STUDY OF NUCLEAR DYNAMICS USING NEUTRONS

By

KAUSHIK BANERJEE
Enrolment No PHYS04200804001

Variable Energy Cyclotron Centre, Kolkata, India

A thesis submitted to the
Board of Studies in Physical Sciences

In partial fulfillment of requirements
For the Degree of

DOCTOR OF PHILOSOPHY

of

HOMI BHABHA NATIONAL INSTITUTE

February, 2013

Homi Bhabha National Institute

Recommendation of the Viva Voce Board

As members of the Viva Voce Board, we certify that we have read the dissertation prepared by **Kaushik Banerjee** entitled "**Study of Nuclear Dynamics using Neutrons**" and recommend that it may be accepted as fulfilling the dissertation requirement for the degree of Doctor of Philosophy.

.....**Date:** 21/5/2013
Chairman - Prof. S R Banerjee

.....**Date:** 21/5/13
Guide / Convener - Prof. Salajananda Bhattacharya

.....**Date:** 21/5/13.
Member 1 - Prof. Satyajit Saha

.....**Date:** 21/5/2013
Member 2 - Prof. Amlan Ray

.....**Date:** 21/05/2013
Member 3 - Prof. Sudipta Narayan Roy

Final approval and acceptance of this dissertation is contingent upon the candidate's submission of the final copies of the dissertation to HBNI.

I hereby certify that I have read this dissertation prepared under my direction and recommend that it may be accepted as fulfilling the dissertation requirement.

date: 21/5/13

Place: VECC, Bidhan nagar

STATEMENT BY AUTHOR

This dissertation has been submitted in partial fulfillment of requirements for an advanced degree at Homi Bhabha National Institute (HBNI) and is deposited in the Library to be made available to borrowers under rules of the HBNI.

Brief quotations from this dissertation are allowable without special permission, provided that accurate acknowledgement of source is made. Requests for permission for extended quotation from or reproduction of this manuscript in whole or in part may be granted by the Competent Authority of HBNI when in his or her judgment the proposed use of the material is in the interests of scholarship. In all other instances, however, permission must be obtained from the author.

KAUSHIK BANERJEE

DECLARATION

I, hereby declare that the investigation presented in the thesis has been carried out by me. The work is original and has not been submitted earlier as a whole or in part for a degree / diploma at this or any other Institution / University.

KAUSHIK BANERJEE

Dedicated to my parents
Tara Pada Banerjee
and
Kalpana Banerjee

ACKNOWLEDGEMENTS

I express my deep sense of gratitude to my supervisor Dr. Sailajananda Bhattacharya for his valuable guidance, supervision and constant encouragement throughout my thesis work. It has been great pleasure and privilege to working with him. His guidance and in-depth teaching helped me to enrich my understanding in the subject to a great extent. His guidance in every stage of this work has made this thesis possible.

I am thankful to Dr. Dinesh Kumar Srivastava (Director, VECC, Kolkata) for his encouragement and kind support. I gratefully acknowledge Dr. Chandana Bhattacharya for her advice, supervision and crucial contribution to this research work. She has been generous in providing valuable guidance and support at different stages of this work. I would also like to convey my sincere thanks to Dr. S. R. Banerjee for many fruitful physics discussions specifically on electronics that helped a lot in successful execution of the experiments. I tender Special thanks to Dr. Tilak Kumar Ghosh for his invaluable support and guidance in the formulation and execution of my first thesis experiment.

With great pleasure, I would like to thank my collaborators Mr. Samir Kundu, Mr. Tapan Kumar Rana, Mr. Pratap Roy, Dr. Gopal Mukherjee, Mr. Jai Kiran Meena, Mr. Ratnesh Pandey, Mr. Supriya Mukhopadhyay, Mr. Deepak Pandit, Dr. Surajit Pal, Manish Gohil, Hari Das Pai and Mrs(Dr.) A. Dey for providing neccessary help and full co-operation towards me. I am grateful to my collaborators Mrs. K. S. Golda, Dr. P. Sugathan of Inter University Accelerator centre and Dr. Pratap Bhattacharya of Saha Institute of Nuclear Physics for their support during the experiment at Pelletron.

I also like to thank Dr. Capas Bandyopadhyay, Dr. Jhilam Sadhukhan, Dr. Santanu Pal for their help. The help received from Mr. Amitava Roy and Mr. Partha Dhara on Data acquisition and other computational aspects is acknowledged with thanks. I take this opportunity to thank the VECC cyclotron staff and NuMC Pelletron staff for the smooth operation of the machine and delivering good quality beam for the experiments.

On personal note, I pay my gratitude to my parents who have supported me all through my academic career and especially to my mother who has been a great source of inspiration since my childhood. I also like to acknowledge my parents-in-law for their kind support and blessings. I would like to thank my wife Shashwati for her continuous love, support and encouragement. This journey would have been much more difficult and in some case impossible without her patience and moral support. Last but not the least I also like to acknowledge my beloved son Kushagra, who's innocent smile have cherised me against all odds.

Kaushik Banerjee

Contents

SYNOPSIS

The aim of the present research is to study the properties of atomic nuclei using neutron as a probe. In low energy nuclear physics, one of the dominant reaction mechanisms is the formation of compound nucleus and its decay. The neutrons (as well as light charged particles and complex fragments) emitted in these reactions carry important information about the compound nuclear decay processes, such as fission and evaporation. Under the present thesis work two physics experiments have been performed. The motivation of the first experiment was to study the dynamics of fission at near-barrier energies by measuring the fission fragment mass distribution and the neutron multiplicity distribution. The second experiment has been performed to study the angular momentum dependence of nuclear level density parameter by measuring the evaporated neutron energy distribution in coincidence with γ-ray multiplicity.

The study of fusion-fission (FF) reaction in transuranic elements at near-barrier energies has immense importance, as it may provide valuable input for the super heavy element synthesis and related studies. One of the competing processes, which is assumed to cause hindrance to the formation of compound nucleus in the transuranic region at near barrier energies, is quasi-fission. In this thesis work, we have investigated the fusion-fission dynamics of ^{16}O + ^{238}U reaction using fission fragment mass distribution and pre-scission neutron multiplicity at near- and below-barrier energies. A sudden change in the fragment mass width, observed in the present measurement, confirmed the transition to quasi-fission at below-barrier energies; the same was indicated earlier by Hinde et.al. from the study of fission fragment angular anisotropy. However, the present measurement of pre-scission neutron multiplicity as well as the earlier measurement of evaporation residue yield by Nishio et.al. did not indicate any significant departure from the respective statistical model predictions throughout the energy range. It is argued that the first two probes are more sensitive for highly asym-

metric systems, whereas all probes would be useful and complimentary to each other for study of quasi-fission in more symmetric systems, where quasi-fission is more dominant.

Nuclear level density (NLD) is an important ingredient of the statistical model, which is generally used for studying a wide variety of nuclear reactions, such as particle evaporation, fission, multifragmentation, and spallation. An accurate determination of NLD, and its dependence on excitation energy and spin in particular, is essential for precise prediction of cross-sections using the statistical models. The dependance of NLD on excitation energy and mass are well established. However its variation with angular momentum is still not well understood. In the present study we have extracted the nuclear level density parameter as a function of angular momentum. In this experiment, we have populated the nucleus ^{119}Sb through ^{4}He + ^{115}In reaction. The light-ion induced reaction has been chosen in the present study over the heavy-ion fusion route, as only one major residue is produced via the $2n$ ($3n$) channel at E^* = 31.3 MeV (42.9 MeV) in the light ion route. The measurement of evaporated neutrons in coincidence with the γ-rays multiplicity and its subsequent statistical model analysis revealed interesting features of the spin dependence of nuclear level density. The inverse level density parameter k appears to be decreasing with increase in angular momentum. Different aspects of nuclear level density, such as the collective enhancement of NLD and the nuclear shape variation at higher angular momentum have been thoroughly considered to expalin the observed trend.

The above experiments were performed with the indigenously developed neutron detectors. As a part of this thesis work, we have developed two types of neutron detectors for neutron energy and multiplicity measurements. Energy measurement is done by time of flight technique using small volume ($\sim$ 1.5 litres) liquid scintillator detector, whereas multiplicity measurement is done using Gd loaded large volume ($\sim$

500 litres) liquid scintillator detector. For neutron energy measurement using time of flight (TOF) technique, several small volume (length $\times$ diameter : $1.5'' \times 5''$, $3'' \times 5''$, $5'' \times 5''$, $7'' \times 5''$) scitillator detectors have been developed. The 4π Gd loaded liquid scintillator detector has been developed primarily for the measurement of neutron multiplicity in the decay of hot nuclei produced in nuclear reactions arround the Fermi energy domain; however, it is also planned to be used for the low energy experiments.

The neutron time of flight detectors were made with liquid scintillator BC501A. A systematic study of the variations of neutron detection characteristics (efficiency, pulse shape discrimination and intrinsic time resolution) has been carried out with these detectors of various dimensions. It has been observed that, with the increase in size of the detector, the pulse shape discrimination property gets poorer and time resolution becomes broader. This is due to the reason that, higher dimension is associated with larger light loss and larger time spread of the arrival of photon at PMT. On the other hand, the detection efficiency increases with the increase in active volume of the detectors. This study helped to optimize the active volume of the detector ($5'' \times 5''$ and $7'' \times 5''$) for the neutron TOF array being developed for experiments with K500 super-conducting cyclotron at VECC, presently undergoing commissioning trials.

Apart from the neutron energy distribution, the total number of neutrons emitted in an event (neutron multiplicity) also plays a crucial role in determining the reaction mechanism, particularly in the Fermi energy domain. However, neutron measurement using time of flight technique is not generally quite efficient to estimate the neutron multiplicity very accurately on event by event basis. This is due to the fact that, the energy measurement using TOF technique is done by modular detectors, which are kept at a certain distance from the source position to achieve reasonable energy resolution. Therefore it suffers due to lack of efficiency. The efficiency may be improved by using large number of detectors; however, very close pack geometry will lead to large cross

talk effect. So the other alternative and rather economical solution is to use a single, large volume detector which will lead to high detection efficiency. By utilising above idea we have developed a 4π neutron multiplicity detector (NMD) using 500 litres of 0.5 % Gd loaded liquid scintillator BC521. Gd has high (n, γ) capture cross-section for thermal neutrons. NMD can measure neutron multiplicity on event-by-event basis with high efficiency (90% at 2 MeV). NMD has been thoroughly tested using ^{252}Cf fission neutron source. The details of the design, fabrication and characterisation are described in the thesis.

List of Figures

List of Tables

Chapter 1

Introduction

1.1 Genesis of nuclear research

Although the radioactivity was discovered by Becquerel in 1896, the actual birth of nuclear physics may be counted with the discovery of nucleus by Lord Rutherford at 1911. He experimentally proved that the major mass of the atom is concentrated in a very small region at the centre of the atom, which he named nucleus. Based on the above finding, the first successful atomic model was proposed by Niels Bohr in 1913, in which he conjectured that the negatively charged electrons are circulating around the positively charged nucleus in certain selected orbits only. Finally, the picture of the nucleus was completed with the discovery of neutron by James Chadwick in 1932. The discovery of neutron gave nuclear physics research a new dimension as was understood that, the neutrons account for the major part of the mass of heavy nucleus, which otherwise would be unstable to sustain against the proton repulsion.

Although a complete century has passed since the discovery of nucleus, still we are unable to explain all nuclear phenomena and the related interactions in simple analytical way like the other interactions. Many shophisticated experiments were performed with the advancement of accelerators, detectors, which helped to explore the finer de-

tails of the nuclei. On the other hand, with the advent of quantum mechanics, many features of nuclear stucture and reactions are now fairly well understood. However, human quest still continues to address the unknown territories of atomic nuclei.

Unlike in the case of atom, where Coulomb force plays the central role, all known fundamental forces except gravity play important roles in the case of nucleus. Since the knowledge of strong interaction, which is the most important interaction in nuclei, is still incomplete, nuclear properties cannot be derived theoretically from first principles. This made the problem of explaining the nuclear structure more difficult compared to the atomic case. Different models were proposed over the years to explain the nuclear structure, among which the shell model and the collective model are known to be highly successful. The shell model explained the ground state spin and magic numbers of the nucleus [May49], whereas collective model emphasized the coherent behavior of all nucleons in a nucleus [Boh53].

Another difficulty in the study of nuclear physics is the limited number of nucleons present inside the nucleus. The nucelon number is neither small enough that, they can be described completely in terms of two body interaction; nor it is large enough like a mole of gas that, where statistical methods can be applied directly to understand the macroscopic properties. This was the main hurdle in the beginning of nuclear physics to describe different nuclear phenomena theoretically. Gradually different theoretical models have been developed, each of which could explain some properties but not the overall nature. One of the most important and fundamental contribution was the "compound nucleus theory" of Bohr, which is one of the mojor backbone of low energy nuclear physics.

At low beam energies (5 - 10 MeV/A), compound nuclear reaction is one of the dominant reaction mechanisms. The present thesis is an attempt to address some of the important aspects of nuclear structure and reaction dynamics at low energy nuclear

reaction using neutron as a probe. The idea of this present work is to study the decay rutes of the compound nucleus and explore some of the important properties of nuclei e.g. nuclear level density. The details of compound nuclear formation and decay have been thoroughly described in the subsequent section with brief description about the open problems in the particular area. Finally a brief description of motivation and outline of the thesis have been presented in the last section.

1.2 Formation of compound nucleus: fusion

In the fusion process, two nuclei fuse together to form a single heavier nucleus. The fused composite soon equilibriates in all degrees of freedom (energy, shape, N/Z ratio) and forms, an intermediate stage known as compound nucleus, before decay into the exit channel. According to the compound nuclear hypothesis, the decay of the compound nucleus is independent of the entrance channel. According to this model, when a projectile x interacts with a target nucleus X, the reaction proceeds in two stages. In the first stage, an excited compound nucleus (C^*) is formed by fusion of the target and the projectile. In the next stage, the excited compound nucleus decays into the final products (Y, y) and the reaction may be symbolically written as,

$$X + x \rightarrow C^* \rightarrow Y + y \tag{1.1}$$

Compound nuclear reaction may be discriminated from other nuclear reaction processes using impact parameter "b" as shown in Fig. 1.1. For distant collisions ($d > R$, d is the distance of closest approach and R is the interaction radius) the ions interact only through the Coulomb field, resulting in Rutherford scattering and/or Coulomb excitation. For peripheral collision ($d \approx R$), the two nuclei interact strongly for a short time resulting in the onset of nucleon exchange and energy damping. As the impact parameter decreses further ($d < R$), there is stong overlap between the colliding nuclei

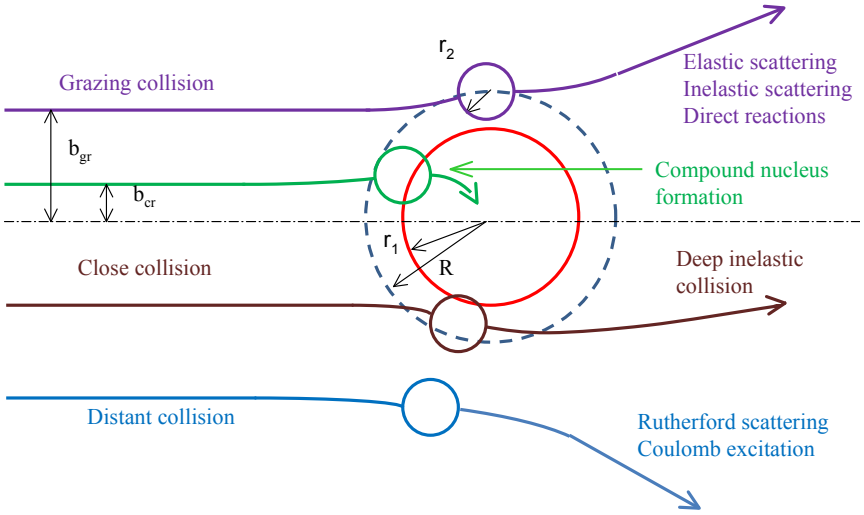

Figure 1.1: *Classification of different nuclear reactions with respect to impact parameter.*

and they interact strongly for a long duration of time. These processes are classified as deep inelastic collision. Finally, if the impact parameter is reduced further ($d << R$), strong dissipative forces lead to the formation of fully energy damped compound nucleus by fusion of the two colliding nuclei. The reaction cross section between b and $b + db$ (or ℓ and $\ell + d\ell$, ℓ is the corresponding partial wave) can be written classically as

$$d\sigma_b = 2\pi b db \qquad or \qquad d\sigma_\ell = 2\pi \lambda\!\!\!^{-2} \ell d\ell, \tag{1.2}$$

Considering that the fusion reaction takes palce upto a certain critical value of impact parameter $b \leq b_{cr}$, the corresponding ℓ values $\ell \leq \ell_{cr}$ the total fusion crosssection can be written as

$$\sigma_{Fus} = \int_0^{\ell_{cr}} d\sigma_\ell = \pi \lambda\!\!\!^{-2} \ell_{cr}^2 \tag{1.3}$$

Fusion crosssection can be generalised in quantum mechanical picture as

$$\sigma_{Fus} = \sum_{\ell=0}^{\ell_{cr}} \sigma_\ell = \pi \lambda\!\!\!^{-2} \sum_{\ell=o}^{l_{cr}} (2\ell + 1) T_\ell = \pi \lambda\!\!\!^{-2} (\ell_{cr} + 1)^2 \approx \pi \lambda\!\!\!^{-2} \ell_{cr}^2 \tag{1.4}$$

$$T_\ell = \begin{cases} 1 & \ell < \ell_{cr} \\ 0 & \ell > \ell_{cr} \end{cases}$$

Here $\lambda\!\!\!^{-}$ is the reduced wavelength, and T_ℓ is the transmission coefficient through the barrier. Since ℓ_{cr} is the highest partial wave for which it can cross the barrier, i.e., $E_{cm} = V(R_B) + \hbar^2\ell_{cr}^2/2\mu R_B$, where $V(R_B)$ is barrier height at R_B, replacing this in the earlier equation, one obtains

$$\begin{aligned} \sigma_{Fus} &= \pi R_B^2\left(1 - \frac{V_B}{E_{cm}}\right) && \mathrm{E}_{cm} > V_B \\ &= 0 && \text{otherwise} \end{aligned} \tag{1.5}$$

Here E_{cm} is the beam energy in centre of mass frame, μ is the reduced mass of the target projectile system, R_B is the separation between target and projectile centres. The above relation describes the dependence of fusion cross section on beam energy. The total reaction cross section of which fusion cross section is a part, can be categorised in terms of incident beam energy and angular momentum brought in by the projectile. Fig. 1.2 shows the fusion cross-section in terms of incident beam energy. From the systematic study of fusion cross-section σ_{Fus}, it has been found that the variation of σ_{Fus} with bombarding energy has three distinct regions [Hod78, Bas80]. In the lower energy region slightly above the barrier (region 1), fusion cross-section increases with incident energy alongwith the total reaction cross-section σ_{tot} and in this region $\sigma_{Fus} \approx \sigma_{tot}$. Eq. 1.5 explains the energy dependence of σ_{Fus} in this region. At higher energies, (region 2) the slope of σ_{Fus} changes and in this region $\sigma_{Fus} < \sigma_{tot}$ due to opening of many other reaction channels. At further higher energies, there may be another region (region 3) where fusion cross-section falls off sharply, which may be due to the fission limit of compound nucleus.

The angular momentum dependence of the reaction cross section is shown schematically in Fig. 1.3. The lower part of the angular momentum distribution (up to ℓ_{cr}) leads to the fusion. This can be further divided into two parts according to the

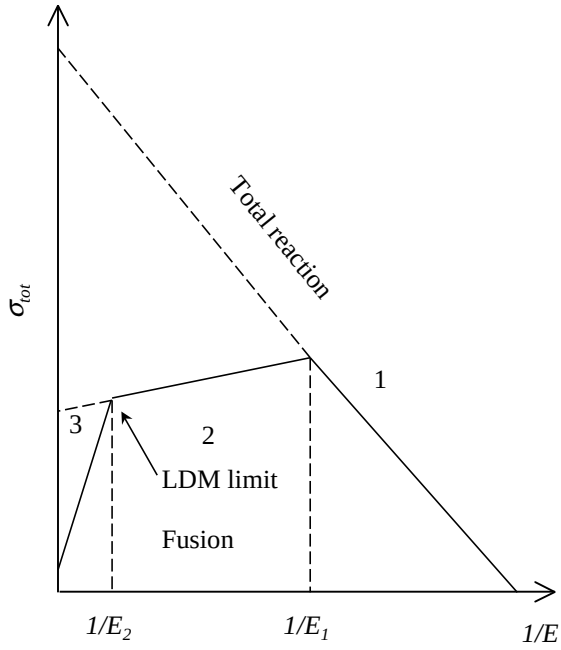

Figure 1.2: *Variation of fusion cross-section with incident beam energy.*

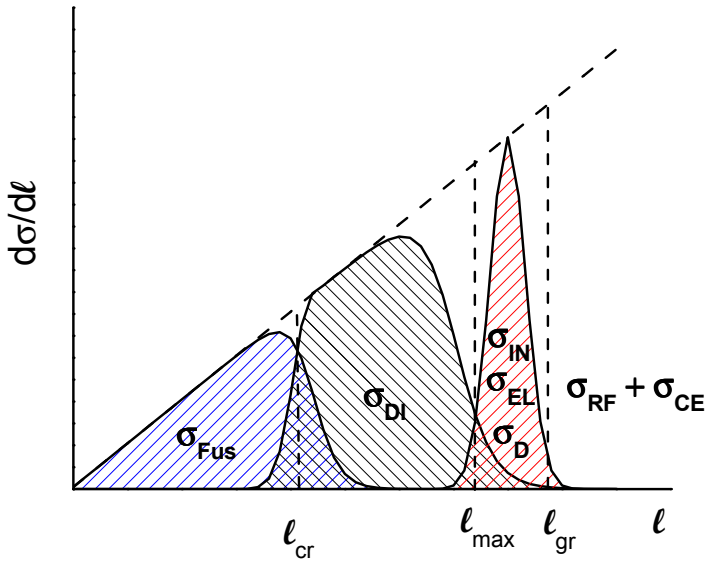

Figure 1.3: *Classification of different nuclear reaction by angular momentum.*

decay. Fusion evaporation (FE) dominates at lower values of ℓ and fusion fission (FF) process dominate at $\ell \approx \ell_{cr}$. In higher angular momentum region ($\ell_{cr} \leqslant \ell \leqslant \ell_{max}$)

deep inelastic (σ_{DI}) processes dominates. In the next higher angular momentum region ($\ell_{max} \leqslant \ell \leqslant \ell_{gr}$, ℓ_{gr} being the grazing angular momentum) elasic scattering (σ_{EL}), inelasic scattering (σ_{IN}) and direct reactions (σ_D) occur. Beyond ℓ_{gr} ($\ell > \ell_{gr}$) Ruthford scattering (σ_{RF}) and Coulomb excitation (σ_{CE}) occur.

1.3 Decay of compound nucleus: evaporation

Light and intermediate mass compound nuclei (typically $A_{CN} < 150$) predominantly de-excite by emitting light particles and gamma rays, and this process is termed as evaporation. The evaporation of light particle of any particular type stops when excitation energy drops to a value below the corresponding particle separation energy. The de-exciation of the system thus stops with the formation of evaporation residue which can then undergo only γ-decay to come back to ground state. In evaporation process, particle emission leads to the decrease of excitation energy but it does not substantially change the average angular momentum. In the later stages of de-excitation, particle emission from the high angular momentum states is hindered to a degree where γ-emission competes favorably with particle emission. The γ decay extends in typical cases to approximately one neutron binding energy above the yrast line. The yrast energy for angular momentum J is defined as the energy for which no levels of angular momentum value J exist below that energy and is qualitatively given by $E_{rot} = (\hbar^2/2\Im_{eff})J(J+1)$, $\Im_{eff}$ being the effective moment of inertia. Once the region of the yrast line is reached, γ rays cascade from one yrast level to the next, each reducing the J value of the nucleus. Pictorial representation of Yrast line is shown in Fig. 1.4.

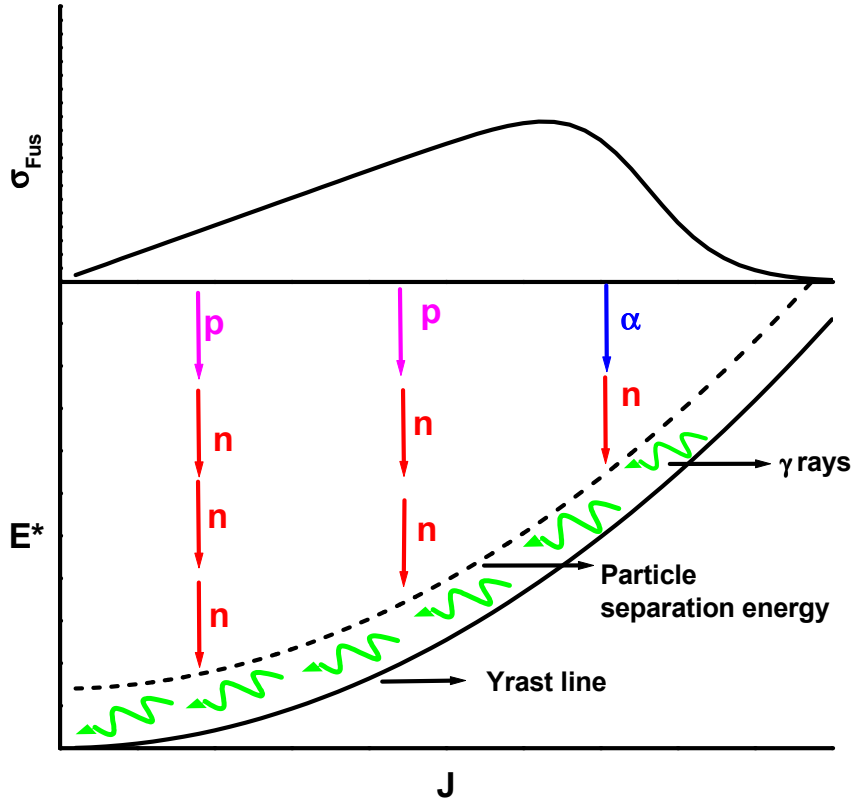

Figure 1.4: *Schematic diagram showing the formation cross-section of compound nucleus at a fixed excitation energy with broad range of angular momentum (top) and decay of compound nucleus via particle and γ emission (bottom).*

1.3.1 Estimation of evaporation probablity using statistical model approach

Nucleus, being a complex many body system, may exist in many different configurations even at very small excitation energy. The density of the quantum mechanical states increases rapidly with excitation energy. Even at near barrier energies, there are many states available for a compound nucleus and it may decay through different routes. Due to the complexity to estimate number of states microscopically, the statistical models are essential for the understanding and prediction of evaporation phenomena. In the case of compound nuclear decay through particle emission, the probability of particle decay is inversely proportional to the total number of possible decays. So, in

the calculation based on statistical framework, it is generally assumed that all possibilities for decay are intrinsically equally likely and are thus governed by density of final states and barrier penetration factor (transmission coefficient). The theoretical description of the compound nuclear decay was first proposed by Weisskopf [Wei37, Wei40] under the framework of statistical mechanics. Weisskopf did not consider the angular momentum dependence, which was resolved by Hauser and Feshbach [Hau52] by considering angular momentum in their calculation. The model is based on the Bohr's independent hypothesis and the principle of detailed balance. Formation and decay channels are statistically independent. The principle of detailed balance assumes that the transition probability $W_{i\to f}$ of a system from an initial state (i) to final state (f) is related to the probability of inverse transition $W_{f\to i}$ as follows

$$\rho_i W_{i\to f} = \rho_f W_{f\to i} \tag{1.6}$$

Here ρ_i and ρ_f are the densities of the initial and the final states respectively. The partial cross-section for compound nucleus formation can be written as [Bla52, Tho64]

$$\sigma_{Fus} = \pi\lambda\!\!\!^{-2}\frac{2J_{CN}+1}{(2J_P+1)(2J_T+1)}\sum_{J_P-J_T}^{J_P+J_T}\sum_{J-S}^{J+S}T_\ell \tag{1.7}$$

Here J_{CN} is the compound nucleus spin, J_P, J_T are the spins of projectile and target nuclei. T_ℓ is the transmission coefficients for entrance channel, which depends upon the projectile energy. Here $S = J_P + J_T$ is the channel spin.

$$T_\ell = \frac{1}{1+exp[-(\ell-\ell_{cr})/d]} \tag{1.8}$$

Here d is the diffuseness parameter, ℓ_{cr} is the critical angular momentum for fusion. The evaporation cross section is generally estimated by Hauser Feshbach method [Hau52]. In this method, the cross section σ_i for the decay of the compound

nucleus to channel i can be expressed in terms of partial and total decay widths as follows

$$\sigma_i = \sigma_{Fus} \frac{\Gamma_i}{\sum_i \Gamma_i} \tag{1.9}$$

The partial decay width of a compound nucleus of excitation energy E^* and spin J_{CN} for the evaporation of particle i is [Hau52]

$$\Gamma_i = \frac{1}{2\pi\rho_{CN}(E^*, J_{CN})} \int \sum_{J_d=0}^{\infty} \sum_{J=|J_{CN}-J_d|}^{J_{CN}+J_d} \sum_{\ell=|j-s|}^{j+s} \rho_d(E^* - B_i - \epsilon, J_d)\mathscr{T}_\ell(\epsilon)d\epsilon \tag{1.10}$$

where J_d is the spin of the daughter nucleus, s, ℓ and j are the spin, orbital and total angular momenta of the evaporated particle, ϵ and B_i are its kinetic and separation energies, $\mathscr{T}_\ell(\epsilon)$ is the transmission coefficient for the exit channel i. ρ_d and ρ_{CN} are the level densities of the daughter and the compound nuclei respectively.

1.3.2 Nuclear Level Density

It is clear from the above (Eq. 1.10) that nuclear level density plays a crucial role in determining the statistical decay rate. The nuclear level density (NLD) is the number of different ways in which individual nucleons can be placed in the various single particle orbitals such that the excitation energy lies in the range E^* and $E^* + dE^*$. NLD provides important structural information of highly excited nuclei, and is necessary in understanding complex nuclear reaction. Thus one needs a sufficiently accurate description of the nuclear level density over a wide interval of the excitation energy and angular momentum. Since we know the nuclear level densities accurately only at low excitation energies, we largely depend on different theoretical models to predict the level densities at high excitation energies. Among the different models, Fermi gas model [Bet36], constant temperature model [Gil65], Gilbert Cameron model [Gil65a], Hartree Fock BCS model [Her05, Dem01], Moment method [Hua00, Lang93, Nak97]

are generally used. The Fermi gas model is the most widely used description of the nuclear level density which was proposed by Bethe [Bet36]. It is based on the thermodynamic relation between entropy and average energy of a nucleus, which is assumed to be made up of nucleons behaving like non-interacting Fermi gas. Bethe's model assumes that, the individual neutrons and protons occupy a set of low energy levels in the ground state and fill up the higher individual states at any excitation energy. The nuclear level density for a spherical nucleus in the Fermi gas model with constant single-particle level density (uniform level spacing) can be estimated as,

$$\rho_{int}(E^*, J) = \frac{(2J+1)}{12}\left(\frac{\hbar^2}{2\Im_{eff}}\right)^{3/2} \sqrt{a} \times \frac{\exp[2\sqrt{a(E^* - E_{rot} - \Delta_P)}]}{(E^* - E_{rot} - \Delta_P)^2} \tag{1.11}$$

$$E_{rot} = \frac{\hbar^2}{2\Im_{eff}} J(J+1) = \frac{\hbar^2}{2\Im_{rig}(1 + \delta_1 J^2 + \delta_2 J^4)} J(J+1). \tag{1.12}$$

$$\Im_{rig} = \frac{2}{5} A^{5/3} r_\circ^2 \tag{1.13}$$

$$a = \frac{\pi^2}{6}[g^n(\epsilon_F^n) + g^p(\epsilon_F^p)] \tag{1.14}$$

$$g^n(\epsilon_F^n) = \frac{3A}{2\epsilon_F^n} \qquad g^p(\epsilon_F^p) = \frac{3A}{2\epsilon_F^p} \tag{1.15}$$

Here E^*, E_{rot}, Δ_P, $\Im_{eff}$, $\Im_{rig}$, J, A are the excitation energy, rotational energy, pairing energy, effective moment of inertia, rigid body moment of inertia, angular momentum and mass number of the decaying nucleus, respectively. The parameters a, $r_\circ$, δ_1, δ_2 are the nuclear level density parameter, nuclear radius and deformability coefficients, respectively. $g^n(\epsilon_F^n)$ and $g^p(\epsilon_F^p)$ are the neutron and proton single-particle level densities at their respective Fermi energies, ϵ_F^n and ϵ_F^p, respectively. The density of levels near the ground state varies markedly depending on an odd or even numbers of

neutrons and protons, the vicinity of the closed shell and the spherical or the deformed nature of the nucleus. Our current understanding of the structure of low lying nuclear levels is based on few important concepts. Some of the most important concepts are shell effect, pairing correlation and collective phenomena, which are discussed below.

- **Shell effect on NLD**

  The NLD parameter, *a*, is related to the density of the single particle levels near the Fermi surface and is influenced by the shell structure and the shape of the nucleus, which in turn depend on excitation energy. The shell effect in nuclear level density parameter is shown in Fig. 1.5, which indicates decrease in level density parameter in the visinity of magic nuclei. The spacing and the order

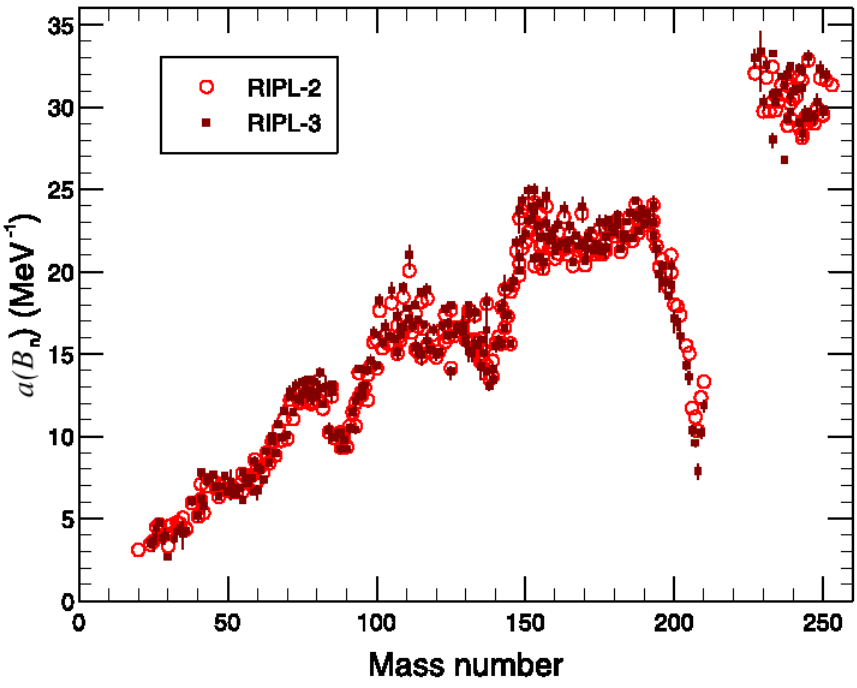

Figure 1.5: *Variation of nuclear level density parameter with mass number, data taken from the compilation of Reference Input Parameter Library (RIPL) [Cap09].*

of the single particle level depends on the shape of the nuclear potential. The

deformation is related to shell effect, which may be seen by comparing the sequence of single particle levels for a spherical nucleus with those for a nucleus with varying deformation. Excitation energy dependent description of nuclear level density parameter, a, has been proposed by Ignatyuk et. al. [Ign75], which incorporated the effect of nuclear shell structure at low excitation energy and went smoothly to the liquid drop value as expected at higher excitation energy. This is expressed as,

$$a = \tilde{a}[1 - \frac{\Delta S}{U}\{1 - \exp(-\delta U)\}] \tag{1.16}$$

$$U = E^* - E_{rot} - \Delta_P \tag{1.17}$$

$$\delta^{-1} = \frac{0.4A^{4/3}}{\tilde{a}}, \tag{1.18}$$

$$\Delta_P = \frac{12}{\sqrt{A}} \tag{1.19}$$

where, $\tilde{a}$ is the asymptotic Fermi gas value of the liquid drop NLD parameter at the excitation energy where shell effects are believed to be depleted leaving a smooth dependence on mass number A, ΔS is the shell correction obtained from the difference of the experimental and the liquid drop model masses and δ is the rate at which the shell effect is depleted with the increase in excitation energy. E^*, E_{rot} and Δ_P are the excitation energy, rotational energy and pairing energy of the decaying nucleus. Pairing energy is positive for (even, even) nuclei, zero for (odd, even) and (even, odd) and negative for (odd, odd) nuclei.

- **Collective enhancement of NLD**

  One of the interesting aspects of NLD at low excitation energy is the possibility of its collective enhancement due to the coupling of rotational as well as vibrational degrees of freedom with the single particle degrees of freedom for nuclei with appreciable ground state deformations. The microscopic calculation of

level densities for deformed and spherical nuclei and their comparison with the respective experimental level densities obtained from neutron resonance studies indicated the need for including the effect of collective excitation on single particle level density. The collective enhancement of NLD due to the ground state deformation was qualitatively described by Ignatyuk et. al. [Ign79]. According to this prescription, the level density $\rho(E^*, J)$ at excitation energy E^* and angular momentum J may be expressed as,

$$\rho(E^*, J) = \rho_{int}(E^*, J)K_{coll}(E^*) \tag{1.20}$$

where $K_{coll}(E^*) = K_{vib}(E^*)K_{rot}(E^*)$ is the collective enhancement factor, consisting of both vibrational and rotational contributions. $\rho_{int}(E^*, J)$ is the intrinsic level density comprising of single particle level density. In deformed nuclei, the most important contribution to the collective enhancement of NLD originates from the rotational excitations, whereas in case of spherical nuclei, the collective enhancement can be caused by vibrational excitations [Cha10]. The long range correlations, which are mainly responsible for the enhancement of level density, are expected to die out at higher excitation. Björnholm, Bohr and Mottleson [Boj73] have suggested that there may be a critical temperature, T_c, beyond which the collective enhancement in NLD is expected to fade out, and the value of T_c is estimated as,

$$T_c = \hbar\omega_0\beta_2 \sim 40A^{-1/3}\beta_2 \text{ MeV}. \tag{1.21}$$

where ω_0 is the mean oscillation frequency and β_2 is the ground state nuclear quadrupole deformation. As a consequence, there should be a reduction of the NLD parameter above T_c. However, the results of some of the recent experiments, although showing indications about such changes in some cases, are not quite conclusive [Jun98, Kom07].

- **Excitation energy dependence of NLD**

  From Eq. 1.11 it is evident that nuclear level density increases rapidly with the increase in excitation energy. Most often, several evaporation channels are in competition. The characteristic functional form of the level density ($exp(2\sqrt{aE^*})$) has an important consequence for the excitation energy dependence of this competition. Fig. 1.6 shows the logarithms of the level densities as a function of excitation energy, which indicates that the logarithms of the level densities approach each other with increasing energy. This means that the decay probabilities of the different channels come closer to each other. They asymptotically tend to become equal. This means that decay channels, which are negligible at low excitation energies become more important or even comparable with the most important channels at higher excitation energy. This also implies that the number of open channels increases with excitation energy.

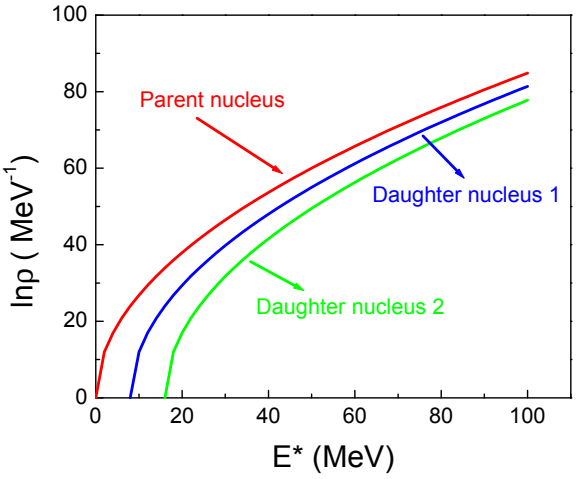

Figure 1.6: *Schematic of excitation energy dependence of NLD of mother and two daughter nuclei, shifted by corresponding emission thresholds.*

Recent experiment showed, the excitation energy dependence of nuclear level density as described in Eq. 1.11 is however not sufficient [Neb86]. Precise mea-

surement over a wide range of excitaiton energy showed that, further dependence is needed, which is incorporated through excitaiton energy dependence of nuclear level density parameter a. The observed trend was subsequently analysed and reproduced by the theoretical calculation performed by Shlomo and Natowitz [Shl90]. They considered the effects of the finite nuclear size, the momentum and frequency dependence of the effective mass, shell effects and the corresponding variation of these effects with temperature. Fig. 1.7 [Shl90] shows the calculated values of nuclear level density parameter k along with the measured one as a function of temperature (where k is the inverse level density parameter; $k = 1/a$).

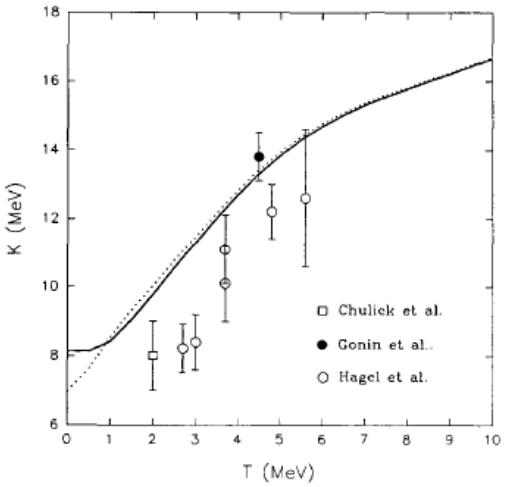

Figure 1.7: *Variation of nuclear level density parameter k with temperature T.*

- **Spin dependence of NLD**

  In the phenomenological description of the J -dependence, there are two prescriptions. In the first approach the J -dependence appears as a multiplicative

function to the total level density. This function is a Gaussian whose width is defined in terms of a temperature dependent spin cut-off parameter σ.

$$\rho(E^*, J) = \frac{\sqrt{a}}{24}\left(\frac{\hbar^2}{2\Im_{rig}}\right)^{3/2}\frac{exp(2\sqrt{aE^*})}{E^{*2}}\left[\frac{2J+1}{2\sigma^2}exp(\frac{-(J+1/2)^2}{2\sigma^2})\right] \quad (1.22)$$

$$\sigma^2 = \frac{T\Im_{rig}}{\hbar^2} \quad (1.23)$$

However this formalism is mostly used in low excitation energy and low angular momentum region, such as neutron capture resonances. The other approach is used at higher excitation energy and angular momentum region, where the spin dependence in NLD is generally taken into account in an approximate way by incorporating the spin dependent shape change as predicted by rotating liquid drop model (RLDM)[Coh74]. In this approach, the rotational energy $E_{rot} = (\hbar^2/2\Im_{rig})J(J+1)$ is subtracted from the excitation energy E^*. This effective excitation energy is used in the conventional formula for the level density $\rho(E^*, J)$ (see Eq. 1.11). The level density parameter is taken as constant and the J dependence of $\rho(E^*, J)$ is incorporated through E_{rot} by modifying the moment of inertia term $\Im_{eff} = \Im_{rig}(1 + \delta_1 J^2 + \delta_2 J^4)$. This prescription has been used to explain inclusive particle spectra at higher excitation energies and at higher angular momenum. Exclusive measurement with respect to the angular momentum may reveal additional details on the spin dependence of NLD. For $E^* >> E_{rot}$, the two prescriptions become equivalent.

1.3.3 Transmission coefficient

The transmission coefficient $\mathscr{T}_\ell$ as discussed in Eq. 1.10, is generally estimated from the analysis of the angular distribution of elastic scattering between the emitted particle and the residue nuclei using optical model. In the optical model the interaction

between an incident particle and a target nucleus is represented by a complex mean field potential V_{opt}(r), which has both real and imaginary components. The real part always represents the strength of the potential, which causes the elastic scattering, and the imaginary part gives the strength of the absorptive potential through all non-elastic channels, which accounts for the loss of incident flux. The absorption may be of different kinds such as surface type, volume type or a combination depending upon the energy and structure of the interacting particles. Typical form of optical model potential is given below

$$
\begin{aligned}
V_{opt}(r) = \quad & +V_C(r) && \text{Coulomb term} \\
& -V_v f_v(r) && \text{real volume term} \\
& +V_s g_v(r) && \text{real surface term} \\
& -iW_s g_w(r) && \text{imaginary surface term} \\
& -iW_v f_w(r) && \text{imaginary volume term} \\
& -d_{so}\vec{\ell}\cdot\vec{s}\,V_{so}h_{V_{so}}(r) && \text{real spin-orbit term} \\
& +id_{so}\vec{\ell}\cdot\vec{s}\,W_{so}h_{W_{so}}(r) && \text{imaginary spin orbit term}
\end{aligned}
$$

where $d_{so} \approx 2\,fm$ is the spin-orbit constant. The Coulomb term is generally calculated by assuming interaction of a point charge with a uniformly charged sphere of radius R_c

$$
V_C(r) = \begin{cases} \left(\dfrac{3}{2} - \dfrac{r^2}{2R_c^2}\right) Z_p Z_t e^2/R_c & r \leqslant R_c \\ \\ Z_p Z_t e^2/r & r > R_c \end{cases}
$$

Z_p and Z_t are projectile and target charge respectively. The real and imaginary volume terms are normally taken to be of Wood-Saxon form

$$
f_i(r) = \frac{1}{\left[1 + exp\left(\dfrac{r - R_i}{a_i}\right)\right]} \qquad i = V, W, \tag{1.24}
$$

where R_i, a_i are the radius and diffuseness respectively. The real volume potential reflects the average interaction of the projectile with the nucleons of the target nucleus.

The imaginary volume potential takes into account the loss of projectile nucleon due to the collision with the nucleons of the target. The real and imaginary surface terms of the optical potential are taken to be either the derivative of Wood-Saxon

$$g_i(r) = -4a_i \frac{d}{dr} f_i(r) = 4\frac{exp[(r - R_i)/a_i]}{(1 + exp[(r - R_i)/a_i])^2} \qquad i = V, W, \tag{1.25}$$

or a Gaussian

$$g_i(r) = exp\left[\frac{(r - R_i)^2}{a_i^2}\right] \qquad i = V, W, \tag{1.26}$$

The real surface term of the optical potential is used to invoked nuclear many body effects. The imaginary surface term takes into account the absorption due to the coupling to the quasi bound compound nucleus states and to the excitation of low energy collective modes which have their coupling concentrated in the nuclear surface. The spin-orbit term is included to take into account the interaction between the spin of the nucleon with its orbital momentum. Both the real and imaginary spin-orbit terms of the optical potential are taken to have a Thomas form factor,

$$h_i(r) = -\frac{1}{r}\frac{d}{dr} f_i(r) = \frac{1}{ra_i}\frac{exp[(r - R_i)/a_i]}{[1 + exp\{(r - R_i)/a_i\}]^2} \qquad i = V_{so}, W_{so}, \tag{1.27}$$

The radius R_i is parametrised in terms of the reduced radius r_i and target mass as $R_i = r_i A^{1/3}$, with r_i in the range $r_i \approx 1.1$ -1.3 fm. The diffuseness values are generally taken in the range $a_i \approx 0.4$ -0.7 fm. The different optical model parameters V_v, V_s, W_s, W_v, V_{so}, W_{so}, a_s are are estimated by fitting the calculated angular distribution with experimental data.

The wave functions associated with the scattered particles are calculated from the optical potential by solving the Schrödinger equation.

$$\nabla^2\psi + \frac{2m}{\hbar^2}[E - V_{opt}(r)]\psi = 0 \tag{1.28}$$

Considering the total wave function ψ as a combination of an incident plane wave and a spherical scattered wave. This may be done by expanding ψ in partial waves. These equations may be integrated numerically for each values of ℓ contributing to the interaction and the resulting (complex) radial wave functions are matched to the known asymptotic form beyond the nuclear field to obtain the scattering matrix element S_ℓ. The observable quantity can be described as

$$\frac{d\sigma(\theta)}{d\Omega} = |f(\theta)|^2 \tag{1.29}$$

where

$$f(\theta) = f_C(\theta) + \frac{1}{2ik}\sum_{\ell=0}^{\infty}(2\ell+1)(S_\ell - 1) \tag{1.30}$$

in which $f_C(\theta)$ is the Coulomb scattering amplitude. The expression for elastic scattering (σ_{EL}), reaction cross-section (σ_R) and total reaction cross-section (σ_{tot}) can be written as follows

$$\sigma_{El} = \pi\lambda\!\!\!^{-2}\sum_{0}^{\infty}(2\ell+1)|1 - S_\ell|^2 \tag{1.31}$$

$$\sigma_R = \pi\lambda\!\!\!^{-2}\sum_{0}^{\infty}(2\ell+1)(1 - |S_\ell|^2) \tag{1.32}$$

$$\sigma_{tot} = \sigma_{El} + \sigma_R \tag{1.33}$$

$$\mathscr{T}_\ell = 1 - |S_\ell^2| \tag{1.34}$$

$$S_\ell = exp(2i\delta_\ell) \tag{1.35}$$

Here $\lambda\!\!\!^{-}$ is the reduced de-Broglie wavelength, δ_ℓ is a complex number representing the phase shift between the outgoing and the ingoing waves, and, $\mathscr{T}_\ell$ is the tranmission coefficient.

1.3.4 Experimental determination of NLD parameter

The most straightforward method of determining level density is to count individual levels. This is possible at low excitation energies where the levels are well spaced and easily resolved by a variety of techniques including charged particle and neutron spectroscopy. Level densities of nuclei at excitation energies well above the particle separation energy, where they form the continuum, can however be studied only through less direct approaches which involve models for the formation and decay of the compound nucleus.

Though several attempts have been made in the recent years to understand, both theoretically as well as experimentally, the excitation energy (temperature) dependence of NLD [Kat78, Shl91, Shl90, Cha05], the information available about its angular momentum dependence is quite limited. Henss et. al. had extracted the NLD at high spin by measuring the neutron spectra for $1n$ evaporation channel in coincidence with the Yrast γ-rays measured with a 4π gamma detector array [Hen88], but they did not explore the dependence of NLD in different angular momentum region. In another measurement, Mitra et. al. showed a broad structure in γ-ray multiplicity gated charged particle particle spectrum in ^{12}C + ^{93}Nb system and they conjectured that it may be due to an unusual spin and excitation energy dependence of the nuclear level density [Mit02, Mit06]. In a recent experiment by Gutpa et. al., the γ-ray multiplicity gated α-particle evaporation spectra were measured for a number of nuclei with $A \sim 180$, $E^* \sim 56$ - 61, $< J > \sim 15$ -30 $\hbar$, the inverse level density parameters 'k' (= $1/a$) were found to remain constant within the limits of statistical errors [Gup09]. In an another measurement by the same group, performed at $A \sim 120$, $E^* \sim$60 MeV, $< J > \sim 10$ -20 $\hbar$ and Z_R =48-55 (Z_R is the atomic number of the residue), no systematic variation of the inverse level density parameter was observed. For Z_R = 49, 50, and 51, 'k' was found to be constant while for the other cases it was observed to increase with

increasing angular momentum [Gup08]. However, the calculations based on statistical theory of hot rotating nuclei [Agg10] predicted that the value of k would increase with J in all cases. As the experimental information on level density parameter as a function of angular momentum is still scarce, it is evident that the interplay of the key parameters, such as ground state deformation, excitation energy and spin in NLD is yet to be properly understood. So the present understanding on the variation of NLD as a function of angular momentum is not conclusive and require further investigations.

1.4 Decay of Compound Nucleus: Fission

An excited compound nucleus with mass $\gtrsim 200$ predominantly decays by fission, where it breaks up into two nuclei having similar masses. In recent years, one of the major goals of the fission research is to understand the dynamics of fission in the super heavy region. There has been a lot of activities in the study of the mechanism of fusion reaction at near-barrier energies in the actinides region [Hin95, Gho09, Ram85, Itk04, Nis08], which plays key role in the synthesis of super heavy elements (SHE). Major hindrance in the formation of super heavy elements is the suppression of fusion - evaporation (FE) channel not only by the equilibrium fission process but also due to the non equilibrium fission processes, such as, quasi-fission (QF) and preequilibrium fission (PEF). There are plenty of research activities around the globe in recent years to identify, and, if possible, quantify the factors which hinder the compound nucleus formation and and to locate the favorable condition for fusion to occur (incident beam energy, entrance channel parameters).

1.4.1 Equilibrium and non equilibrium fission process

Equilibrium fission (or fusion-fission) is characterised by the formation of a compound nucleus (CN) which is equilibrated in all degrees of freedom. In this case fission fragment mass, energy and angular distributions are expected to exhibit properties which are independent of the entrance channel. On the other hand, in the case of non-equilibrium fission, the composite system undergoes fission before attaining complete equilibration in all degrees of freedom (energy, mass, shape etc). The non-equilibrium fission process can be broadly categorized in three types, quasi-fission, fast-fission and pre-equilibrium fission. The occurrence of these processes can be understood, in terms of the potential energy landscape of interaction potential as a function of the inter-nuclear distance r as illustrated in Fig. 1.8.

Consider the two colliding nuclei in ground states when they are far apart. At the point of collision, a neck is formed between the two nuclei, which gradually evolves to a single composite system with two mass and charge distribution centers. The interaction potential, estimated by assuming it to be a function of separation between the two nuclei alone, where all the internal degrees of freedom are frozen, is termed as “sudden potential”. The sudden approximation is reasonably valid to describe the fusion potential of the colliding ions. In the subsequent evolution of the fused system, the composite system relaxes in shape and mass degrees of freedom and thus generates a new density distribution in the region where the ion overlap is the strongest. So exit channel (fission) potential is calculated using adiabatic approximation, where the nuclear shape is allowed to adjust so as to minimize the potential energy at each distance of separation. Due to the continual change in shape, the adiabatic procedure does not lead to any short-range repulsion. Adiabatic and sudden approximations are very useful for obtaining analytical results which provide a conceptual framework for understanding the fusion-fission process.

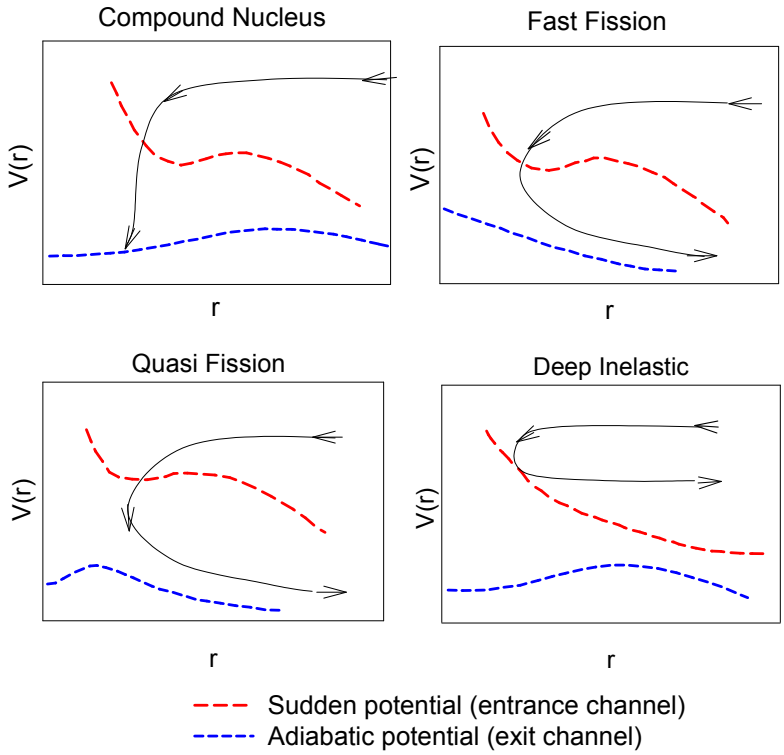

Figure 1.8: *Illustration of different reaction mechanisms in terms of entrance channel (red long dash line) and exit channel nuclear potential (blue short dash line) as a function of internuclear distance.*

In the case of equilibrium fission (or fusion-fission), the composite is trapped in the entrance channel after surmounting the fusion barrier. The saddle configuration is elongated enough to keep the system trapped and the system evolves to the formation of compound nucleus. After that, fission occurs from the compound nucleus crossing the fission barrier (see Fig. 1.8). On the contrary, in the case of quasi fission, the composite is trapped behind the conditional saddle point for the mass asymmetric entrance channel (sudden potential). Subsequently, the composite system evolves towards symmetry and the potential between them also evolves (the adiabatic potential), in such a way that the composite reaches mass asymmetric saddle directly, which means that the system first fuses and then fission occurs without passing through the compound nuclear configuration. This reaction channel is characterized by full energy relaxation

but incomplete mass and shape relaxations. The pictorial representation of the quasi fission trajectory in three dimensional potential energy surface is shown in Fig. 1.9.

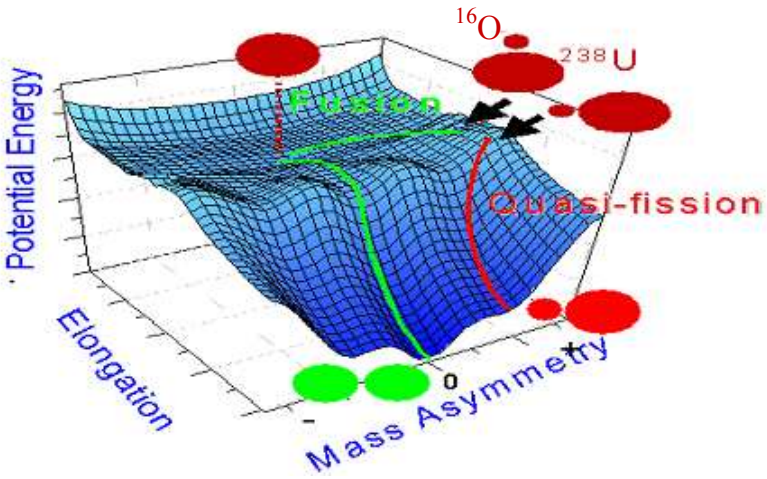

Figure 1.9: *Pictorial representation of quasi fission in three dimensional potential energy surface.*

Quasi-fission phenomenon is generally observed in Actinide nuclei. Hinde et. al. investigated the orientation effects in fusion-fission reaction in ^{238}U nucleus [Hin95]. The ^{238}U nucleus is prolate deformed in the ground state; therefore the Coulomb-barrier height between target and projectile nuclei depends on their mutual orientation, and, different reactions may occur from different touching configurations. The two extreme cases are the collisions with polar and equatorial sides of the deformed target nucleus. At low projectile energy, nuclear contact occurs only at polar collisions, whereas at higher energy contact is obtained also in equatorial collisions. It was observed that the equatorial collisions result in fusion-fssion, whereas the polar collisions lead to quasi-fusion at near barrier energies [Hin95].

Fast fission, a non-equilibrium fission process, occurs when the composite is trapped inside the fusion pocket but the fission barrier of the compound nucleus

vanishes due to large angular momentum (see Fig. 1.8). For fast fission to occur $J_{cr} > J_{bf=0}$. The typical reaction time scale of fast fission is of the order of 10^{-21} to 10^{-20} seconds, which is intermediate of deep inelastic reaction and fusion-fission time scales [Bac81]. The deep inelastic phenomenon occurs when the pocket in the sudden (entrance channel) potential vanishes due to large angular momentum (see Fig. 1.8). In this case the system may not get sufficient time for significant mass exchange before the separation.

Another non-equilibrium fission process, pre-equilibrium fission, takes place when fission occurs before the composite system equilibrate in K degree of freedom; K is projection of total angular momentum J on the fission axis (see Fig 1.10). Ramamurty et. al [Ram85] proposed the pre-equilibrium fission model and explained the anomalous angular distributions of several fissioning systems e.g., ^{19}F, ^{24}Mg, ^{28}Si and ^{32}S + ^{208}Pb. Pre-equilibrium fission gives rise to a narrow variance around $K = 0$ for spin less particles, as the memory of the entrance channel reaction plane is partially retained in these reactions. This usually occurs in systems where the fission barrier height is comparable to the temperature and the fission width is sufficiently large.

1.4.2 Estimation of fission probablity using statistical model approach

Similar to evaporation as described by Eq. 1.10, the fission decay width is estimated using Bohr and Wheeler [Boh39] model,

$$\Gamma_f^{BW} = \frac{1}{2\pi\rho_{gs}(E^*)} \int_0^{E^*-B_f} \rho_{sp}(E^* - B_f - \epsilon)d\epsilon \tag{1.36}$$

Here ρ_{gs} and ρ_{sp} are the level density at the ground state (stable equilibrium position) and the fission saddle point (unstable equilibrium position) respectively, E^* is the total excitation energy, B_f is the fission barrier height. Considering the effect of nuclear vis-

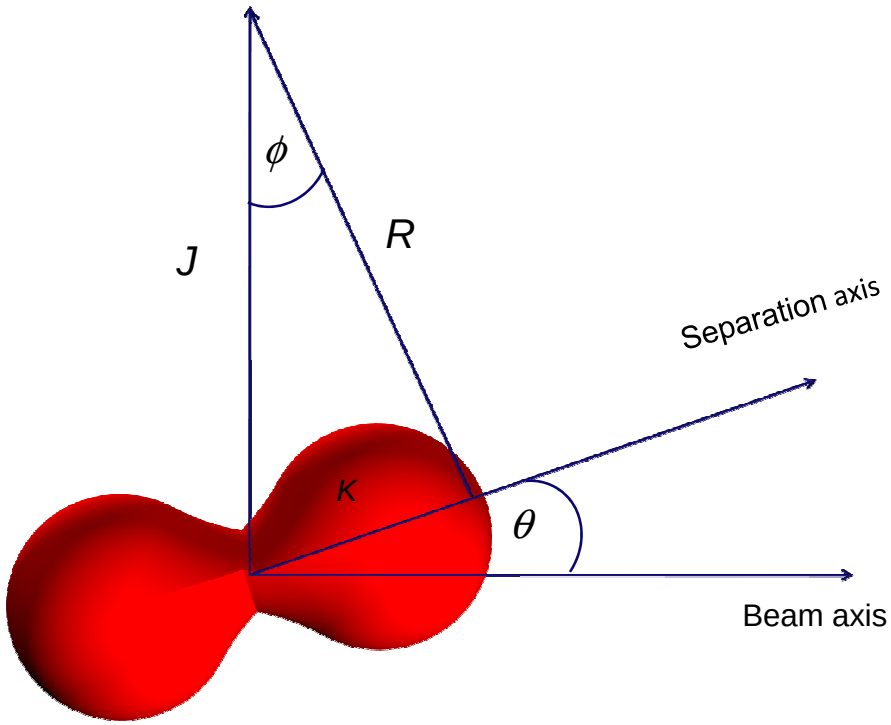

Figure 1.10: *Schematic diagram of typical fissioning system as per saddle point model. θ is the angle between fission axis and incident beam direction. Tilting angle ϕ = K/J.*

cosity by taking in to account Kramer's prescription [Kra40], decay width is modified as

$$\begin{aligned}\Gamma_f &= (\sqrt{1+\gamma^2}-\gamma)\Gamma_f^{BW} \\ &= (\sqrt{1+\gamma^2}-\gamma)\frac{1}{2\pi\rho_{gs}(E^*)}\int_0^{E^*-B_f}\rho_{sp}(E^*-B_f-\epsilon)d\epsilon \end{aligned} \tag{1.37}$$

Where γ is the nuclear viscosity given by $\beta/(2\omega_{sp})$, β is the dissipation coefficient and ω_{sp} is a measure of the potential curvature of the fission saddle point.

1.4.3 Experimental probes

Different experimental probes are used to study the equilibrium fission and non equilibrium fission processes. Details of these probes are described below.

- **Angular distribution**

  The angular distribution is a powerful tool to study the shape of the fissioning nucleus at saddle point and also the angular momentum involved in the fusion process. The final directions of fission fragments are directly related to the orientation of the nuclear symmetry axis during passage through the saddle point. This orientation is expressed in terms of the projections of total angular momentum J along the nuclear symmety axis K and along the beam axis M. In statistical saddle point model [Fre86], the fragment angular distribution $W(\theta)$ is related to the angular momentum distribution J and the width K_0 of the K distribution of the fissioning nuclei. K_0 is related to the nuclear temperature T and effective moment of inertia $\Im_{eff}$ at the saddle point. The angular distribution $W(\theta)$ for a particular J and M can be written as follows.

$$W_M^J(\theta) \propto \sum_{K=-J}^{J} T_J(2J+1)\rho_t(E_t,K)[(2J+1)/2]|D_{M,K}^J(\theta)|^2 \tag{1.38}$$

  Here θ is the angle of the symmetry axis with respect to the beam direction, T_J is the transmission coefficient, $\rho_t(\mathrm{E}_t, K)$ is the level density at the transition state, $D_{M,K}^J(\theta)$ is the rotational wave function. Based on statistical model with a constant temperature level density prescription $\rho_t(E_t, K)$ can be expressed as follows

$$\rho_t(E_t,K) \propto exp[E^* - B_f - \epsilon]/T \tag{1.39}$$

$$\rho_t(E_t,K) \propto exp\left[\frac{-E_{rot}}{T}\right] \propto exp\left[\frac{-\hbar^2K^2}{2\Im_{eff}T}\right] \propto exp\left[\frac{-K^2}{2K_0^2}\right] \tag{1.40}$$

$$K_0^2 = \frac{T}{\hbar^2}\Im_{eff} \tag{1.41}$$

$$\frac{1}{\Im_{eff}} = \frac{1}{\Im_{\parallel}} - \frac{1}{\Im_{\perp}} \tag{1.42}$$

Where E^*, B_f and ϵ are the excitation energy, fusion barrier, kinetic energy of the fission fragment, respectively. $\Im_\perp$, $\Im_\parallel$ are the moments of inertia associated with rotation around the symmetry axis and perpendicular axis. For compound nuclei formed with spin projection $M = 0$ along the beam direction and taking average over J and K, the angular distribution becomes

$$W(\theta) = \frac{\sum_{J_0}^{J_{cr}} T_J \sum_{K=-J}^{J} \frac{1}{2}(2J+1)|D^J_{M=0,K}(\theta)|^2 exp(-K^2/2K_0^2)}{\sum_{K=-J}^{J} exp(-K^2/2K_0^2)} \tag{1.43}$$

which involves summations over J and K of the symmetric-top wave function $D^J_{M=0,K}(\theta)$ and assuming a sharp-cutoff expression for the spin distribution and a Gaussian K distribution. Here J_{cr} is the critical angular momentum for fusion and the term $(2J+1)T_J$ reflects the formation cross section for a specific compound nucleus of spin J. Fission fragment angular anisotropy (A_θ) is defined as the ratio of the fragment yields along the beam direction and the perpendicular direction, i.e.,

$$A_\theta = \frac{\langle W(0^\circ)\rangle}{\langle W(90^\circ)\rangle} \tag{1.44}$$

Considering the saddle-point temperature $T = \sqrt{[E^*/a]}$ and assuming $J + 0.5 \sim J$, the anisotropy A_θ reduces as

$$A_\theta \approx 1 + \frac{\langle J^2\rangle}{4K_0^2} \tag{1.45}$$

In the case of pre-equilibrium fission, the composite udergoes fission before it attains K equilibration; this leads to larger fragment angular anisotropy [Ram90]. In the case of quasi-fission, mass equilibriation is not complete as the fission takes place from the conditional saddle point. Experimental evidence [Tok85] shows that the mass asymmetry degree of freedom equilibrates more rapidly than shape equilibration. So K equilibration may not be complete in quasi fission and

therefore larger angular anisotropy is expected, which is confirmed by several experiments [Bac85, Bac83, Hin95]. Similarly, in the case of fast-fission also, large angular anisotropy has been reported [Bac81].

- **Mass distribution**

  The fundamental property of fission is binary splitting of nucleus. As the statistical fission of the compound nucleus proceeds through shape changes over a mass symmetric unconditional fission barrier, the fission fragment mass distribution is symmetric around the average mass of the target and the projectile. The fission potential as a function of mass asymmetry can be approximated by a parabolic shape [Bac96]

$$U(A) = \frac{1}{2}k_s(A - A_s)^2 \tag{1.46}$$

  Where A is the fragment mass, A_s is the mass of the symmetric fragment, k_s is the stiffness parameter for the mass asymmetry degrees of freedom. A statistical model treatment leads to a variance of the fragment mass distribution given by

$$\sigma_A^2 = \frac{T}{k_s} = \frac{1}{k_s}\sqrt{\frac{E^*}{a}} \tag{1.47}$$

  Here T is the scission point temperature and a is the nuclear level density parameter. From the above relation it is evident that the width (or standard deviation σ_A) of the mass distribution is a smoothly varying function of excitation energy. In the case of quasi fission, as it proceeds through a mass asymmetric fission barrier, the fragment mass distribution is expected to be mass asymmetric. For a mixture of fusion-fission and quasi-fission, the mass distribution may still be peaked around the average of the projectile and the target mass, but the width of the mass distribution may become larger. Therefore, if the proportion of quasi-fission reaction increases with the change in excitation energy, there will be an

increase in the width of the mass distribution. Such an increase in the width of fragment mass distribution has been observed at near barrier energies [Gho04]. In the case of fast-fission also, there has been reports of increase in width of the mass distribution with the increase in excitation energy [Ber82, Zhe84].

- **Evaporation residue**

  The fused composite, which survives fission and releases its excitation energy by evaporating light particles and γ-rays, ends up as evaporation residue. As one moves towards the higher mass region, the competition between fission and neutron evaporation increases. The correct estimation of the compound nucleus formation cross section in a reaction involving massive nuclei is an important but difficult task. The mass distribution and angular distribution data used to estimate the fusion probability depend on the unambiguity of identification of the complete fusion reaction products among the non-equilibrium fission products. The difficulties arise when the mass and angular distributions of the non-equilibrium fission and equilibrium fission fragments strongly overlap depending on the reaction dynamics. On the other hand the observed evaporation residues in experiments are a result of the de-excitation of a heated and rotating compound nucleus. There are no evaporation residues if a compound nucleus is not formed. Therefore detection of evaporation residue gives a sensitive measure of the estimation of compound nucleus formation cross-section. The evaporation residue cross-section can be estimated as follows,

$$\sigma_{ER}(E_{cm}) = \sigma_{capture}(E_{cm}) \cdot P_{CN}(E_{cm}) \cdot P_{survival}(E_{cm}) \tag{1.48}$$

  where E_{cm} is the centre of mass energy, $P_{survival}$ is the survival probability of the ER that is determined by the competition between fission and neutron evaporation of the excited compound nucleus. P_{CN} is the probability of complete

fusion after the capture stage in the di-nuclear system. $\sigma_{capture}$ is the partial capture cross-section for the formation of the di-nucleus system in competition with other peripheral reactions like quasi-elastic processes. The partial capture cross section for the formation of the di-nuclear system is given by

$$\sigma_{capture}(E_{cm}) = \sum_{\ell=0}^{\ell_{cr}} \sigma_{capture}(E_{cm}, \ell) = \sum_{\ell=0}^{\ell_{cr}} \pi \lambda^2 (2\ell + 1) T_\ell \tag{1.49}$$

Here ℓ_{cr} is the critical angular momentum and T_ℓ is the transmission coefficient. The presence of any non-equilibrium fission process will suppress the evaporation residue formation. There have been several measurements in the actinide region, which indicate strong inhibition of evaporation residue cross-section in the presence of quasi-fission [Hin02, Sag03].

- **Neutron Multiplicity**

Since the neutrons are emitted throughout the fission path, they are generally categoried in two parts; pre-scission and post-scission neutrons. As the name suggests, pre-scission neutrons are basically the neutrons emitted before the fission takes place, whereas the post scission neutrons are emitted after fission, from the excited fission fragments. The time duration between the formation of compound nucleus to scission is generally attributed as the fission time scale, τ_f, which can be estimated from the measured pre scission neutron multiplicity, ν_{pre} as follows,

$$\tau_f = \sum_{i=1}^{\nu_{pre}} \frac{\hbar}{\Gamma_n(E^*, J_{CN})} \tag{1.50}$$

$$\Gamma_n(E^*, J_{CN}) = \frac{1}{2\pi\rho_{CN}(E^*, J_{CN})} \int_0^{E^*-S_n} \sum_{J_d=0}^{\infty} \sum_{J=|J_{CN}-J_d|}^{J_{CN}+J_d} \sum_{\ell=|j-s|}^{j+s} \rho_d(E^* - S_n - \epsilon_n, J_d) T_\ell(\epsilon_n) d\epsilon_n \tag{1.51}$$

where Γ_n, S_n, ϵ_n are the decay width, separtion energy and kinetic energy of the neutron, respectively. ρ_{CN}, ρ_d, J_{CN}, J_d are the nuclear level densities and angular momentum of the compound nucleus and the daughter nucleus respectively. E^* is the excitation energy, T_ℓ is the transmission coefficient, s, ℓ and j are the spin, orbital and total angular momenta of the evaporated neutrons. The fission timescale has been measured in a large number of systems with a wide range of excitation energies and it has been ovserved that fast-fission ($10^{-20} - 3 \times 10^{-21}$ second) and quasi-fission ($5-10\times10^{-21}$ second) timescale are shorter than that of fusion fission timescale ($\sim 5 \times 10^{-20}$ second) [Hin89]. As evident from Eq. 1.50 that, prescission neutron multiplicity can be considered as a useful probe for the study of fission dynamics. Since the time scales of nonequilibrium fission process (~saddle-to-scission time) and fusion-fission (~presaddle time + saddle-to-scission time) are likely to be different, the appearance of nonequilibrium fission at near-barrier energies should also be reflected in prescission neutron multiplicity data. Such change (decrease) in prescission neutron multiplicity with the onset of quasifission has been observed [Don99].

In addition to the above mentioned probes, there are a few combinational probes which are also used to study fission dynamics, such as, mass angle distribution [Tok85, She87, Hin08] and mass energy distribution [She87, Chi03].

Although there are many available probes for the identification of different non equilibrium fission processes as discussed above, however, the identification of particular kind of reaction mechanism is not always quite unambiguous. A very interesting case in point is ^{16}O + ^{238}U system, which is a highly fissile, deformed system and therefore is a probable candidate for quasi-fission at near barrier energies. Anomalous behavior of fission fragment angular anisotropy has been observed for this system at near barrier energies, which indicates significant contribution from non-compound

nuclear fission. By assuming that the effect of quasi-fission will be predominant in the sub-barrier region, where the orientation of the deformed target-projectile system will be crucial to determine the fusion trajectory, Hinde et. al. [Hin95] explained the anomalous energy dependence of the fragment anisotropy for ^{16}O + ^{238}U system and concluded that there is quasi-fission transition at sub-barrier energies. On the contrary, the cross-sections of the evaporation residues (ER) measured for the same system at near and sub-barrier energies have been reported to be consistent with the statistical theory [Nis04], indicating that the contribution from non-compound fission (say, QF) is not significant. So, Nishio et. al. [Nis04] have proposed that the observed anomalous fission fragment angular distribution may be due to the contribution from another competing mechanism, pre-equilibrium fission [Ram85]. Two measurements performed using different probes, conjecture different reaction mechanism. In this thesis work ^{16}O + ^{238}U system was reinvestigated using other available probes to elucidate reaction mechanism.

1.5 Motivation and structure of the thesis

The main motivation of the present thesis is to (i) study some of the important features of low energy nuclear reaction using neutron as a probe, and, (ii) design and development of related detectors and instruments. More specifically, this plan of the work can be categorised as follows,

- Design, development and characterisation of neutron detectors for the measurement of neutron energy and multiplicity. A major detector development program has been taken up within this thesis work. The main criteria in this development is to achieve high efficiency and good pulse shape discrimination ability of the detector to discriminate γ rays. Liquid scintillators are found to be the suitable

candidate. Liquid scintillator BC501A was used to fabricate detectors for neutron energy measurements. Neutron energy was measured using time of flight technique. For multiplicity measurement, a detector consisting of 500 litres of liquid scintillator BC521 (0.5% Gd loaded) was built. In the multiplicity detector, neutron detection is based on thermalisation followed by (n,γ) capture reaction.

- Study of the dynamics of fission (fusion fission vs quasi fission) in heavy tranuranic systems using neutron and other available probes. ^{16}O + ^{238}U system has been chosen, based on the two different conjectures of earlier experiments. There are two earlier measurements on ^{16}O + ^{238}U system at near barrier energies. Angular distribution measurement claimed the presence of quasi-fission [Hin95]. Whereas the evaporation residue measuremnt conjecture the presence of pre-equilibrium fission [Nis04]. In this thesis work ^{16}O + ^{238}U system has been reinvestigated using fragment mass distrubtion and neutron to understand the reaction mechanism in near barrier energies.

- Study of neutron evaporation spectra to extract the nuclear level density parameter and explore its dependence on angular momentum. The excitation energy dependance of nuclear level density is well studied but the angular momentum dependance is not well known. There are few experiments in recent years [Gup08, Gup09], however no systematic dependance of NLD has been observed. In this thesis work ^{119}Sb was chosen which will decay predominantly by neutron evaporation. ^{119}Sb was populated through light ion route to ensure the formation of one major residue. Evaporated neutrons were detected in coincidance with γ-ray multiplicity. The measured neutron spectra were analyse using statistical model to extract nuclear level density and study its dependance on angular momentum.

The thesis has been divided in five chapters. Chapter 1 contained a detailed survey and physics motivation of the thesis work. The details of neutron detector development and characterisation have been discussed in chapter 2. The fission dynamics study in ^{16}O + ^{238}U reaction have been described in chapter 3. The neutron evaporation study in ^{4}He + ^{115}In reaction have been presented in Chapter 4. Finally, summary and conclusion of the present thesis have been presented in chapter 5.

Chapter 2

Detector development

2.1 Introduction

The detection of neutron is more difficult (or rather indirect) than the detection of charged particles since it is uncharged in nature. Neutrons are generally detected through nuclear reactions that result in prompt energetic charged particles such as proton, alpha particle and so on. Because the cross section for neutron interaction in most material is a strong function of neutron energy, rather different techniques has been used for neutron detection in different energy region. The most important process for the detection of fast neutrons (neutron Energy $\sim$ 0.1 MeV -100 MeV) is elastic scattering of neutron with proton in a hydrogenous material. Similarly for slow neutrons (neutron energy $\sim$ eV) different nuclear reaction, such as ^{3}He(n, p), ^{6}Li(n, α), ^{10}B(n, α), neutron capture in ^{155,157}Gd and neutron induced fission in ^{235}U are generally used. The nuclear reactions used for the detection of slow neutron can in principle be used for fast neutron also, however the detection efficiency will be extemely poor. This inherently low detection efficiency for fast neutrons can be somewhat improved by surrounding the detector with hydrogen containing moderating material.

Under this thesis work we have developed two types of neutron detectors for neutron energy and multiplicity measurements. The detectors developed for energy measurement using time of flight technique are small volume (1.5 litres) liquid scintillator detectors, whereas the neutron multiplicity detector is Gd loaded large volume (500 litres) liquid scintillator detector, which used the neutron capture γ-rays to meausre the multiplicity. This chapter describes the details of these developments.

2.2 Neutron time of flight detector

The Time-of-flight (TOF) technique is a general method for determining the kinetic energy of a travelling neutron, by measuring the time it takes to fly between two fixed points separated by a fixed distance. Liquid scintillator based detectors are widely used for neutron energy measurement using time of flight technique due to their properties like relatively high light output, good detection efficiency, fast decay time and excellent neutron gamma ($n - \gamma$) discrimination. Among the available scintillators, BC501A (or equivalently NE213) has been demonstrated to have very good pulse shape discrimination capability and good time resolution [Kle06, Kle02, Hor00, Rob81, Ahm77, Win71]. The TOF technique can provide a good neutron energy resolution compared to other spectroscopy techniques.

2.2.1 Scintillation mechanism

Liquid scintillators mainly consist of aromatic hydrocarbons, with small admixtures of other molecules. In aromatic hydrocarbons two types of chemical bonds are important, σ bond and π bond. The σ bonds are the normal regular tetrahedron bonds of carbon and they do not contribute to the luminesence of the liquid, whereas the π bonds cause double and triple bonds and are responsible for the luminesence. In aro-

matic hydrocarbons there are many "p" orbitals which make up a delocalised π system that can be modeled as free electron orbiting the nucleus. The scintillation light comes from transitions of molecular valence electrons between different energy levels. The energy levels are separated into spin singlet levels (S_0, S_1, S_2 ...) and spin triplet levels (T_1, T_2 ...). Every molecular energy level has associated vibrational energy levels, (S_{00}, S_{01} ...; S_{10}, S_{11} ...) and (T_{10}, T_{11} ...) (see Fig. 2.1). The energy difference between molecular energy levels is of the order of $\sim$ 3 eV, while the difference between vibrational energy levels is $\sim$ 0.1 eV. When ionizing radiation passes through the scintillator, the molecules may absorb a fraction of the energy with their π orbital electrons via transitions from the ground state to higher energy levels. Electrons excited to higher energy levels rapidly (few $\sim$ ps) fall back to the S_1 level via radiationless de-excitation.

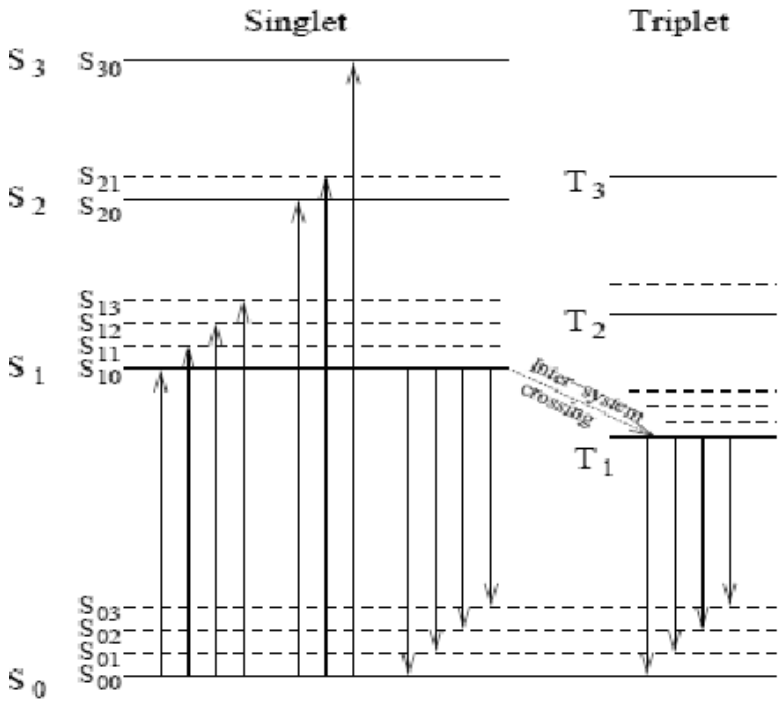

Figure 2.1: *Typical energy levels diagram of an organic scintillator.*

Scintillation light is emitted due to the de-excitation of electrons from S_1 level to one of the vibrational states of the ground state S_0 (fluorescence). This type of transition occurs with decay times ~ ns, corresponding to the fast component of the scintillation light pulse. The other possibility is an inter-system crossing decay. In this case, the electron in S_1 level crosses to T_1 level and from there this molecule interacts with an other molecule with an electron in T_1 state. The result of such an interaction leaves one molecule in the S_1 state and the other in the S_0 state. The life time of T_1 (~ ms) is characteristically much longer than that of S_{10}. So the radiation emitted (phosphorescence) in the deexcitation does not contribute to the pulse produced by the prompt fluorescence. However, instead of a transition to S_0, some of the molecules can be excited back to S_{10} and then decay to S_0, which is called delayed fluorescence. Decay time in this case is ~ 100 - 500 ns. The scintillation light is the superposition of two or more exponential decay components with different decay time constants. Delayed fluorescence constitutes the slow component of the scintillation light and is mainly responsible for the neutron gamma discrimination property of liquid scintillator.

2.2.2 Properties of liquid scintillator BC501A

BC-501A (manufactured by M/s Saint-Gobain) is one of the popular liquid scintillators used world wide for neutron detection. This liquid scintillator is based on xylene or dimethylbenzene, $C_6H_4(CH_3)_2$. Some of the important properties of BC501A are described in the Table 2.1. The neutron detection mechanism of BC501A scintillator detector is based on elastic scattering of neutron with proton, which strongly dominates over the other reaction channels in the energy range 0.1 -8 MeV region. At around 8 MeV, different inelastic channels gradually come up and they start playing significant roles in the detection mechanism. Different nuclear reactions of neutrons

with proton and carbon are shown in Fig. 2.2 for the neutron energy range 0.1 MeV to 30 MeV [Rei04].

Table 2.1: *Properties of liquid scintillator BC501A.*

Scintillator Properties	BC501A
Light output, % Anthracene	78
Wavelength of maximum emission, nm	425
Decay time of short component, ns	3.2
Ratio H:C atoms	1.212
Number of electrons per cc	2.87
Density, gm/cc	0.874
Refractive Index at 425nm	1.530
Flash point, T.O.C. /°C	24
Scintillator decay time	3.16 ns, 32.3 ns & 270 ns

Light output response: Generally the light output of a scintillator depends on the type and energy of the incident particle. Typical light output responses of liquid scintillator BC501A for different ionizing radiations are shown in Fig. 2.3. Birks had first expressed the differential light output from scintillators in terms of the specific energy loss, dE/dx of the charged particles, which was later improved by adding extra parameters. The light output as a function of incident particle energy may be expressed as [Cra70].

$$L(E) = \eta \int_0^E d\epsilon[1 + KB(dE/dx) + C(dE/dx)^2)]^{-1} \tag{2.1}$$

Where η is scintillator efficiency, dE/dx specific energy loss, K, B and C are constants. In the case of electrons, the light output is almost linear for electron energies $E_e \geq 40$ KeV [Die82]. However it shows non linear response to proton and higher charged particles. The other alternative approach to describe scintillation light output is the phenomenological type, proposed by Cecil et. al. [Cec79]. In this approach scintilla-

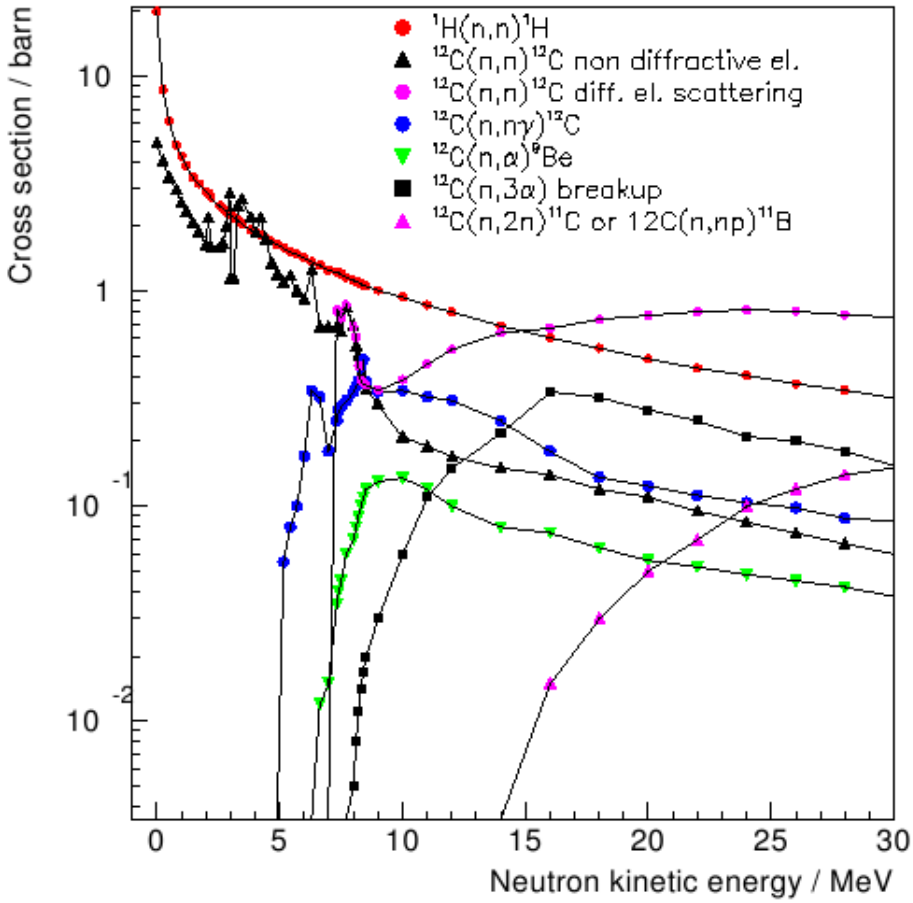

Figure 2.2: *Different nuclear reactions of neutrons with proton and carbon in the neutron energy range 0.1 MeV to 30 MeV [Rei04]*

tion light is expressed as a function of energy of different ionizing radiation as follows,

$$L(E) = a_1 E - a_2(1 - e^{-a_3 E^{a_4}}) \tag{2.2}$$

The parameters a_1, a_2, a_3, and a_4, extracted by fitting the experimental data are shown in Table. 2.2.

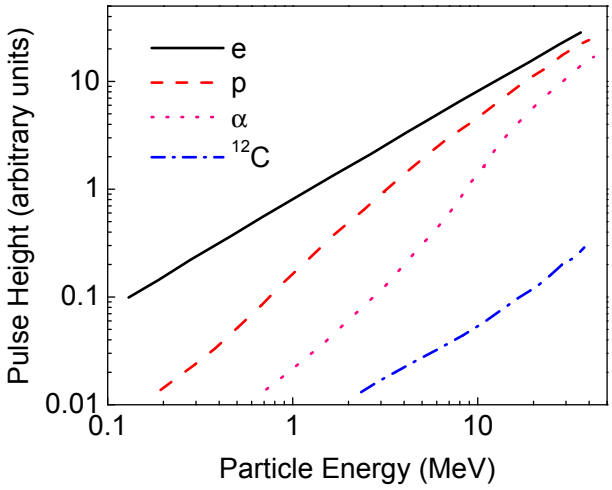

Figure 2.3: *Typical light output of different ionizing radiation for liquid scintillator BC501A.*

Table 2.2: *Description of the parameters for different charged particles produced in liquid scintillator BC501A.*

Particle	a_1	a_2	a_3	a_4
Proton	0.83	2.82	0.25	0.93
alpha	0.41	5.9	0.065	1.01
Carbon	0.071	0	0	0

2.2.3 Design consideration and simulation study

To perform the experiments as discussed in the Chapter 1, the neccessary neutron TOF detectors have been developed indegenously. Another intention behind this development was to make a case study to select suitable detector element for building a neutron time of flight spectrometer, to cater to the needs of new experimental programme using the upcoming K500 superconducting Cyclotron at VECC. The neutron energy range considered for the present development is 0.5 MeV - 25 MeV. The main design considerations for the detector development were,

- High detection efficiency.
- Low sensitivity to gamma radiation and background events.
- Neutron-gamma discrimination capability, because of neutron emission often competes with gamma de-excitation.
- Modularity, in order to distinguish between single and multiple neutron emission events.
- Resonable energy resolution.

The intrinsic efficiency is clearly proportional to the volume or thickness of the cell while the energy resolution depends inversely on the thickness for a given flight path. Commercially available phototubes of 5" diameter were considered as the largest acceptable ones. Simulation using *GEANT*4 has been performed to study the efficiency of detector having different length and 5" diameter.

Simulation of neutron detector: We have used GEANT4 [Ago03] version 4.9.2 and neutron data library G4NDL3.14 for the present simulation. All possible processes of light production inside the detector, including the effects of metallic casing of the detector, detector resolution and non-linear light responses of all secondary charged particles, have been taken into account. The photomultiplier tube has, however, been ignored in the simulation. The simulation is based on a series of *GEANT*4 classes, each responsible for a given step of the simulation, like the detector geometry and material building, particle and physics processes definition, particle tracking, hit definition and handling. Individual neutrons are randomly generated by a particle generator and tracked through the detector volumes. ParticleGun class was used to generate the primary events. *GEANT*4 tracks the particle and provides necessary tools to extract the parameters of particle tracking. In this simula-

tion, the charged particles produced and the scattered neutrons are tracked until they deposit all their energy in the defined detector volume or go out of the “World" volume, which encompasses the entire detector geometry. In the PhysicsList, the neutron induced interactions have been simulated using the high precision neutron specific model (NeutronHP), where the major low energy interactions of neutrons have been broadly treated in four categories, i.e., radiative capture, elastic scattering, fission and inelastic scattering. Each category of reaction has been simulated with separate class (G4NeutronHPElastic, G4NeutronHPInelastic, G4NeutronHPCapture and G4NeutronHPFission, respectively), using the cross-section data library G4NDL3.14. The scintillation light output from the energetic secondary charged particles produced by the neutron interaction has been estimated using Cecil’s prescription [Cec79]. Simulation has been performed with pencil neutron beam. Estimated detection efficiency as a function of neutron energy for neutron detectors of different sizes are shown in Fig. 2.4.

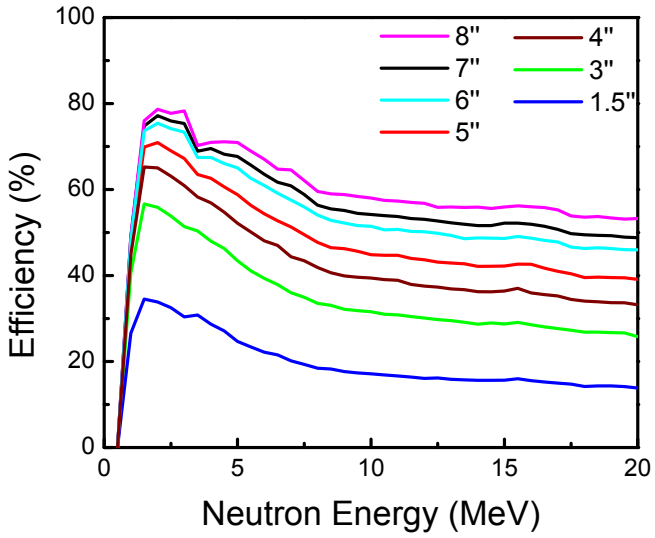

Figure 2.4: *GEANT4 simulation of detection efficiency as a function of neutron energy for detector of different sizes (diameter 5 inch, lengths of detectors are mentioned in the graph).*

2.2.4 Detector Fabrication

Based on the above study four different sizes of neutron detectors (length × diameter : $1.5'' \times 5''$, $3'' \times 5''$, $5'' \times 5''$, $7'' \times 5''$) were designed and fabricated for the study of different characteristics properties of neutron detector and their variation with detector dimension. The detector cells, cylindrical in shape, were made up of 2 mm thick stainless steel and filled with liquid scintillator BC501A. Internal walls of the cells were white painted for efficient light collection. The scintillator liquid was thoroughly flushed with dry nitrogen gas of purity (99.999%) for sufficient time to remove any dissolved oxygen present in the liquid [Beg06]. A small expansion chamber (10% of the detector volume) was coupled to the detector to take care of the thermal expansion of the liquid. Scintillator cells, sealed with 6mm thick pyrex glass, were viewed by 5 inch photo multiplier tube (PMT) (model: 9823B; Electron tube Ltd). The photo multiplier tubes were provided with 1 mm thick μ- metal shield to protect them from magnetic field. The PMT and the voltage divider were covered with a cylindrical container, which held the PMT rigidly in position and also provided light tightness. The fabricated neutron detector cells are shown in the Fig. 2.5a.

The design of the neutron detector was further improved. The new cell is now made up of 1.5 mm of aluminium and expansion chamber was made up of teflon capilary tube (inner diameter = 1.5mm, outer diameter = 2.5 mm), which was rolled around the neutron cell. The cylindrical surface of the cell was encapsulated in an aluminium cover. The new detector cell is shown in Fig 2.5b. This new cell will be used in proposed time of flight array.

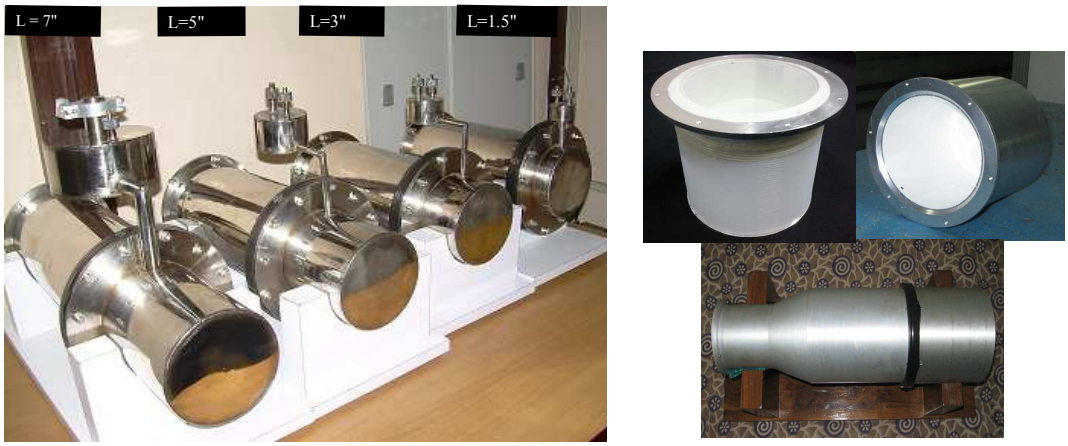

(a) (b)

Figure 2.5: *(a) Neutron detectors of different sizes used in present work., (b) detector with compact design.*

2.2.5 Calibration procedure

Since the mono energetic neutron sources are not readily available, the calibration of the liquid scintillator detector is usually done by standard γ-ray sources with known energies ^{137}Cs (E_γ = 662 keV), ^{22}Na (E_γ = 511 keV, 1274.5 keV). As the pulse height response does not contain pronounced full energy peaks (except for energies < 100 keV) the calibration procedure relies on the analysis of the Compton edge. This process results in a recoil electron, which carries a large fraction of the incident γ energy depending on the angle of scattering,

$$E_e = \frac{E_\gamma^2(1 - cos\theta)}{m_o c^2 + E_\gamma(1 - cos\theta)}, \tag{2.3}$$

where E_e, E_γ, θ are the scattered electron energy, incident γ-ray energy and scattering angle, respectively, m_o is the rest mass of electron and c is the velocity of light. The recoil electron will have maximum energy at head-on collision, which is known as Compton edge, E_C, where

$$E_C = \frac{2E_\gamma^2}{m_o c^2 + 2E_\gamma} \tag{2.4}$$

E_C is usually expressed in MeV electron equivalent, i.e. MeVee. Because of the dependence of the light yield of organic liquid scintillator on the type of particle, the term MeV electron equivalent is introduced to place the light yield on the absolute basis. The determined Compton edge for the corresponding E_C provides a calibration curve presented in Fig. 2.6, which shows good linearity. But the determination of Compton

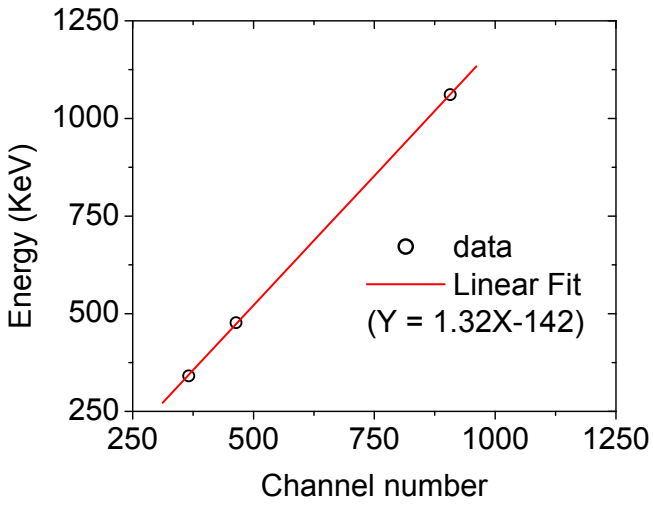

Figure 2.6: *Pulse height calibration curve using standard γ sources.*

edge is not always unambiguous due to the finite pulse height resolution of the detector, which is particularly more severe with the increase in detector dimension. This problem was solved by Dietze and Klein [Die82]. They proposed a state-of-the art method, which is based on fitting the theoretical response function to the measured pulse height distribution. This is illustrated in Fig. 2.7. The blue line is the ideal response function for ^{137}Cs γ-ray source calculated by means of the Monte Carlo code PHRESP [Nov97] for a $5'' \times 5''$ detector. This distribution is folded (red line) with a Gaussian having FWHM corresponding to the pulse height resolution of the detector ΔL, which can be expressed as

$$\frac{\Delta L}{L} = \sqrt{\alpha^2 + \frac{\beta^2}{L} + \frac{\gamma^2}{L^2}} \tag{2.5}$$

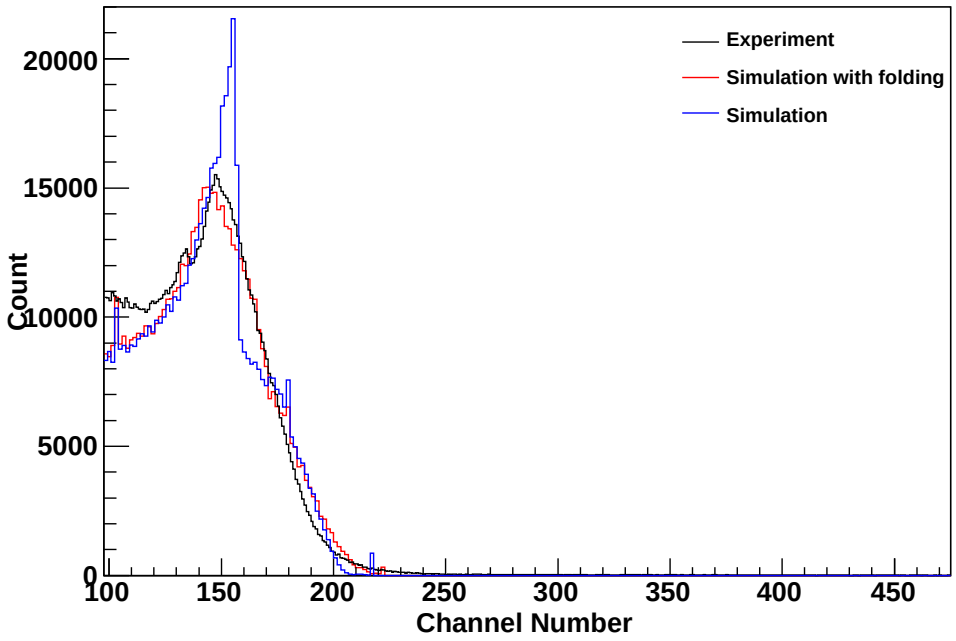

Figure 2.7: *Pulse height response of liquid scintillator BC501A based detector for* ^{137}Cs γ *source.*

The first term represents the locus dependent light transmission from the scintillator to the photo cathode, the second term is for statistical variation of the conversion of light to photo electrons, and the third one is due to noise contributions from the dynode chain [Die82, Dek87]. The folded pulse height distribution is then expanded or compressed in both x and y axes (red line) in order to fit the measured pulse height distribution (black line). The scaling factor in the x-axis (in channels/MeVee) gives the relation between the pulse height and the light output. The pulse height resolution obtationed in this case is 10%.

2.2.6 Variation of neutron detector characteristics with detector dimension

The most important characteristics of neutron detector are efficiency, neutron gamma discrimination and intrinsic time resolution. All these properties are sensitive to detector dimension. The neutron gamma discrimination property is degraded with the increase in detector dimension [Kal70, Mos94]. The same is also true for the intrinsic time resolution; on the contrary, the neutron detection efficiency improves with the increase in detector dimension. Thus it is important to make a systematic study of the variation of these properties as a function of detector volume to optimize the detector design as per requirement. While modern calculational tools are quite well suited for the estimation of efficiency for neutron detector, the neutron gamma discrimination capability and intrinsic time resolution can only be studied experimentally. In the following sections, we will discuss a comprehensive study of all these important properties measured with same set of detectors.

Efficiency: Efficiency measurement has been performed using associated particle technique [Rid74]. 6 μCi ^{252}Cf was mounted on the back plane of a (20 cm x 6 cm) position sensitive multiwire proportional counters (MWPC) [Gho05], which detects the fission fragments. Neutron energy was measured using time of flight method with the start from MWPC and the stop from liquid scintillator detector. MWPC is shown in Fig. 2.8. There was five wire planes (electrodes), one anode (A), two sense wire planes (X, Y) and two cathode (C) wire planes. Schematic diagram of MWPC is shown in Fig. 2.9. Separation between successive electrodes is 3.2 mm, the electrodes are made of 20 μm thick gold plated tungsten wires. The X and Y sense wire planes were perpendicular to each other and were made of 50 μm diameter gold coated tungsten wire, placed 2 mm apart. All the wire planes were made of G - 10 quality double sided glass epoxy, copper plated printed circuit boards (PCB). Gas detectors were isolated from

the vacuum chamber using 1 μ Mylar foil. The foil is supported by a grid of aluminum wire of 0.5 mm diameter at a separation of 15 mm. The MWPC was operated with Isobutane gas maintained at a pressure of 2 torr with the help of an electronically regulated gas flow system. Since the detector was operated at very low pressure, it was insensitive to alpha particles emitted from ^{252}Cf source. For each fission event, one of the resulting fission fragments was emitted within the active volume of the detector, which enabled the MWPC to detect almost every fission event. The MWPC with ^{252}Cf source was kept within a vacuum chamber having a 3 mm thickness flange in front of the neutron detector. The experimental arrangement has been shown schematically in Fig. 2.10.

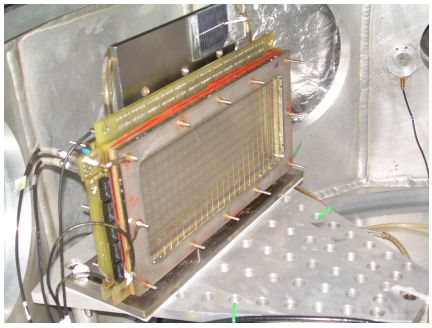

Figure 2.8: *Photograph of MWPC used in the efficiency measurement.*

The neutron detector was kept at a distance of 150 cm from the MWPC. Low energy neutrons can be discriminated from the γ-rays by TOF. However, finite flight path of the TOF spectrometer poses a constraint for comparatively higher energy neutrons. High energy neutrons can be readily distinguished from the γ-rays by neutron-γ pulse shape discrimination technique, which also eliminates the background arising from the γ rays following inelastic neutron scattering and neutron capture in the surrounding medium. Hence a combination of these two techniques enabled good discrimination between neutron and γ-ray induced events for both high and low neutron energies. The other background (neutron scattering from air, wall etc) was measured by inserting a

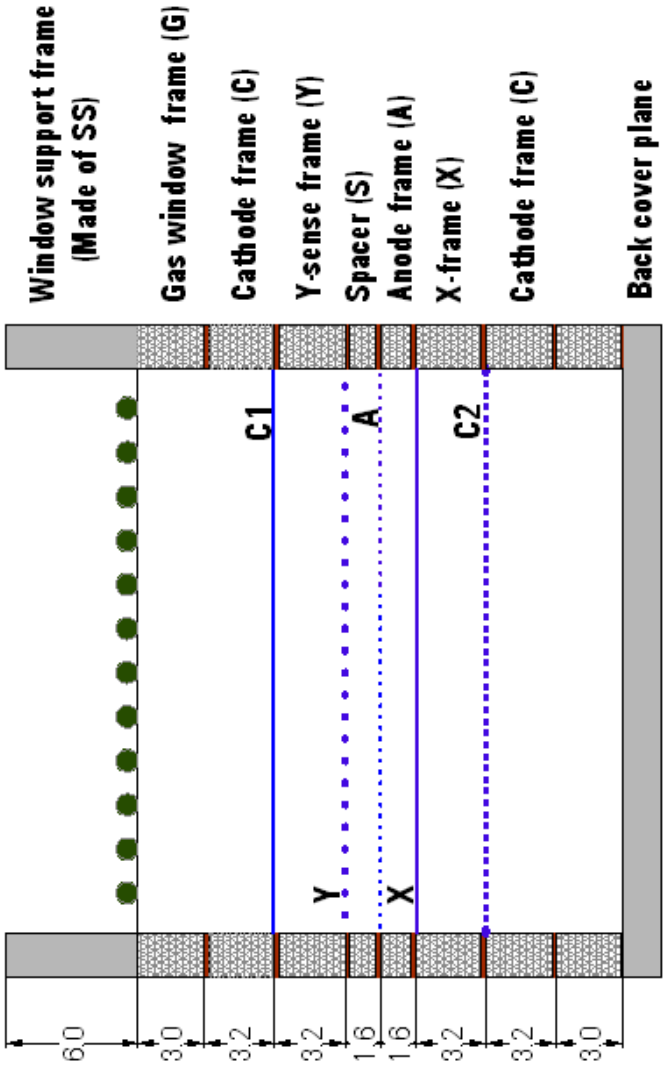

Figure 2.9: *Schematic design of MWPC.*

shadow bar of concrete (20 cm in breadth and height and 60 cm long) in between the MWPC and neutron detector. The readout electronics and data acquisition setup has been shown in Fig. 2.11. The signal from the central anode wire plane of MWPC was fed to a wide bandwidth voltage sensitive pre amplifier followed by a constant fraction discriminator (CFD) to generate the MWPC timing signal. Neutron detector signal was directly connected to another CFD, to generate corresponding timing signal. The CFD timing output of MWPC was used as start input of the Time to Digital converter

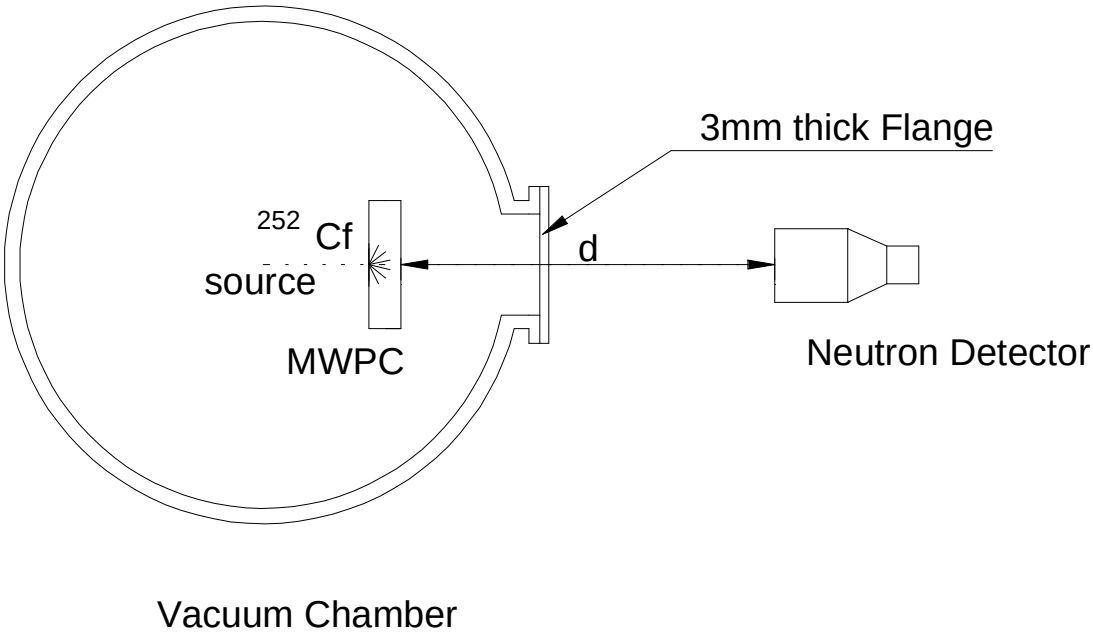

Figure 2.10: *Experimental setup for detection efficiency measurement.*

(TDC) and the delayed timing output of the neutron detector was used as stop. Neutron detector threshold was kept at 100 KeVee. Pulse shape discrimination was achieved by zero cross over (ZCO) technique [Spe74]. The difference between the CFD and the ZCO timings was measured with a Time to Amplitude Converter (TAC) which is further connected to ADC. Energy signal of the MWPC was connected to pre amplifier followed by an amplifier and finally connected to ADC. The neutron detector pulse height, the neutron γ discrimination signal and the neutron time of flight, fission fragment energy loss in MWPC were stored on event by event basis using CAMAC based online data acquisition system [Ban87].

A typical two-dimensional scatter plot of time of flight (TOF) vs zero cross over time (ZCO) for neutrons as well as γ- rays emitted from ^{252}Cf is shown in Fig. 2.12. It is clear from Fig. 2.12 that neutron and gamma events are very well separated in this plot.

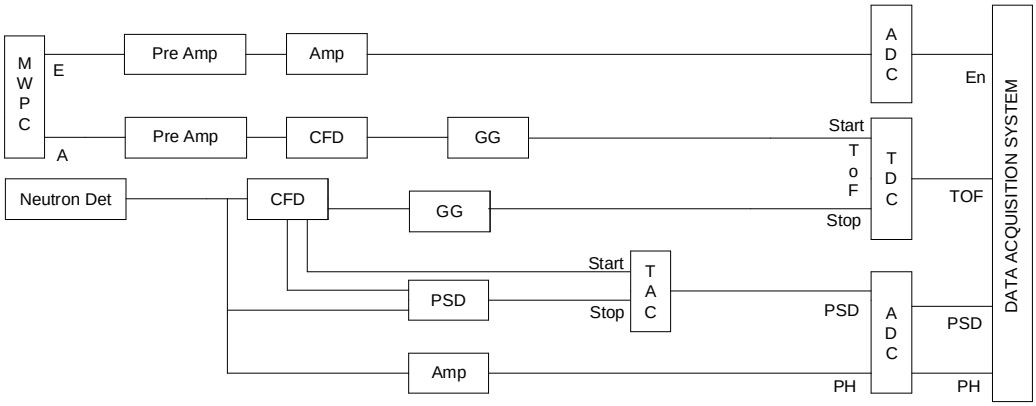

Figure 2.11: *Block diagram of the electronics for detection efficiency measurement.*

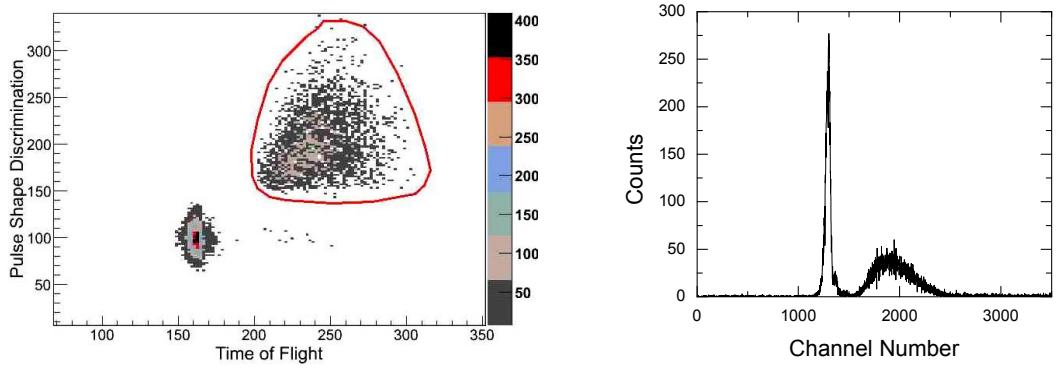

Figure 2.12: *2-D plot of TOF vs ZCO time (left), TOF spectrum (right).*

Genuine neutron events were extracted by using a two dimensional gate (Fig. 2.12). The prompt γ-ray peak in the TOF spectra was used as time reference. Neutron energy spectra were then obtained from the TOF spectra using proper Jacobian transformation. Data have been corrected for background, measured with shadow bar technique. Standard ^{252}Cf source spectrum taken from reference [Kno00], properly normalised with neutron multiplicity $\nu = 3.77$, the neutron detector solid angle and the total number of fission detected, corrected for dead time loss. The reference neutron energy spectrum thus obtained was then compared with the experimental spectrum to obtain the absolute energy dependent neutron detector efficiency. Measured efficien-

cies as a function of energy for individual detectors are shown in Fig. 2.13, where the errors represent sum of statistical and systematic errors. Systematic errors are estimated to be ~ 2 %.

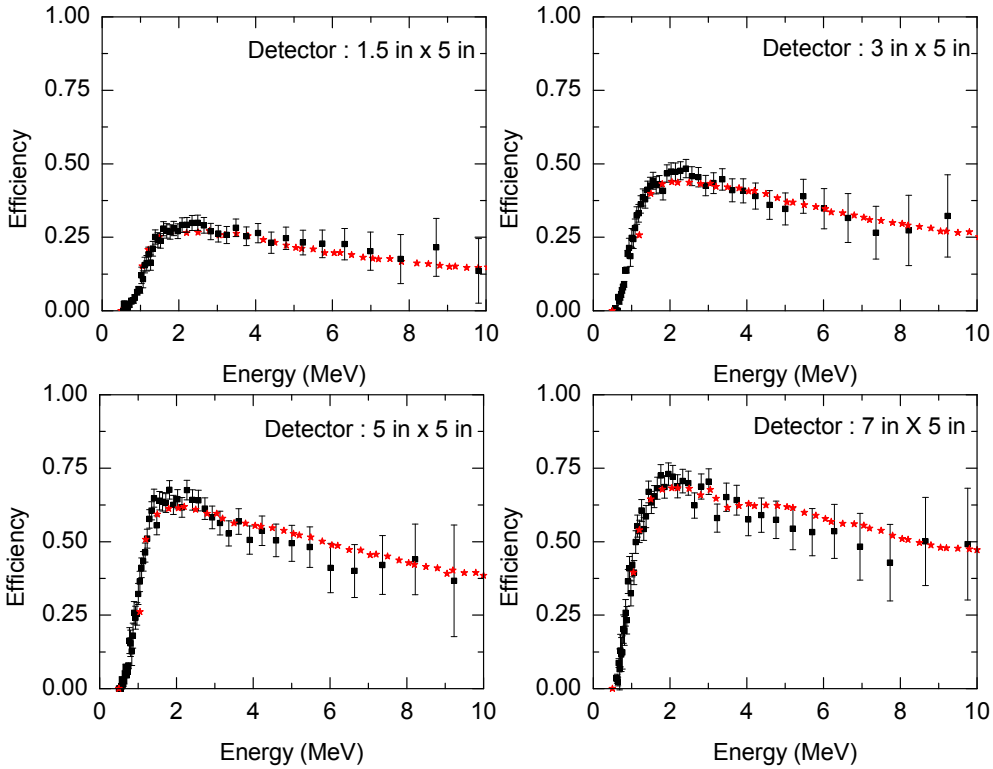

Figure 2.13: *Absolute efficiencies as a function of energy for different sized detectors. Square (black) symbol shows the experimental result and star symbol (red) shows the GEANT4 simulation.*

It is observed that the efficiency, as expected, increases with the increase in detector dimension. Bigger the detector size, (compared to the interaction mean free path of neutron in the detection medium) higher is the probability of interaction of neutrons with detector and so is efficiency. The measured efficiencies were compared with the corresponding GEANT4 simulation. It is evident from Fig. 2.13 that, the measured efficiencies are in good agreement with the simulations in all cases over the whole range of neutron energies.

Neutron gamma discrimination : This is also known as pulse shape discrimination. Organic scintillators, particularly BC501A are well known for their good Pulse Shape Discrimination (PSD) properties. PSD is possible due to the variation of the long-lived decay component of scintillator light with the specific energy losses (dE/dx) of the different particles in the detector material. Fig. 2.14 illustrates the shape of the emitted light pulse, which can be described by a single fast decay component and a substantial slow component. The quality of the $n - \gamma$ discrimination is assessed

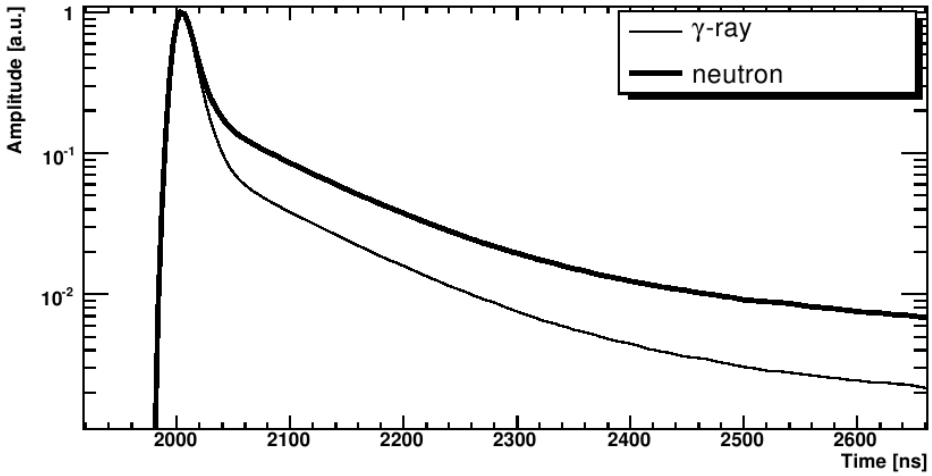

Figure 2.14: *Typical pulse shape of liquid scintillator BC501A for γ ray and neutron interaction [Sod08].*

quantitatively by the Figure of Merit (FOM), which is defined as,

$$M = \frac{\Delta}{\delta_n + \delta_\gamma} \tag{2.6}$$

where Δ is the separation between the γ peak and the neutron peak, δ_γ, δ_n are the full width at half maximum of γ and neutron peaks, respectively. Pulse shape discrimination (PSD) setup is already discussed in the earlier section. PSD measurement was repeated with 30 mCi ^{241}Am-^{9}Be source. Among others, ^{241}Am-^{9}Be source emits 4.44

MeV gammas from the first excited state of ^{12}C. Pulse shape discrimination spectra for different sizes of BC-501A detectors are shown in Fig. 2.15.

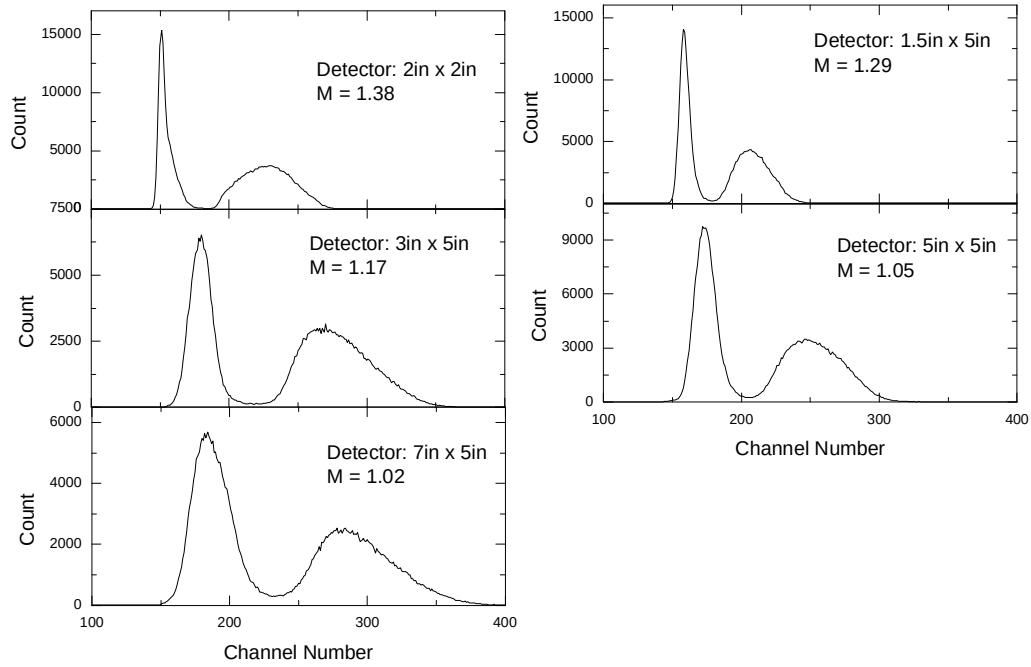

Figure 2.15: *Pulse shape discrimination spectra of different sizes of liquid scintillator based neutron detectors for ^{241}Am-^{9}Be source, threshold ~ 350 keVee.*

The figures of merit (M) for all detectors, obtained using Eq. 2.6, have been summarized in Table. 2.3. It is seen that the figure of merit M decreases with the increase in detector size. This can be intuitively understood as follows; the larger detectors are associated with larger loss of light and also larger time spread of the arrival of photon at the PMT; both of these cause broadening of neutron-γ PSD distribution. However it is seen that even for the largest detector (7$^{''}$ long) used in this work, neutron and gamma peaks are well separated. The figures of merit has been extracted for different pulse height, which are shown in Fig. 2.16. Figure of merit initially increases with pulse height and then saturates. The decrease in the figure of merit on neutron-γ discrimination at lower pulse height is due to low photo electron statistics.

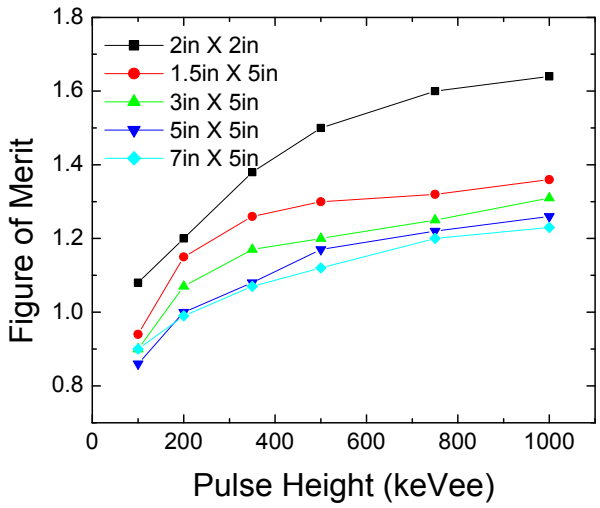

Figure 2.16: *Figure of merit vs pulse height for different sized detectors.*

Intrinsic Time Resolution: Intrinsic time resolutions of the liquid scintillators for γ -ray detection have been measured with the help of BaF_2 detector (dimension 5 cm $\times$ 3.5 cm $\times$ 3.5 cm; time resolution (FWHM = 400 psec) as start detector, using the experimental setup shown in Fig. 2.17. A ^{60}Co source was kept in between the BaF_2 detector and the neutron detector. The separation between the BaF_2 detector and the neutron detector was 20 cm. Thresholds of the two detectors were $\sim$ 30 KeV. PSD and time resolution measurements were also carried out with a commercially available BC501A liquid scintillator detector (2" diameter, 2" length) for comparison purpose. The timing spectra of the detectors measured with ^{60}Co source have been shown in Fig. 2.18. The intrinsic time resolutions for different size detectors are displayed in Table. 2.3. It is observed that the smaller the size of the detector, the better is the time resolution.

This may be chiefly due to the fact that both time jitter and time walk increase with the increase in detector volume and decrease in pulse amplitude. However in the case of neutron measurement the time response is mainly determined by the transit time of neutron within the detector [Kle06]. Transit time of neutron in the detector

Table 2.3: *Measured values of different parameters in all detectors*

Detector dimension length x diameter in inch	Detector volume in litre	M-Value Threshold at 350 keVee	Time resolution (FWHM) in psec	Efficiency in % Threshold = 100keVee		
				2 MeV	5 MeV	10 MeV
1.5×5	0.50	1.26	1446 ± 39	29± 2.5	23 ± 4	13 ± 11
3×5	1.01	1.17	1477 ± 56	47 ± 2.8	35 ± 5	30 ± 16
5×5	1.66	1.08	1538 ± 42	64 ± 3	49 ± 6	37 ± 20
7×5	2.36	1.07	1569 ± 46	72 ± 3.8	54 ± 7	49 ± 20

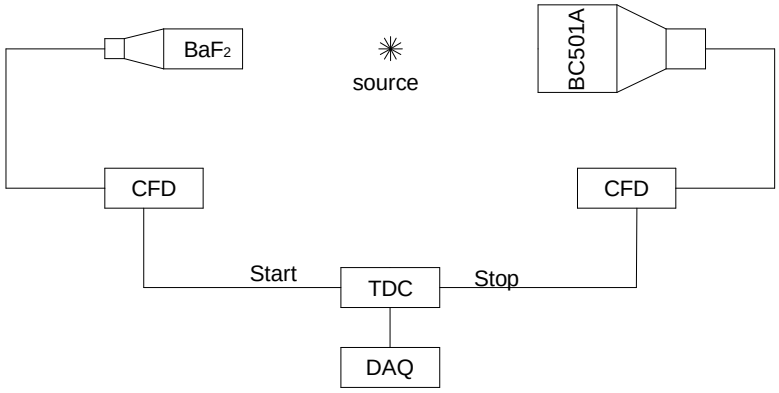

Figure 2.17: *Experimental setup for γ-γ-coincidence measurements to determine the intrinsic time resolution.*

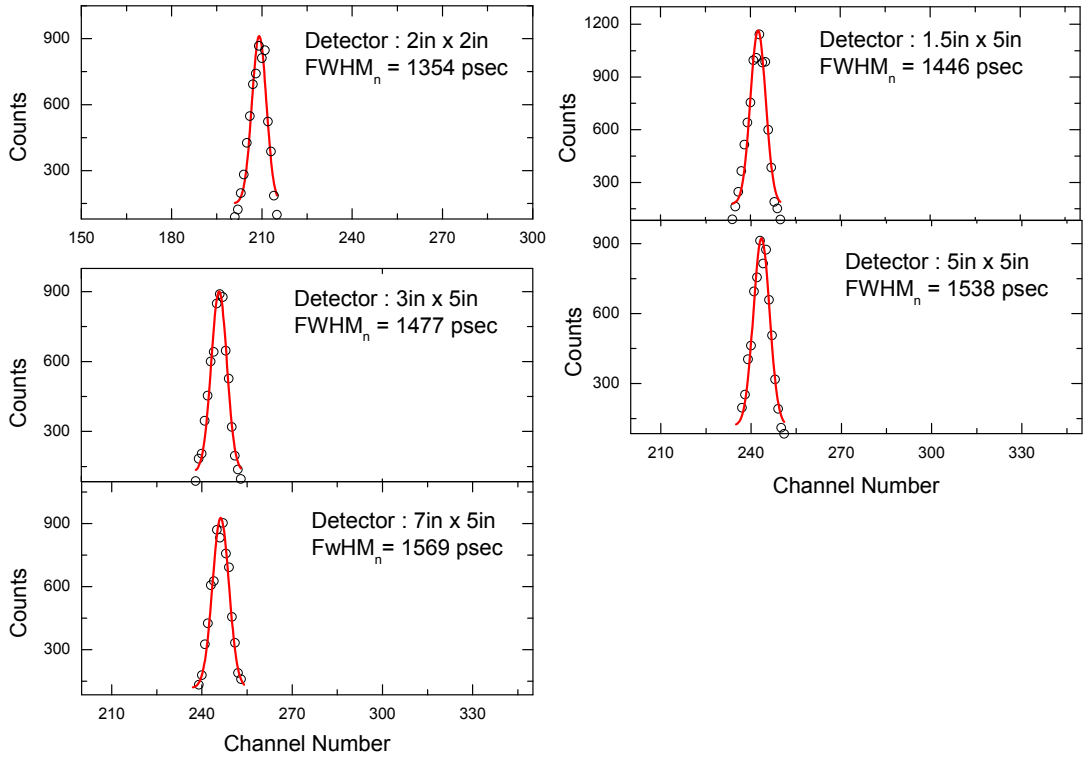

Figure 2.18: *Time resolution spectra of different sizes of liquid scintillator based neutron detectors using ^{60}Co source, detector threshold ~ 30 keVee. Solid circle shows experimental data, line shows Gaussian fit.*

is generally estimated using Monte Carlo simulation technique [Die82a]. A simulated time response matrix is used to unfold the measured TOF spectrum. Transition time is sensitive to flux attenuation and multiple neutron scattering within the detector and therefore strongly depends on the size of the detector, neutron energy and detector threshold. The neutron time response is asymmetric in shape increasing with length and volume of the scintillator and with decreasing neutron energy [Kle06].

2.3 4π Neutron Multiplicity Detector

Apart from the neutron energy distribution, the total number of neutrons emitted in an event (neutron multiplicity) also plays a crucial role in determining the reaction mechanism, particularly in the Fermi energy domain. However, neutron measurement using time of flight technique is not generally quite efficient to estimate the neutron multiplicity very accurately on event by event basis. This is due to the fact that, the energy measurement using TOF technique is done by modular detectors, which are kept at a certain distance from the source position to achieve reasonable energy resolution. Therefore it suffers due to lack of efficiency. The efficiency may be improved by using large number of detectors; however, very close pack geometry is prohibited due to cross talk effect. So the other alternative and rather economical solution is to use a single, large volume detector which should be highly efficient in neutron detection. This may be achieved by a large volume liquid scintillator detector, where the scintillator is loaded with elements (Gd, Cd, B) having high (n, γ) capture cross-section. To ensure efficient neutron detection, the liquid scintillator is required to be loaded with typically 0.1 - 1.5% of Gd by weight [Lig04]. These detectors are used to count, in 4π geometry, the total number of neutrons emitted from the transient reaction product. Gd and B loaded scintillators based neutron multiplicity detectors are widely used in

accelerator based experiments for the measurement of neutron multiplicity with high efficiency [Jah03, Lie98, Sch95, Tak93, Cho93, Jah83].

2.3.1 Working principle

Neutron detection in a Gd loaded scintillator is based on the following steps; when a fast neutron enters the detector, it slows down in a few tens of nanoseconds primarily by multiple scattering with hydrogen nuclei in the scintillator and produces a prompt signal. After several collisions it is thermalized, provided it does not escape from the detector volume. The thermalised neutron then diffuses in the scintillator volume till it encounters a Gd nucleus. Gd has a very high neutron capture cross section (~10^5 barn) for thermal neutrons. When the neutron is captured in the Gd, it typically emits three gamma rays of total energy ~8 MeV. So, by detecting these capture gamma rays one can measure the total number of neutrons emitted. Thus the detection of neutrons by this method is a delayed process having two stages; thermalization and then diffusion of the neutron in the liquid until it is captured in the Gd nuclei. As the diffusion process is stochastic in nature, the time elapsed between the first interaction of a neutron with the liquid and its subsequent capture will have a distribution in time. This distribution of time interval is called the capture time distribution. Capture time distribution may be fine tuned by changing the Gd concentration; so it is essential to measure the capture time distribution to check its suitability for any particular experimental purpose. Usually, the capture time distribution is measured using a large volume of liquid [Jah03, Lie98, Sch95]. We have devised a new technique to measure capture time distribution using a small volume detector in combination with other ancillary (BaF_2) detectors, which is described below.

2.3.2 Measurement of Capture Time Distribution with small volume detector (proto-type): a new approach

The capture time distribution can be approximated with a two parameter exponential formula [Jah83]

$$P(t) = exp(-\lambda t)[t(\beta - \lambda) - 1] + exp(-\beta t), \tag{2.7}$$

where the parameter λ characterizes the moderation properties of the scintillator and is proportional to the proton density in the liquid; whereas β describes the capture strength of the scintillator and is proportional to the density of the Gd-nuclei. According to Eq. 2.7, the capture time distribution first builds up to reach a maximum and then falls off exponentially. The mean lifetime of neutron is given by

$$< t >= \beta^{-1} + 2\lambda^{-1} \tag{2.8}$$

Considering the capture part only [Jas04], Eq. 2.7 can be further simplified as,

$$P(t) = exp(-\beta t) \tag{2.9}$$

The parameter β can be estimated as follows; $\beta = [N_{Gd}\sigma v]$, $< t >= \beta^{-1}$, Where N_{Gd} is equal to the number density of Gd nuclei and σ is thermal neutron capture cross section in Gd, which follows a $1/v$ dependence, v being the neutron velocity. When a neutron is captured in Gd nucleus, it emits three γ-rays of total energy ~8 MeV on the average. In a large volume detector (e.g. 500 litre or more), these γ-rays are absorbed in the detector by multiple Compton scattering and produce a scintillation signal corresponding to the capture. But in a small cell these γ-rays are not fully absorbed. So it is not possible to detect any clean signal corresponding to the neutron capture event. However, the scattered γ-rays which come out of the detector cell may, if detected, be

utilised to generate the capture signal. This is what has been done in the present studies. We have specifically developed two stainless steel cylindrical (60 cm long, 13 cm diameter) cells for this measurements. The cells were filled with xylene based BC521 and mineral oil based BC525 liquid scintillators respectively and having different Gd loading. The scintillator cells were coupled with 5", 14 stage photomultiplier (PMT) tubes (9823B of Electron Tubes Ltd.). Two walls of BaF_2 detectors, one each on the two sides of the cylindrical detector cell, have been used to detect the scattered γ rays from the cell. The high γ efficiency and fast timing properties of BaF_2 detector have been utilised here. Each wall consisted of 5 BaF_2 detectors. The BaF_2 detectors were 35 cm long, square faced (3.5 cm $\times$ 3.5cm), and were coupled with photonics XP2978 photo tubes. Four BaF_2 detectors (of the same dimension as above) were used for the generation of a start signal and a ^{252}Cf source was positioned above the start detectors. Lead sheets of 3 mm thickness were put in between the source and the neutron detector to stop the γ-rays directly coming from the source. The layout of the experimental setup is shown schematically in Fig. 2.19. The start signal was generated from the liquid scintillator (prompt flash) in coincidence with an OR of the four BaF_2 detectors positioned on the top. This ensures a genuine neutron start. The stop signal was generated from the liquid scintillator detector in coincidence with an OR output of the 10 BaF_2 detectors forming the two walls surrounding the liquid scintillator detector. The scheme (Fig. 2.20) has been very effective in removing the background originating from the cosmic response of the detector. The measured capture time distributions of neutrons in BC521 and BC525 are shown in Fig. 2.21(left). The distributions show well developed peak at about 10 μs followed by a tail stretching over a time interval up to 40-70 μs.

The shape of the experimental distribution with a pronounced maximum is indicative of proper functioning of the detector. It is further seen that the higher the

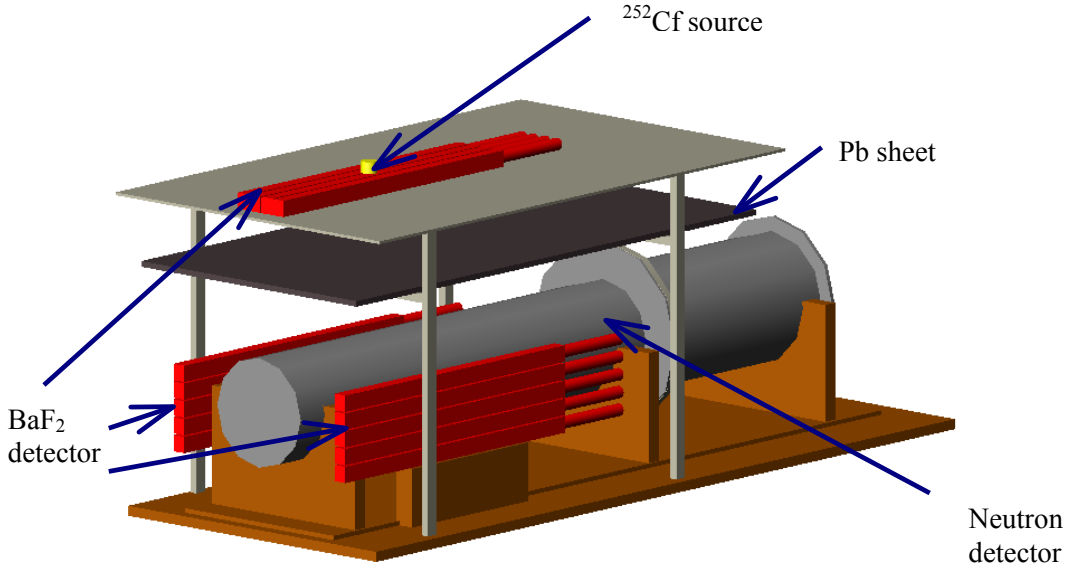

Figure 2.19: *Experimental setup for capture time distribution measurement.*

Gd concentration, the narrower the width of the distribution; nearly all neutrons have been captured in 35 μs in BC521 (0.5% Gd) and in 70 μs in BC525 (0.2% Gd). Experimental results have been compared with theoretical simulations of the capture time distribution using a Monte Carlo simulation code DENIS [Poi74]. The details of the simulation have been discussed in the following section. The simulation results have been shown in Fig. 2.21(right). It is seen that the experimental and the simulation results are in good agreement with each other. Mean capture times have been extracted from experimental data (Fig. 2.21-left side) as well as from the simulation results (Fig. 2.21-right side) and compared with that obtained from Eq. 2.8. The comparision of mean capture times has been given in Table. 2.4.

It is evident from the Table. 2.4 that both experimental and simulation results are in fair agreement with those predicted by theory (see Eq. 2.8). In order to have further insight on the effect of neutron moderation on capture time distribution, capture time distribution has been further simulated with thermal neutrons as source, so that

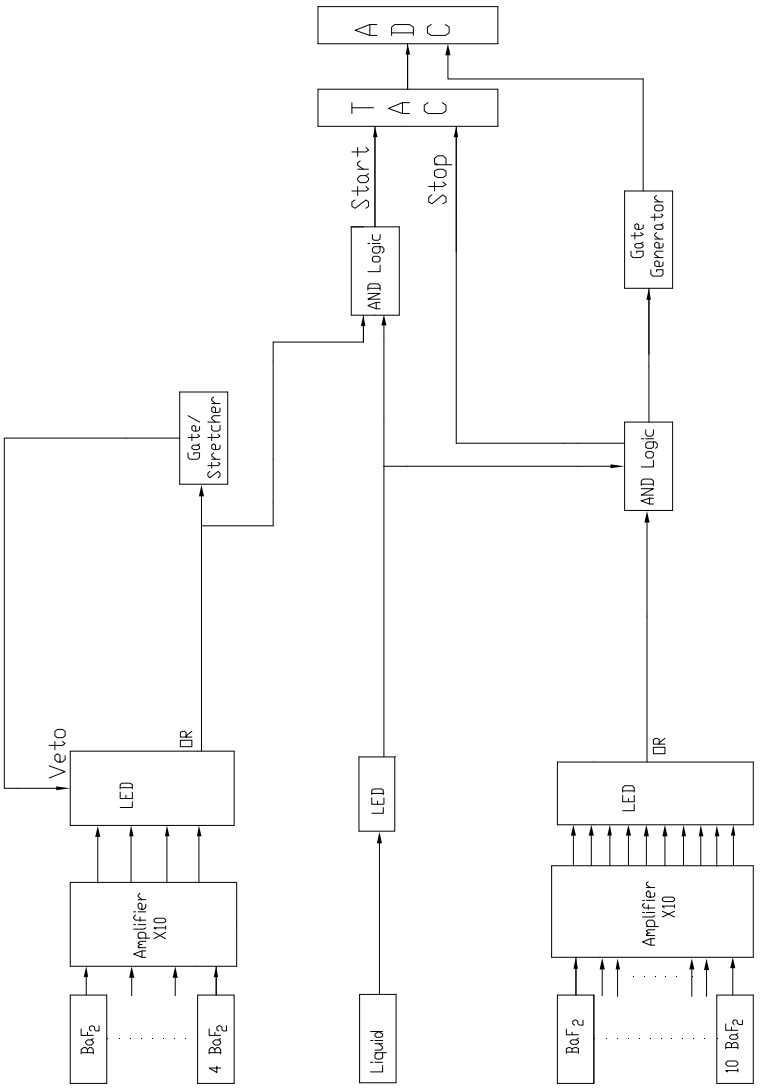

Figure 2.20: *Block Diagram of the Electronics for capture time distribution measurement.*

Table 2.4: *The calculated mean neutron capture time distribution.*

Scintillator	Gd(%)	$< t >$ (μs) Experiment	$< t >$ (μs) Simulation	$< t >$ (μs) Theory
BC521	0.5%	12.5±5	8.81	8.82
BC525	0.2%	17.3±7.7	18.67	22.3

they are captured directly by Gd present in the liquid scintillator. The distributions are shown in Fig. 2.22. It is clearly seen that the distribution is in agreement with Eq. 2.9. Comparing the two capture time distributions (with and without the inclusion of neu-

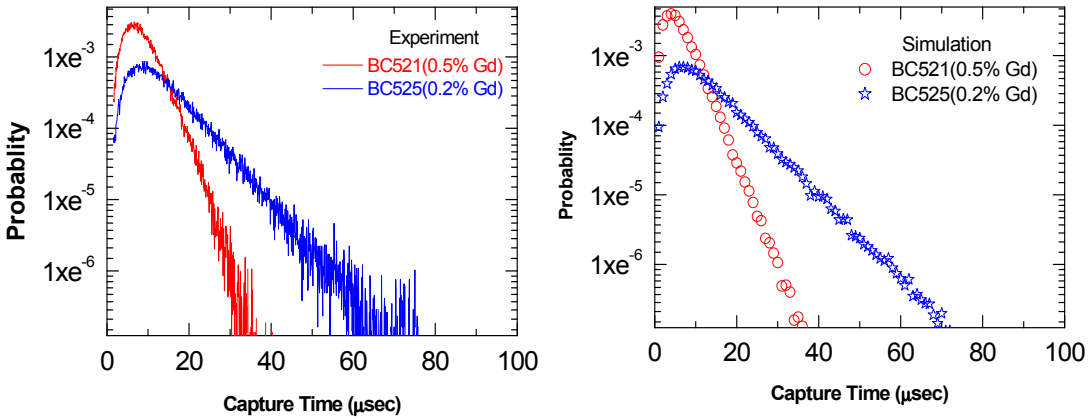

Figure 2.21: *Capture Time Distribution measured using ^{252}Cf source. Left hand side shows the Experimental result and right hand side shows the DENIS simulation.*

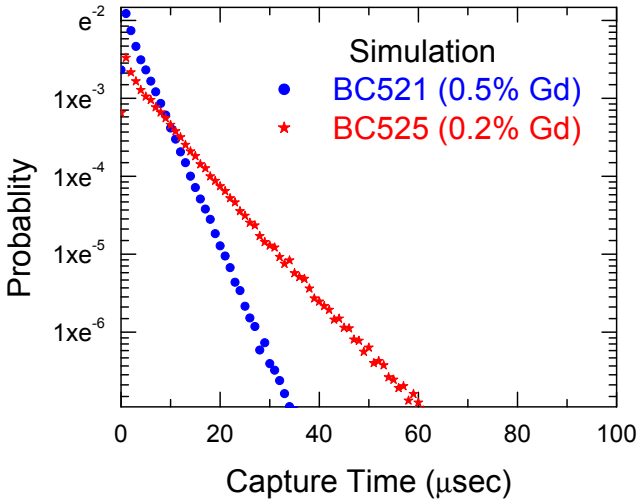

Figure 2.22: *DENIS simulation of Capture Time Distribution for thermal neutrons.*

tron moderation) in Fig. 2.21 and Fig. 2.22, it is obvious that the initial build up of the capture time distribution is primarily due to the finite moderation time of the energetic neutrons.

2.3.3 Design and simulation of 4π Neutron Multiplicity Detector

The simulation of neutron multiplicity detector (NMD) has been performed using the Monte Carlo code DENIS [Poi74]. The simulation process can be categorised in three stages. In the first stage, the energetic neutrons loose their kinetic energies by successive elastic (and inelastic) collisions in the scintillator. Once the neutrons are thermalised, they are captured in Gd which is doped in the liquid scintillator. In the next stage, several γ-rays $\sim$ (8MeV total) are emitted from the n, γ capture reaction; these γ-rays then interact via Compton scattering with the scintillator and produce scintillation. Finally the scintillation light is collected by the photomultiplier tubes, which is however neglected in our simulation. The full collisional history of each neutron from its first interaction in the scintillator to its subsequent slowing down and absorption is recorded on event by event basis. The initial direction of the neutrons (from the centre of the detector) are chosen randomly. A single neutron is followed until it is captured in the Gd nuclei or the time limit is exceeded (in our case 100 μs) or the neutron escapes from the detector. The slowing down of the neutron was followed till its energy was reduced to 25 meV (below this energy, neutron is thermalised). Six types of interactions have been taken into account; elastic scattering from ^{12}C, ^{1}H and ^{155,157}Gd nuclei, inelastic scattering from ^{12}C nucleus, and capture by ^{1}H and ^{155,157}Gd nuclei. Only spherical detector geometry has been considered for the simulation and maximum neutron energy considered is 10 MeV. It was observed that a spherical detector of 100 cm diameter and inner through hole for beam pipe of diameter 6.5 cm is optimum for neutron energy of $\sim$ 0.5 - 10 MeV. Capture site, capture time and efficiency of the detector has been studied in the simulation. Capture site is the co-ordinate of the detector where the neutron is captured in the Gd. The capture site distributions are shown in Fig. 2.23. The inner circle in the XZ plot shows the space left for the beam pipe (along Y axis), where as the outer circle shows the detector boundary. For

1 MeV neutrons, the capture sites are in the vicinity of the inner circle, whereas for 10 MeV neutrons the captures sites are spread all over the detector volume. This indicates the high efficiency of the detector for 1 MeV neutrons which decreases at 10 MeV. The simulated detection efficiency as function of neutron energy is shown in Fig. 2.24. Typically, the value of total neutron detection efficiency is 90% for 1 MeV neutrons, which decreases to 60% for 10 MeV neutrons.

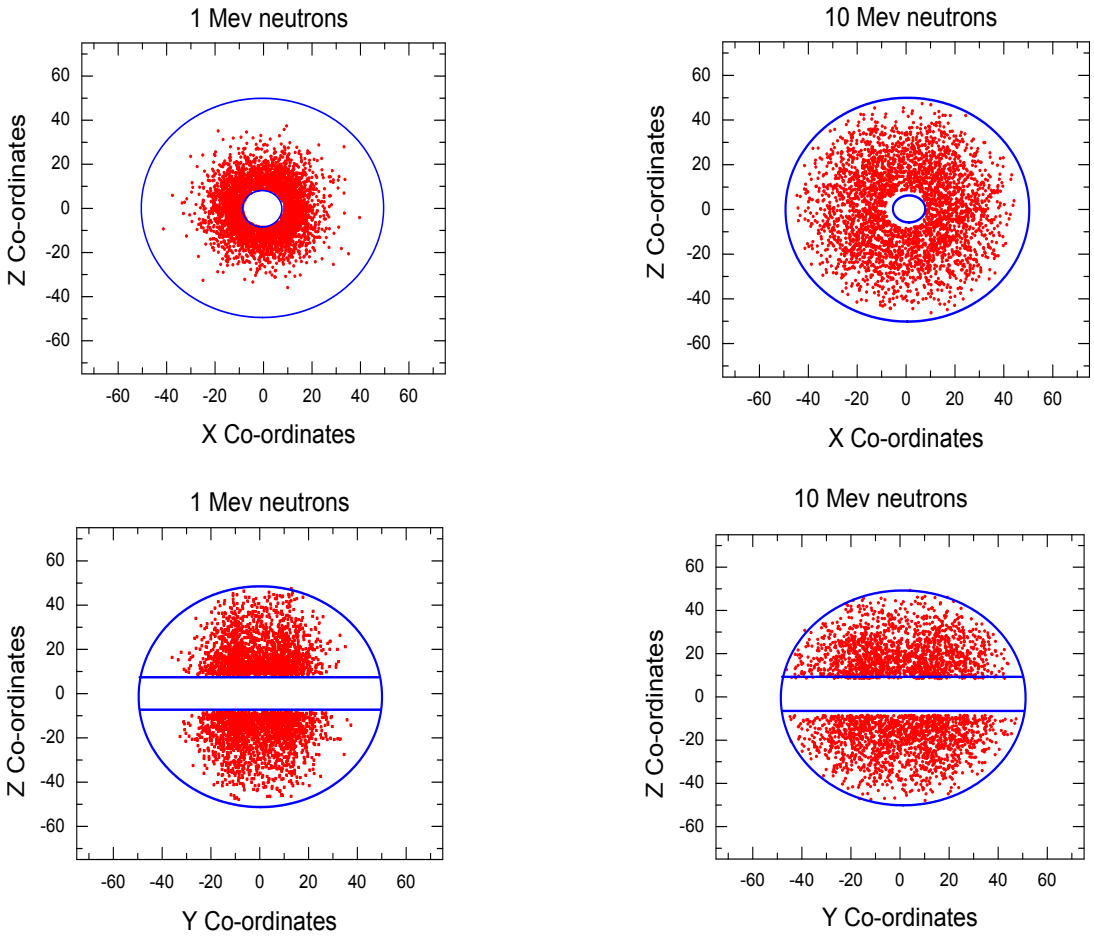

Figure 2.23: *Capture site distributions for 1 MeV and 10 MeV neutrons in different two dimensional planes.*

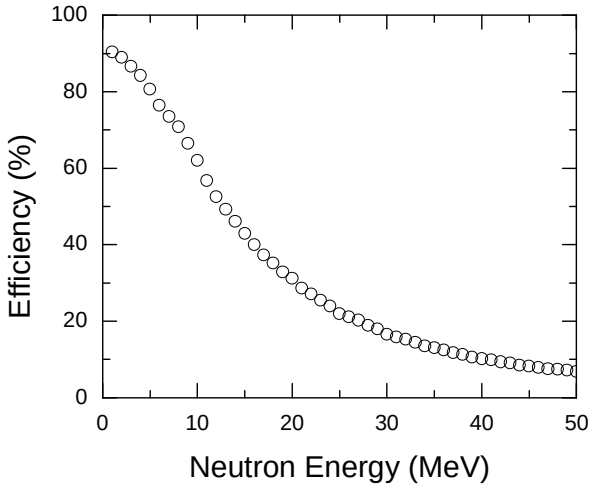

Figure 2.24: *DENIS calculation for detection efficiency as a function of neutron energy.*

2.3.4 Fabrication of 4π Neutron Multiplicity Detector

Based on the above simulation study, the NMD design has been finalised and fabrication has been done. The NMD consists of two stainless steel hemispheres of one metre diameter, filled with 500 litres of 0.5% Gd loaded liquid scintillator BC521. The hemispheres have been fabricated from a 8 mm thick stainless steel sheet using hot press method. Finally these were machined to get a uniform thickness of 5 mm. The hemishpheres are mounted on a mild steel movable trolley with adjustable jack. For scintillator light output readout, each hemisphere is fitted with five photo multiplier tubes (PMT) (model: 9823B; Electron tube Ltd) each of 5$''$ diameter, and, 10 mm thick pyrex glass windows are used at the interface of the scintillator and the PMT. Fig. 2.25 shows the PMT positions over the NMD. To take care of the thermal expansion of the liquid scintillator, each hemisphere is connected with an expansion chamber of capacity 25 litres. Each expansion chamber is connected with a pressure gauge and a pressure release valve. The completed 4π NMD is shown in Fig. 2.26.

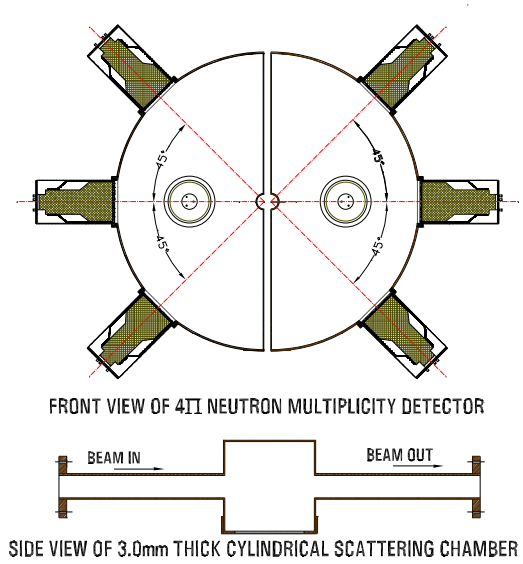

Figure 2.25: *Schematic diagram of 4π neutron multiplicity detector and inside vacuum chamber.*

Figure 2.26: *Neutron Multiplicity Detector and inside vacuum chamber.*

For emergency draining of liquid scintillator, each hemisphere is connected with stainless steel diapharm valve with a locking plug (model:6L- LD8 -BBXX;

Swagelok). This development involved many shopistocated anciliary system developments like, pumping system for liquid scintillator transfer, scintillator testing setup and readout electronics etc. Liquid filling was done by air operated double diapharm pump (make SANDPIPER) with teflon diapharm. All piping and valves are made up of teflon and stainless steel to avoid any possible contamination and subsequent degradation of liquid scintillator during filling.

2.3.5 Testing of 4π Neutron Multiplicity Detector

The detector has been tested with ^{252}Cf source, which was housed within the small scattering chamber kept in the centre of NMD (see Fig. 2.25, 2.26). A 40 μm silicon surface barrier detector was placed within the scattering chamber to detect the spontaneous fission fragments which are used to generate the 'MASTER GATE' for neutron counting. The threshold of the silicon detector were set in such a way, that it was sensitive for fission fragments only (insensitive for α particles of ^{252}Cf source). The silicon detector signal was delayed by 700 nsec to avoid the occurrence of prompt pulse of the NMD within the MASTER GATE. The circuit diagram for neutron multiplicity counting is shown in Fig. 2.27. All photomultiplier tubes were connected to CAMAC constant fraction discrimination (CFD, CAEN C808). The current sum of all CFDs of each hemisphere were connected to a leading edge discriminator (LED) with a preset threshold, which decides the number of PMT's fired simultaneously. For the present measurement we allowed LED output, when at least three PMTs fired simultaneously per hemisphere. Finally, the two logic pulses A, B were counted within a master gate of 50μ sec on event by event basis in a customized GATED CAMAC SCALER developed by Data Acquisition & Development Section at VECC. This module generates Look-At-Me (LAM) at the trailing edge of each event. The LAM initiates reading out of the neutron multiplicity count as one of the parameters in the list mode. The counter

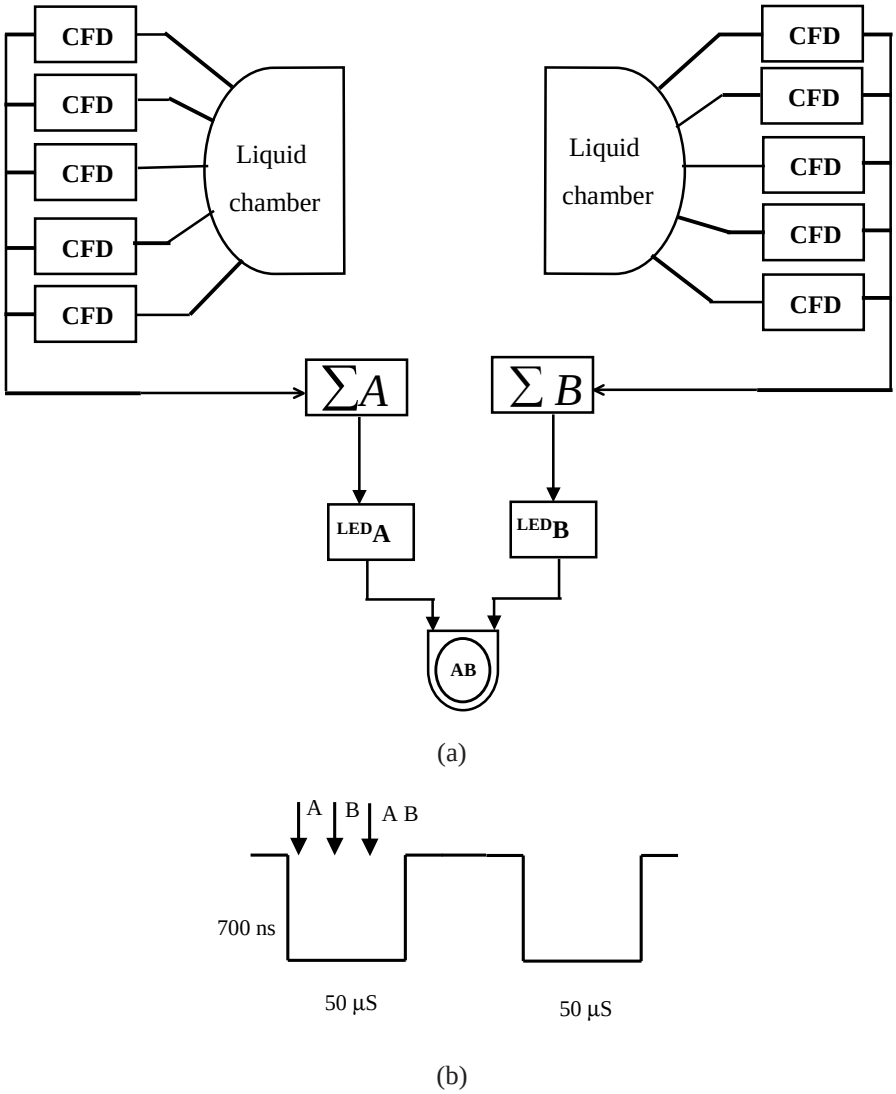

Figure 2.27: *(a) Circuit diagram of neutron multiplicity counting, (b) Timing diagram.*

is cleared after each readout. The random partial effective GATE width resulted due to the statistical occurrence of event asynchronous with respect to the module 'CLEAR' is eliminated with customized logic. The cross talk between two hemispheres were accounted by counting the coincidence GATE A+B within the same MASTER GATE. So the total neutron multiplicity N_{tot} may be defined as

$$N_{tot} = N(A) + N(B) - N(A + B) \tag{2.10}$$

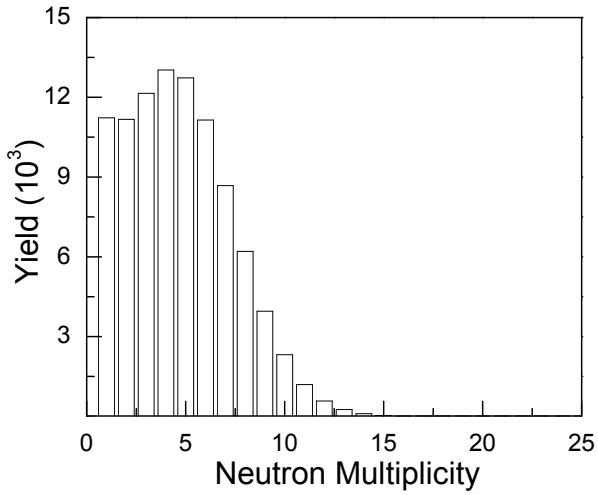

(a)

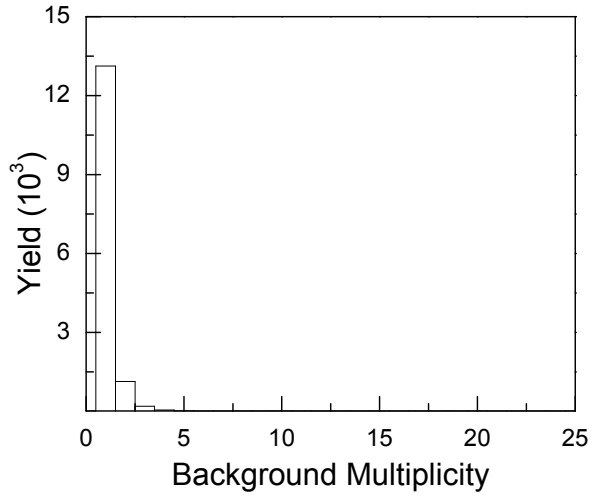

(b)

Figure 2.28: *(a) Neutron multiplicity for ^{252}Cf, (b) background multiplicity of NMD.*

Here $N(A)$ is the number of neutron detected in hemisphere A, $N(B)$ numbers of neutron detected in hemisphere B and $N(A + B)$ is the number of neutron which are detected in both the segment. Measured neutron multiplicity for ^{252}Cf is shown in Fig. 2.28- (a). Average neutron multiplicity observed in the present measurement is 4, which is consistent with the earlier reported value [Sch95]. Fig. 2.28- (b), shows the background multiplicity of NMD.

Chapter 3

Study of fission dynamics at near-barrier energies

3.1 Introduction

The present chapter deals with the fission dynamics study in ^{16}O + ^{238}U system. The motivation of the present study has already been discussed in chapter 1, which is based on the two earlier measurements. The angular distribution measurement by *Hinde et. al.* [Hin95] confirm the presnsence of quasi-fission transition at sub-barrier energies. On the contrary, the evaporation residues (ER) measurement indicates pre-equilibrium fission process [Nis04]. The distinction between quasi-fission and pre-equilibrium fission is, however, quite subtle. In pre-equilibrium fission, fusion and compound nucleus formation occur inside the true fission saddle point and thus fission takes place after the equilibration of all degrees of freedom except the K degree of freedom. Pre-equilibrium fission process usually occurs if the fission barrier height is comparable to the temperature and fission width becomes sufficiently large so that fission may take place before the system attains K-equilibration, leading to larger fragment angular anisotropy. However, as the mass equilibration is faster than the shape equilibration, mass equilibrated fragments may be re-separated as symmetric fission

fragments in a pre-equilibrium fission reaction, before the system reaches spherical compound nuclear shape due to thermal diffusion. The effect of K non-equilibration diminishes with the decrease of temperature, so it is unexpected, following the pre-equilibrium fission model [Ram85] that angular anisotropy or fission mass width would increase with decreasing energies in ^{16}O + ^{238}U system. On the contrary, in the case of quasi-fission, as the fission saddle point is more compact than the entrance channel contact configuration, the dinucleus, initially trapped in the conditional saddle point, evolves ultimately to re-separate before reaching mass symmetry. So, the study of fragment mass asymmetry in conjunction with other available probes will be crucial to decipher the difference between the two processes. Here under this thesis work, we have measured fragment mass distribution and neutron multiplicity for ^{16}O + ^{238}U system at near barrier and sub-barrier energies. The effectiveness of mass distribution studies in elucidating the intricacies of the fusion-fission reaction mechanism has already been established [Gho09]. Furthermore, prescission neutron multiplicity is also considered to be a useful probe for the study of fission dynamics. As the time scales of quasi-fission (~saddle to scission time) and fusion-fission (~presaddle time + saddle to scission time) are different, the appearance of quasi-fission at near barrier energies should be reflected in pre-scission neutron multiplicity data also. Such change (decrease) in pre-scission neutron multiplicity with the onset of quasi-fission has been observed [Don99]. The present measurements are, thus, complimentary to the measurements done earlier for this system using different probes [Hin95, Nis04] and it is expected to throw a new light on a long standing controversy.

3.2 Experimental Details

The experiment was performed using pulsed beam (using RF buncher with repetation rate 250 ns) of ^{16}O obtained from 15UD Pelletron of the Inter University Acceler-

ator Centre (IUAC), New Delhi. The targets used were ^{238}U of thickness 150 $\mu g/cm^2$ on 70 $\mu g/cm^2$ ^{12}C backing and self-supporting 400 $\mu g/cm^2$ ^{197}Au. The measurement on ^{16}O + ^{238}U, which is a spherical projectile, deformed target (β_2 = 0.215) [Mol95] system, have been carried out at E_{lab} = 83, 85, 87, 89, 92, 96 and 100 MeV. Measurements have also been carried out on ^{16}O + ^{197}Au system at 10 MeV above the Coulomb barrier for testing and calibration of the experimental setup and analysis procedures. Since the ground state deformation of ^{197}Au (β_2 = -0.131) [Mol95] is much less than that of ^{238}U and the experiment has been performed well above the Coulomb barrier, so only compound nuclear fission is expected in this system. For the detection of fission fragments, two large area (20 cm $\times$ 6 cm) position sensitive multi wire proportional counters (MWPC) [Gho05b] were placed at the folding angle for symmetric fission [Vio85], at distances of 26 cm and 41 cm respectively, from the centre of the target on either sides of the beam axis. Angular coverage of two MWPCs were 42° and 26° respectively. The details of MWPC has already been discussed in chapter 2. The position informations were derived from the X and Y sense wire planes with delay line read out. The end to end delay in X and Y positions are 200 ns and 150 ns respectively. The X sense wire plane consisted of 100 wires at a pitch of 2 mm and 30 wires at 2 mm pitch was used as Y sense wires. The position signals were read by tapped delay lines. The delay between successive X-sense wires was 2 ns, while that between Y-sense wires was 5 ns. Beam flux monitoring as well as normalization were done using the elastic events collected by two silicon surface barrier detectors placed at ±10°.

Four liquid scintillator (BC501A) based neutron detectors [Ban09], each of dimension 5" $\times$ 5", were used for the detection of neutrons. The neutron detectors were placed outside the scattering chamber at angles 30°, 60°, 90°, 120° with respect to the beam direction at a distance of 100 cm from the target. 3 mm thin stainless steel flanges were used in the ports of the scattering chamber facing the neutron detectors to min-

imise neutron scattering. The neutron detection thresholds were kept at 100 keVee by calibrating the detectors with standard gamma source. To keep the background of the neutron detectors at minimum level, the beam dump was kept at 3 meter away from the target and was well shielded with layers of lead and borated paraffins. Neutron energies were measured using Time of Flight (TOF) technique whereas the neutron gamma discrimination was achieved by pulse shape discrimination (PSD) and time of flight. The details of the experimental setup are shown in Figs. 3.1, 3.2 and 3.3 respectively.

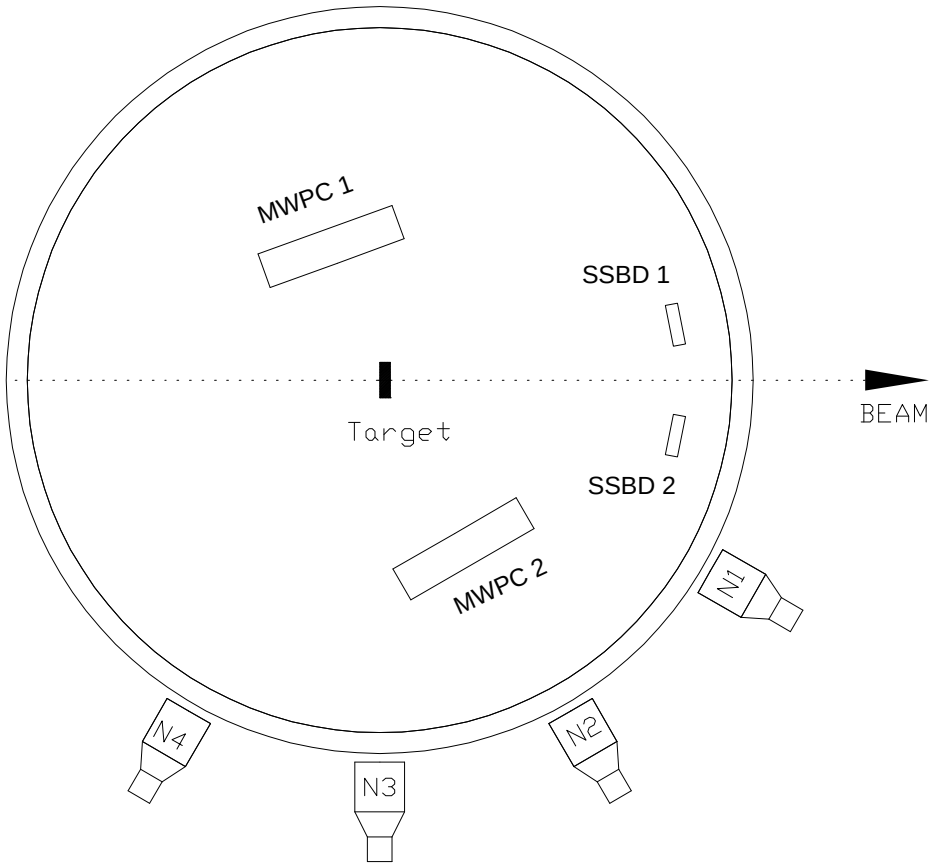

Figure 3.1: *Schematic of experimental setup*

.

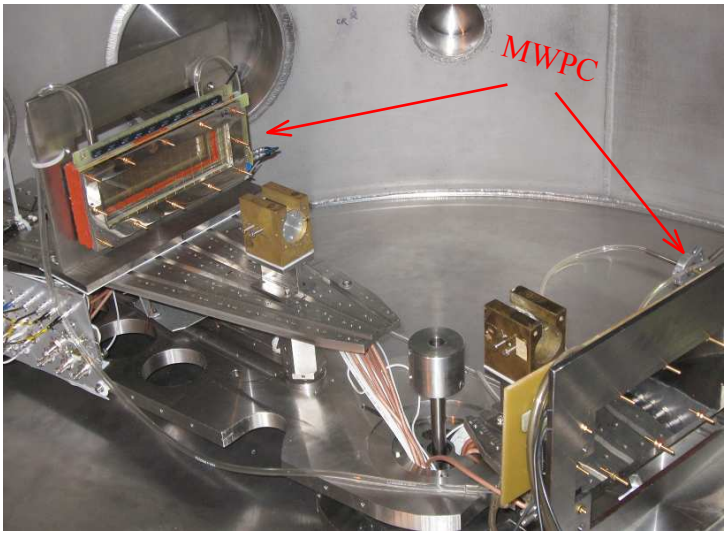

Figure 3.2: *Photograph of experimental setup, inside the vacuum reaction chamber.*

Figure 3.3: *Photograph of experimental setup, outside the vacuum reaction chamber.*

3.2.1 Electronics setup

The block diagram of the electronics setup is shown in Fig. 3.4. The anode signals from the two MWPCs were taken through fast timing pre-amplifiers (ORTEC VT 120A), and then fed to constant fraction discriminators (CFD, ORTEC 935). The data taking was triggered when any one of the two MWPCs ($A1$ or $A2$) fired in coinci-

dence with the RF. This logic output was used as the common start of the CAMAC 16 channel time to digital converter (TDC, Phillips Scientific 7186). Another channel of coincidence unit was used as master strobe for CAMAC 16 channel peak sensing ADC (Phillipse Scientific 7164). The fission TOF was obtained by using the delayed CFD outputs of the individual MWPC anode signals (A1 and A2), which were connected to the stop of the TDC. The delays were adjusted suitably for all logic signals so that they were within the TDC range after the common start. The position signals from the two detectors (x_1, y_1, x_2, y_2) were taken through Phillips Scientific 6955B pick off amplifiers and then fed to the CFDs, the outputs of which were connected to the stop channel of TDC after suitable delay adjustment. The energy loss signals (ΔE_1, ΔE_2) from the MWPCs were taken through charge sensitive pre amplifiers (ORTEC 142IH). The shaping and amplification of energy loss signals were done using ORTEC 572 spectroscopic amplifiers and then they were connected to the ADC. The energy signals from the silicon surface barrier detectors (SSBD) were also processed in the similar way (not shown in figure).

The anode pulses of the neutron detectors were fed to dual channel PSD module, developed by IUAC, New Delhi [Ven08]. This module provides simultaneously the pulse height (PH), CFD and the zero cross over (ZCO) outputs. CFD outputs of the neutron detectors were connected to the TDC to get neutron time of flight information. The PH and ZCO were connected to the ADC to get the pulse height and the pulse shape informations. The discrimination between the neutron and the γ- rays was achieved by using ZCO and TOF outputs.

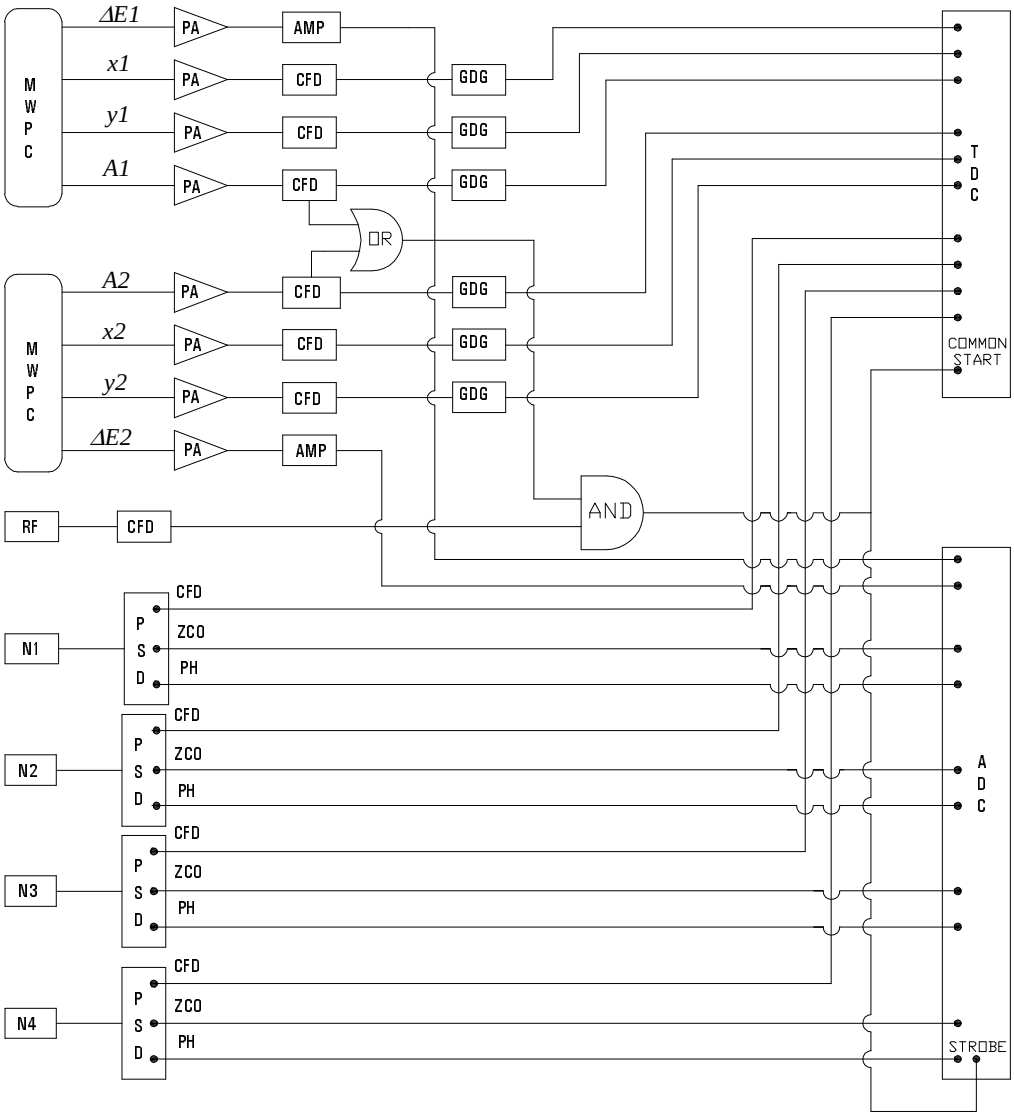

Figure 3.4: *Block diagram of electronic circuit.*

3.3 Data Analysis

The data were collected on event by event basis; each event consists of information on the time of flights (t_1, t_2), positions (x_1, y_1, x_2, y_2) and energy losses (ΔE_1, ΔE_2) of the fission fragments in MWPCs, as well as time of flights (t_n), pulse heights and zero cross overs for neutrons. MWPC provide the position signal of a fission fragment by

measuring the delay of the sense wire pulse with respect to the anode pulse. Since the position resolutions obtainable in these detectors are excellent in terms of angular resolution, position calibrations are usually done using the shadows of the window support wires [Gho05a]. A typical x spectrum is shown in Fig. 3.5, where the dips in x spectrum are the shadows of the MWPC window support wires. There were 14 wires (4 wires) provided as the support to the window foil of the MWPC along x- axis (y-axis). The correlation between the length of the MWPC along x -direction ℓ and the offset angle $\Delta\theta$ of the wire position from the central position of the detector is tabulated in Table. 3.1. Fig. 3.6 shows the correlation plot between length ℓ and $\Delta\theta$ of MWPC. The correlation for polar angle $\Delta\theta$ (azimuthal angle $\Delta\phi$) can be written as

$$\Delta\theta = a_0 + a_1 l \qquad\qquad \Delta\phi = b_0 + b_1 h \tag{3.1}$$

Here h is the length of the MWPC along y -direction and a_0, a_1, b_0, b_1 are the calibration coefficients. The fission fragment position information was then converted to the angle of the corresponding fragment as explained in Fig. 3.7. The MWPC dimension is 20 cm $\times$ 6 cm, so the central position of the detector was assigned as ℓ = 0 cm in x -direction while the right edge and the left edge of the detector were ℓ = - 10 cm and ℓ = + 10 cm, respectively. The position signal was taken from the right edge of the detector. 10 delay line chips, each with 20 ns delay were used in the x -sense wire plane. So the delay tx_i (i =1,2) at the right edge of the detector was 0 ns while at the left edge was 200 ns.

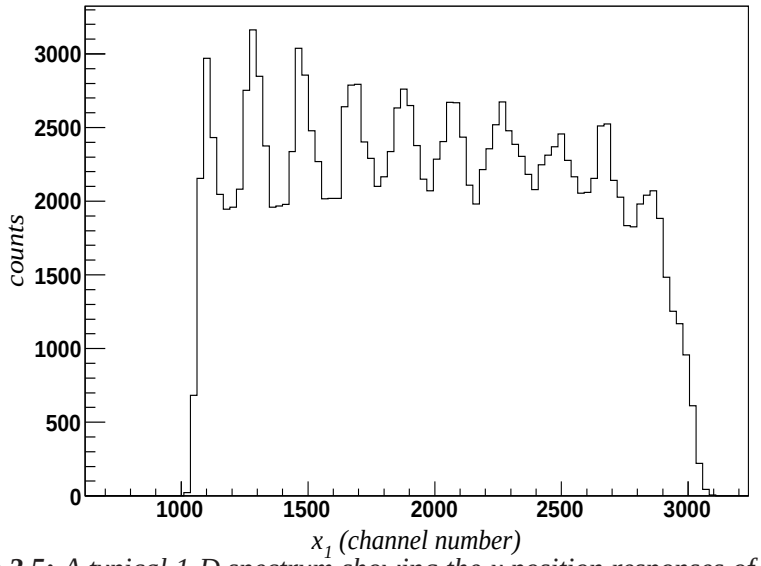

Figure 3.5: *A typical 1-D spectrum showing the x position responses of the MWPC1.*

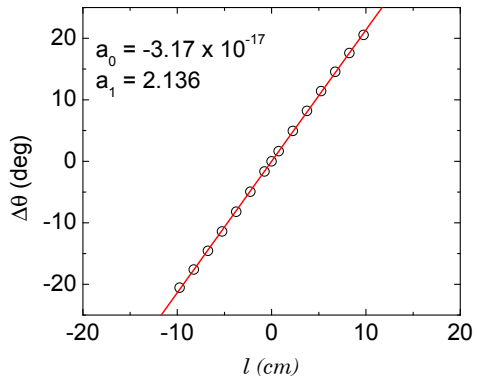

Figure 3.6: *Correlation plot between the detector length and off-set angle of the window support wire from the central position of the detector.*

Position	Length (cm)	$\Delta\theta$
Wire 1	-9.75	-20.55°
Wire 2	-8.25	-17.6°
Wire 3	-6.75	-14.55°
Wire 4	-5.25	-11.41°
Wire 5	-3.75	-8.20°
Wire 6	-2.25	-4.94°
Wire 7	-0.75	-1.65°
Centre	0.0	0.0°
Wire 8	0.75	1.65°
Wire 9	2.25	4.94°
Wire 10	3.75	8.20°
Wire 11	5.25	11.41°
Wire 12	6.75	14.55°
Wire 13	8.25	17.6°
Wire 14	9.75	20.55°

Table 3.1: *The angular off-sets of the window support wires and the length of MWPC1.*

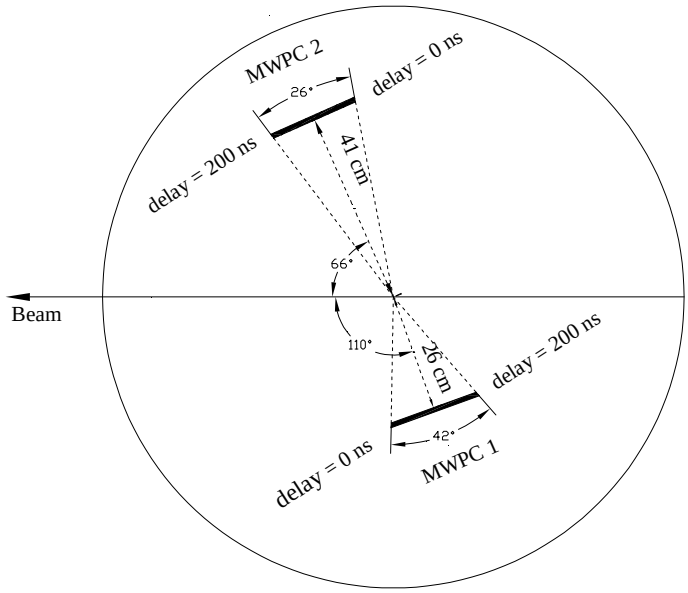

Figure 3.7: *Schematic diagram of angular calibration.*

Similarly the delay in *y*- direction was 150 ns, so the corresponding delay ty_i (i =1,2) at the top and bottom edge of the detector were 0 ns and 150 ns respectively. Thus the relation between the length ℓ (h) and delay tx_i (ty_i) for MWPC can be defined as follows,

$$l_i = \frac{tx_i - 100}{10} \qquad\qquad h_i = \frac{ty_i - 75}{25} \tag{3.2}$$

Therefore the polar angular offset $\Delta\theta$ (azimuthal angular offset $\Delta\phi$) can be found from the time delay by the relation

$$\Delta\theta_i = a_i + a_i'\left[\frac{tx_i - 100}{10}\right] \qquad\qquad \Delta\phi_i = b_i + b_i'\left[\frac{ty_i - 75}{25}\right] \tag{3.3}$$

The value of tx_i (ty_i) from the channel number x_i (y_i) of any x- spectrum (y- spectrum) can be derived from the time difference between initial channel and x_i (y_i) channel.

$$tx_i = tx_i' - tx_i^{in} \qquad\qquad ty_i = ty_i' - ty_i^{in} \tag{3.4}$$

tx_i' (ty_i') and tx_i^{in} (ty_i^{in}) are calculated from channel number x_{ich} (y_{ich}) of the spectrum using TDC calibration. The values of tx_i' (ty_i') and tx_i^{in} (ty_i^{in}) are given by

$$tx_i' = C_i + C_i' x_{ich} \qquad ty_i' = D_i + D_i' y_{ich} \tag{3.5}$$

$$tx_i^{in} = C_i + C_i' x_{ich}^{in} \qquad ty_i^{in} = D_i + D_i' y_{ich}^{in} \tag{3.6}$$

Here C_i, C_i', D_i and D_i' are the calibration coefficients. The actual angular position is estimated by adding $\Delta\theta$ ($\Delta\phi$) with θ (ϕ) are shown below.

$$\theta_1 = \theta_1 + \Delta\theta_1 \qquad \phi_1 = 90^\circ - \Delta\phi_1 \tag{3.7}$$

$$\theta_2 = \theta_2 - \Delta\theta_2 \qquad \phi_2 = 90^\circ + \Delta\phi_2 \tag{3.8}$$

3.3.1 Fission Fragment Folding Angle Distribution

The angle between the two fission fragments in lab frame is called the folding angle. The folding angle depends on the velocity of the fission fragments ($\vec{v_1}$ and $\vec{v_2}$) and the recoil velocity ($\vec{v_r}$) of fissioning nucleus as shown in Fig. 3.8.

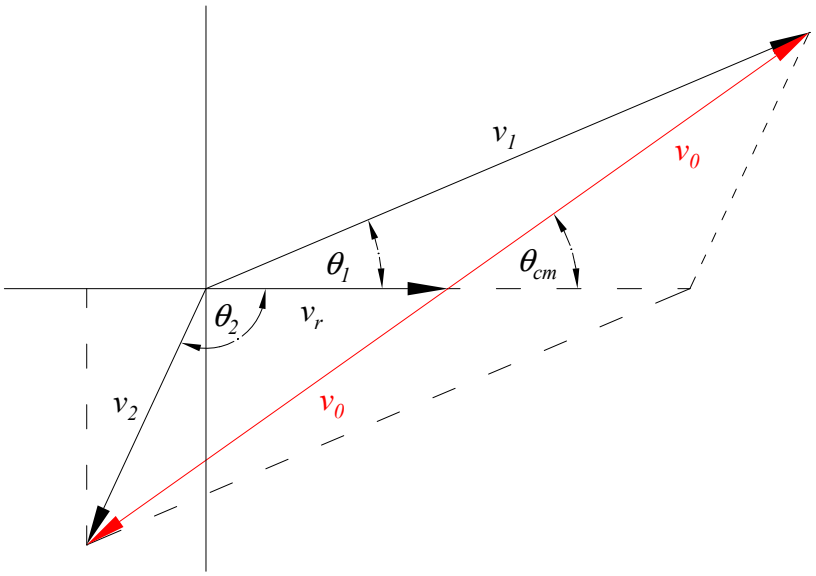

Figure 3.8: *Kinematics of fission following the fusion.*

In the case of symmetric fission of the compound nucleus following full momentum transfer of the projectile to the fused fissioning system, $\vec{v_r} = \vec{v_{CM}}$, the compound nucleus velocity, and the centre of mass velocity for both the fragments is same ($\vec{v_\circ}$). The folding angle can be written as

$$\theta_{fold} = \theta_1 + \theta_2 \tag{3.9}$$

To calculate the folding angle theoretically at an angle, say θ_1, θ_2 must be evaluated in terms of known quantities. Considering the Fig. 3.8

$$tan\theta_2 = -tan(\pi - \theta_2) = \frac{-v_1 sin\theta_1}{v_1 cos\theta_1 - 2v_r} = \frac{v_1 sin\theta_1}{2v_r - v_1 cos\theta_1} \tag{3.10}$$

The folding angle for symmetric fission can be written as

$$\theta_{fold} = \theta_1 + tan^{-1}\left[\frac{v_1 sin\theta_1}{2v_r - v_1 cos\theta_1}\right] \tag{3.11}$$

The fission fragment centre of mass velocity can be written as

$$v_\circ^2 = v_1^2 + v_r^2 - 2v_1 v_r cos\theta_1 \tag{3.12}$$

Writing the above equation as a quadratic equation of v_1 and solving it we get

$$v_1 = \frac{1}{2}[2v_r cos\theta_1 \pm \sqrt{4v_r^2 cos^2\theta_1 + 4(v_\circ^2 - v_r^2)}] \tag{3.13}$$

Considering the positive root only, as for the negative root v_1 becomes negative with increasing θ_1. Therefore

$$v_1 = v_r cos\theta_1 + \sqrt{v_r^2 cos^2\theta_1 + (v_\circ^2 - v_r^2)} \tag{3.14}$$

The recoil velocity and recoil energy of the compound nucleus can be written as

$$v_r = \sqrt{\frac{2E_r}{A}}, \qquad and, \qquad E_r = \frac{p_i^2}{2A} \tag{3.15}$$

Where A is the mass of the compound nucleus, p_i is the momentum of the incident particle, which is equal to the momentum of the recoiling nucleus p_r (full momentum transfer). The fragment velocity in centre of mass frame can be calculated by using Viola systematics [Vio85], which is used for calculating the fragment total kinetic energy for symmetric fission as

$$v_\circ = 1.414\sqrt{\frac{TKE}{A}} \qquad TKE = \left[0.1189\frac{Z^2}{A^{1/3}} + 7.3\right] \tag{3.16}$$

where Z is the charge of the fissioning nucleus. The measured folding angle distribution is shown in Fig. 3.9, which is found to be Gaussian in shape.

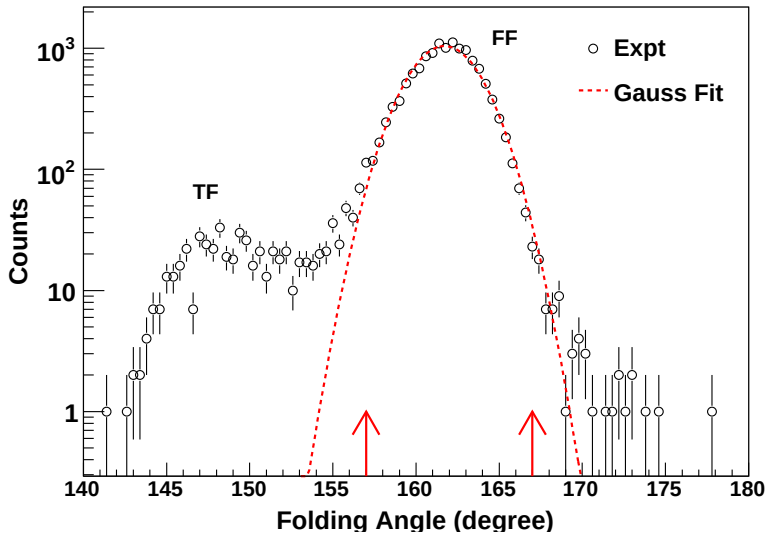

Figure 3.9: *Measured folding angle distribution of all fission fragments in the reaction* ^{16}O + ^{238}U *at* $E_{c.m.}$ *= 81.5 MeV. The two arrows indicate the gate used to select the FF events for mass determination.*

3.3.2 Velocity distribution of the Composite

The velocities of the fissioning system in the reaction plane and in the plane perpendicular to it can be used to separate the fusion-fission and transfer fission components. The velocity component of the fissioning system along the beam direction $v_{\|}$

was calculated from the polar folding angle (θ) and the velocities of two fragments. The velocity component of the fissioning system in the perpendicular direction $v_\perp$ is in the plane perpendicular to the beam and also perpendicular to the projection of the scission axis onto this plane. It was determined from the azimuthal folding angle (ϕ) and the projection of the measured fragment velocities onto this plane. In Fig. 3.10, the velocities of the fragments are denoted by v_1 and v_2, and the emission angles are θ_1 and θ_2, measured with respect to the beam direction.

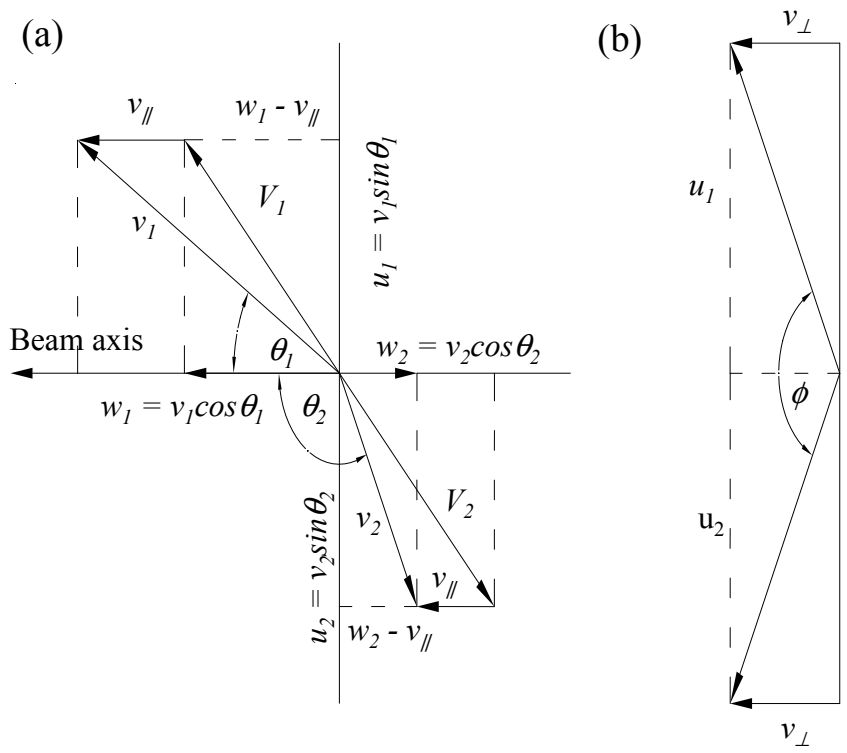

Figure 3.10: *Diagrams of the fission fragment velocity components. (a) Plane including the fission fragment velocity vectors and the beam axis (b) plane perpendicular to the beam.*

Initially it is considered that the two velocity vectors and the beam axis are co-planar (which is equivalent to neglecting $v_\perp$). In Fig. 3.10, the velocities of the fragments in the centre of mass frame are denoted by V_1 and V_2. The measured velocity vectors are decomposed into orthogonal components, parallel (denoted by w_1, w_2),

and, perpendicular (denoted by u_1, u_2) to the beam axis. The velocity components u_i and w_i define the reaction plane for compound nuclear reaction. For compound nuclear reaction $< v_\perp >$ is essentially zero, while a non-zero value of $v_\perp$ signifies a non-compound reaction. Thus a scatter plot of $v_\parallel$ versus $v_\perp$ clearly differentiates the compound and non-compound fission events. It is evident from the Fig. 3.10 that, $w_1 = v_1 cos\theta_1$, $w_2 = v_2 cos\theta_2$, $u_1 = v_1 sin\theta_1$ and $u_2 = v_2 sin\theta_2$. Neglecting the small effects of prescission particle evaporation, the two fragments are taken as co-linear and co planar in the centre of mass frame and the ratio

$$\frac{u_1}{u_2} = -\frac{w_1 - v_\parallel}{w_2 - v_\parallel} \tag{3.17}$$

can be defined. The minus sign is due to the fact that u values (unlike w) can only be positive. Thus, $v_\parallel$ is given in terms of the measured velocity components by

$$v_\parallel = \frac{u_1 w_2 + u_2 w_1}{u_1 + u_2} \tag{3.18}$$

For fission following complete absorption of the projectile by the target, the full momentum of the projectile is transferred and $v_\parallel$ should be equal to the calculated centre of mass velocity for the collision $v_{c.m.}$. However deviations from binary kinematics due to emission of light particle perturbs the fission fragment velocity, resulting in a significant spread in $v_\parallel$. The geometry in the plane perpendicular to the beam is shown in Fig. 3.10(b). The measured components u_1 and u_2 are related to the actual velocities of the fragments in the centre of mass frame of the fissioning system by an in-plane vector having two components. From the Fig. 3.10, we can write

$$\frac{v_\perp}{u_1} = cos\frac{\phi}{2} \tag{3.19}$$

$$\frac{\frac{1}{2}\sqrt{u_1^2 + u_2^2 - 2u_1 u_2 cos\phi}}{u_2} = sin\frac{\phi}{2} \tag{3.20}$$

The velocities of the fissioning system perpendicular to the scission axis can be written as

$$v_{\perp} = \frac{u_1 u_2 sin\phi}{\sqrt{u_1^2 + u_2^2 - 2u_1 u_2 cos\phi}} \tag{3.21}$$

For full momentum transfer fission only the light particle emission causes $v_{\perp}$ to deviate from zero which is very small. Fig. 3.11 shows a typical fragment velocity distribution for ^{16}O + ^{238}U system measured at $E_{c.m.}$ = 81.5 MeV. For fusion-fission process, the events were centered around the velocity coordinates (($v_{\parallel}$-v_{CN}), $v_{\perp}$) = (0, 0). The events corresponding to transfer fission are scattered around non zero ($v_{\parallel}$-v_{CN}), $v_{\perp}$ values.

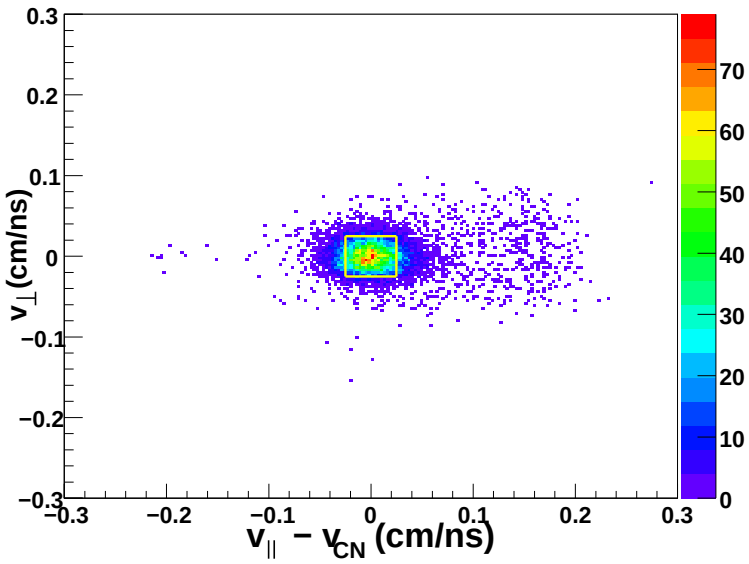

Figure 3.11: *Measured distribution of velocity of the fissioning nuclei at $E_{c.m.}$ = 81.5 MeV. The (yellow) rectangle indicates the gate used to select the FF events for mass determination.*

3.3.3 Separation of fusion-fission from transfer fission

Since at bombarding energy close to the coulomb barrier, Transfer Fission (TF) is a dominant reaction channel. So, in order to extract the contributions of fusion-fission

and quasi-fission (QF), both of which are full momentum transfer processes, TF contribution needs to be separated from the experimental data [Maj95]. The polar folding angle distribution of all fission events (fusion-fission and transfer fission) is shown in Fig. 3.9. Figure shows that the measured folding angle distribution of fusion fission events is peaked around 165°, consistent with the theoretical value for full momentum transfer events (FMT). The transfer fission events are peaked around a smaller folding angle as the ejectile moves in the backward direction. The fission fragments from full momentum transfer events (FF and QF) were exclusively selected from the correlation of the velocity of the fissioning system ($v_{\|}$) in the beam direction relative to the recoil of the fused system and the velocity perpendicular to the reaction plane ($v_{\perp}$) (Fig. 3.11), as well as the correlation of the polar and azimuthal angles of the fragment (θ, ϕ) with respect to the beam axis (Fig. 3.9).

3.3.4 Fission Fragment Mass Distribution

The masses of the fission fragments were determined from the polar angles θ, azimuthal angle ϕ and TOF information obtained from the experiment. Typical time correlation 2-D spectrum between the two MWPCs is shown in Fig. 3.12. It can be observed that events from elastic and quasi-elastic reactions were effectively eliminated and purely binary FFs were selected. Additional elimination of elastic and inelastic channels from fission fragments were obtained from the correlation of energy deposition signals (ΔE_1, ΔE_2) from cathodes of two MWPCs. Since the detectors are thin and operated at low pressure, the elastic and quasi-elastic channels have poor response and almost all (> 99 %) the events in the 2-D plot are from fission fragments. The kinematic diagram given in Fig. 3.13 elucidates the method of determination of masses of the fission fragments using TOF technique. If θ_1 and θ_2 are the polar angles with respect to

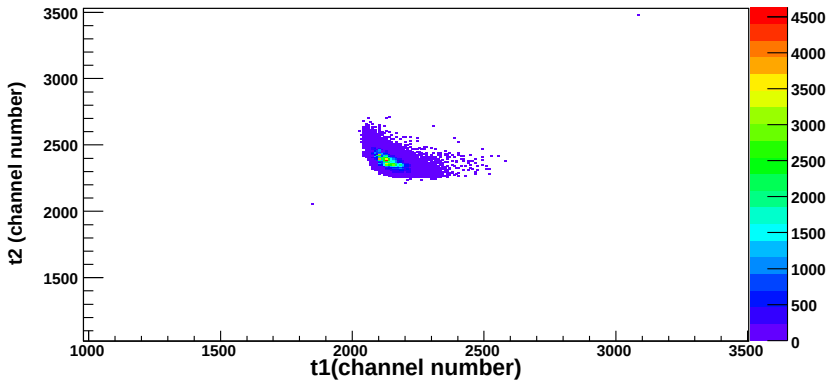

Figure 3.12: *Typical spectrum of timing correlation between anode signals of two MWPCs.*

the beam direction of the fragments of masses m_1 and m_2 respectively. Assuming full momentum transfer,

$$p_1 cos\theta_1 + p_2 cos\theta_2 = m_{CN} V_{CN} \tag{3.22}$$

$$p_1 sin\theta_1 = p_2 sin\theta_2 \tag{3.23}$$

Here m_{CN} is the mass of the compound nucleus moving with velocity V_{CN}. Assuming no particle emission before scission

$$m_{CN} = m_1 + m_2 \tag{3.24}$$

The flight time of the two fragments t_1 and t_2 over the distance d_1 and d_2 can be written as

$$t_1 = \frac{d_1}{v_1}; \qquad t_2 = \frac{d_2}{v_2} \qquad \Rightarrow t_1 - t_2 = \frac{d_1}{v_1} - \frac{d_2}{v_2} = \frac{d_1 m_1}{p_1} - \frac{d_2 m_2}{p_2} \tag{3.25}$$

$$\frac{d_1 m_1}{p_1} - \frac{d_2(m_{CN} - m_1)}{p_2} = m_1\Big(\frac{d_1}{p_1} + \frac{d_2}{p_2}\Big) - \frac{d_2 m_{CN}}{p_2} \tag{3.26}$$

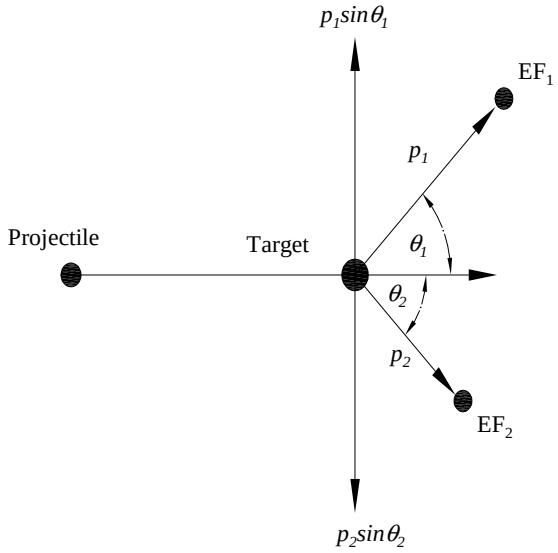

Figure 3.13: *Kinematic diagram of the fusion-fission process.*

$$m_1 = \frac{(t_2 - t_1) + m_{CN}\left(\frac{d_2}{p_2}\right)}{\frac{d_1}{p_1} + \frac{d_2}{p_2}} \tag{3.27}$$

The experimentally measured fission time of flight of the two fragments t_1 and t_2 are having additional delays (δt_1 and δt_2) due to electronics, cable and structure of pulsed beam. So t_1 and t_2 in the above equation should be replaced by $t_1 + \delta t_1$ and $t_2 + \delta t_2$. Therefore the above equation can be written as

$$m_1 = \frac{(t_1 - t_2) + \delta t + m_{CN}\left(\frac{d_2}{p_2}\right)}{\frac{d_1}{p_1} + \frac{d_2}{p_2}} \tag{3.28}$$

where $\delta t = \delta t_1 - \delta t_2$. The measured mass distribution of fission fragments, near and above the coulomb barrier energies, are shown in Fig. 3.14 for ^{16}O + ^{238}U and ^{16}O +

^{197}Au systems. It is observed that the measured mass distributions are well fitted with single Gaussian distribution at all energies.

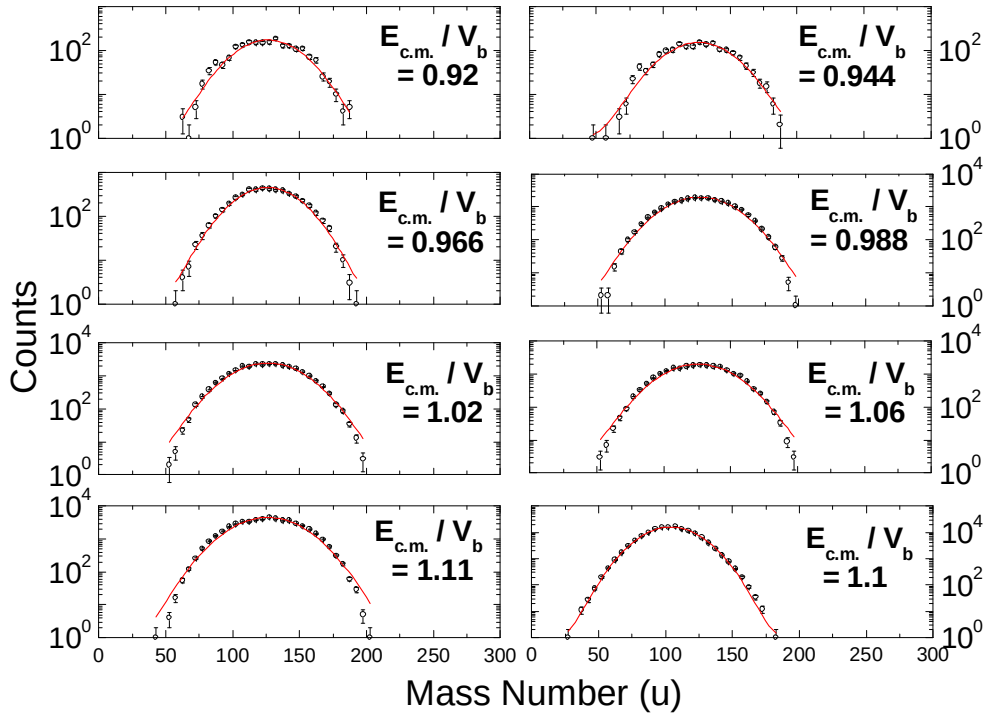

Figure 3.14: *Measured mass distributions for the reactions ^{16}O + ^{238}U, ^{16}O +^{197}Au (bottom, right) at energies near and above Coulomb barrier. The Gaussian fits are shown by (red) solid lines.*

The variation of the standard deviation (σ_m) of the fitted Gaussian as a function of $E_{c.m.}/V_b$, where $E_{c.m.}$ is the incident energy in centre of mass and V_b is the coulomb barrier, is shown in Fig. 3.15. At above barrier energy σ_m is found to increase with increase in $E_{c.m.}/V_b$. However, it is seen that, there is a sudden increase in σ_m as the energy decreases to below-barrier energy. Since the TF contribution has been removed as explained earlier, the increase in width of the mass distribution is a clear indication of a sudden qualitative change in the degree of mass equilibration in ^{16}O + ^{238}U system at below barrier energies.

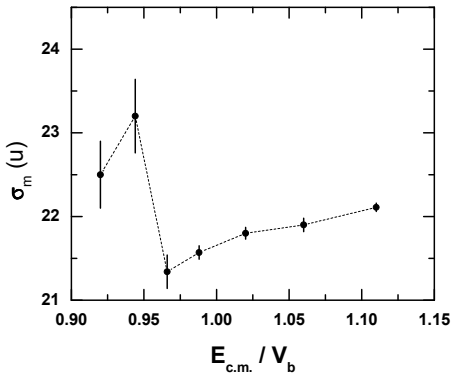

Figure 3.15: *Variation of the σ_m as a function of $E_{c.m}/V_b$, the dotted curve is for eye guide only.*

3.3.5 Neutron Multiplicity

A typical two dimensional spectrum of neutron time of flight versus zero cross over (ZCO) is shown in Fig. 3.16. The neutron TOF spectrum was extracted using a two dimensional gate as shown in Fig. 3.16.

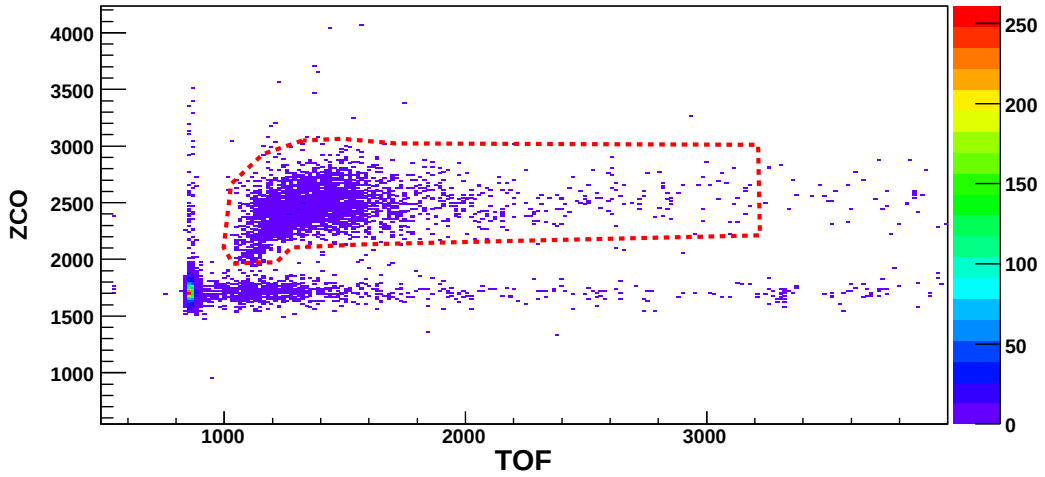

Figure 3.16: *TOF vs ZCO plot. The lower band is due to γ -rays and the upper band is due to the neutrons.*

Neutron energy is related to TOF by the following relation

$$E_n = \frac{1}{2} m_n \left(\frac{\ell}{t_n}\right)^2 \tag{3.29}$$

Where, m_n is the mass of the neutron, ℓ is the flight path, t_n is the neutron time of flight. Using prompt gamma peak as time reference, the measured TOF spectra were transformed into energy spectra using proper incorporation of Jacobian. During the course of transformation from the time domain to the energy domain, events (counts) must be conserved, i.e. the number of events, $N(t)$, in a time bin, δt, for a time domain spectrum must equal the number of events, $N(E)$, in the corresponding energy bin, δE, for the energy domain spectrum. Therefore the transformation can be written as follows,

$$N(E) \cdot \delta E = N(t) \cdot \delta t \tag{3.30}$$

$$N(E) = N(t) \cdot \left|\frac{\delta t}{\delta E}\right| = N(t) \cdot \frac{t}{2E} \tag{3.31}$$

The term $\left|\frac{\delta t}{\delta E}\right|$ is the Jacobian for time to energy transformation. The energy spectrum thus obtined was corrected for efficiency of the neutron detector, which was estimated using Monte Carlo Computer code NEFF [Die82].

The neutrons emitted in the fission-like decay of the compound nucleus have multiple origin; they are emitted either from the compound nucleus during its dynamical evolution to the scission point (pre-scission neutrons), or from the excited fission fragments (post-scission neutrons). In addition, neutrons may also be emitted in the fission process before full equilibration of all degrees of freedom is achieved (pre-compound neutrons). At near barrier energies, pre-scission and post scission emission processes are the most dominant sources of the neutron spectrum. The pre-scission and post-scission components of the neutron spectrum have been extracted from the experimen-

tal neutron energy distribution using phenomenological moving source model, where it is assumed that the neutrons are emitted from thermally equilibirated sources having different velocities and temperatures [Hil79]. Therefore in the rest frame of the source, the emitted neutrons are assumed to follow Maxwell Boltzmann kinetic energy distribution,

$$\frac{dn}{n} = \frac{2}{\sqrt{\pi}} \frac{1}{(K_B T)^{3/2}} \sqrt{E_{nf}} exp\left(\frac{-E_{nf}}{K_B T}\right) dE_{nf} \tag{3.32}$$

Where dn/n is the fraction of neutrons having kinetic energy between E_{nf} and E_{nf} + dE_{nf}, E_{nf} is the kinetic energy of neutrons in the source frame, T is the temperature of the emitter and K_B is the Boltzmann constant. So the neutron multiplicity (M_n) distribution may be written as

$$\frac{dM_n}{dE_n} = \frac{2M_n}{\sqrt{\pi}} \frac{1}{(K_B T)^{3/2}} \sqrt{E_{nf}} exp\left(\frac{-E_{nf}}{K_B T}\right) \tag{3.33}$$

From the Fig. 3.17 the velocity of the neutrons with respect to the neutron emitting source V_{nf} can be written as

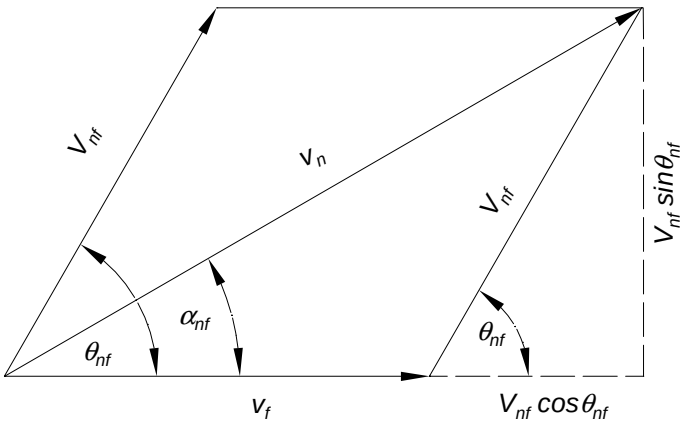

Figure 3.17: *Pictorial representation of neutron emission kinematics.*

.

$$V_{nf}^2 = v_n^2 - v_f^2 - 2v_f V_{nf} cos\theta_{nf} \tag{3.34}$$

Where θ_{nf} is the neutron emission angle in the source frame, v_f source velocity and v_n is the velocity of neutrons in the lab frame. From Fig. 3.17 we get

$$V_{nf}cos\theta_{nf} = v_n cos\alpha_{nf} - v_f \tag{3.35}$$

$$V_{nf}^2 = v_n^2 - v_f^2 - 2v_f(v_n cos\alpha_{nf} - v_f) \tag{3.36}$$

$$V_{nf}^2 = v_n^2 + v_f^2 - 2v_f v_n cos\alpha_{nf} \tag{3.37}$$

$$E_{nf} = E_n - 2\sqrt{\frac{E_n E_f}{m_f}}cos\alpha_{nf} + \frac{E_f}{m_f} \tag{3.38}$$

Where α_{nf} is the neutron detection angle in the lab frame, E_f is the kinetic energy of the neutron emitting source of mass m_f. Assuming $K_B = 1$ in Eq. 3.33, $\sqrt{E_{nf}} \approx \sqrt{E_n}$ and combining Eq. 3.33 with Eq. 3.38

$$\frac{dM_n}{dE_n} = \frac{2M_n\sqrt{E_n}}{\sqrt{\pi}T^{3/2}}exp\left(-\frac{E_n - 2\sqrt{\frac{E_n E_f}{m_f}}cos\alpha_{nf} + \frac{E_f}{m_f}}{T}\right) \tag{3.39}$$

Assuming that the neutrons are emitted from three moving sources (the prescission neutrons emitted from a compound nuclear source and the post-scission neutrons emitted from either of the two fully accelerated fission fragments), the total neutron multiplicity, M_n^{tot}, may be expressed as

$$\frac{d^2M_n^{tot}}{dE_n d\Omega} = \sum_{i=1}^{3}\frac{M_n^i\sqrt{E_n})}{2(\pi T_i)^{3/2}} \times \exp\left(-\frac{E_n - 2\sqrt{E_n E_i/m_i}\cos\alpha_i + E_i/m_i}{T_i}\right) \tag{3.40}$$

Here E_i, T_i, M_n^i, m_i are the energy, temperature, multiplicity and mass of i^{th} neutron emission source ($i = 1, 2, 3$ correspond to the pre-scission and two post-scission sources), respectively. α_i is the relative angle between the neutron direction and the i^{th}

source direction. The kinetic energies of the fission fragments were calculated from Viola systematics for symmetric fission (see Eq. 3.16) [Vio85]. Optimum source parameters have been extracted by fitting the data with the Eq. 3.40, through Chi-square minimization technique [Ros89]. In this analysis, TF events have been precisely removed by considering suitable gates as mentioned earlier. The post-scission multiplicity and the temperatures were assumed to be the same for both the post-fision fragments. The total neutron multiplicity, M_n^{tot}, has been estimated as $M_n^{tot} = M_n^{pre} + 2M_n^{post}$. Fig. 3.18 shows the fits to the experimental double dfferential neutron multiplicity spectra at various angles for ^{16}O + ^{238}U reactions at E_{lab} = 100 MeV.

The Fig. 3.18 clearly shows that at angles around 0° (or 165°), spectra are dominated by the post-scission component whereas the contribution of pre-scission component gradually becomes significant at higher angles (α_{nf} = 60°). Fig. 3.19 shows the experimental double dfferential neutron multiplicity spectra along with the respective fits for pre- scission and post-scission neutron contributions at differnet beam energies for ^{16}O + ^{238}U and ^{16}O + ^{197}Au systems. The pre-scission, post-scission and total neutron multiplicities per fission as function of $E_{c.m.}/V_b$, where V_b is the barrier energy, are shown in Fig. 3.20 alongwith the respective statistical model [Jil08] predictions. The experimental fusion cross sections were taken from [Nis04]. The value of friction coefficient β, for the present calculation was taken to be $10 \times 10^{-21} sec^{-1}$ for all excitation energies. The measured fission fragment mass distributions were used in the calculation to estimate the post-scission neutron emission. The calculated M_n^{pre} values are found to be in good agreement with the experimentally estimated values; the calculated M_n^{post} values are also found to be in fair agreement with the corresponding experimental estimates except at below-barrier energy (E_{lab} = 85 MeV).

This discrepancy at below-barrier energy, in particular, may be due to non inclusion of the shell correction in the fission barrier used in the present calculation;

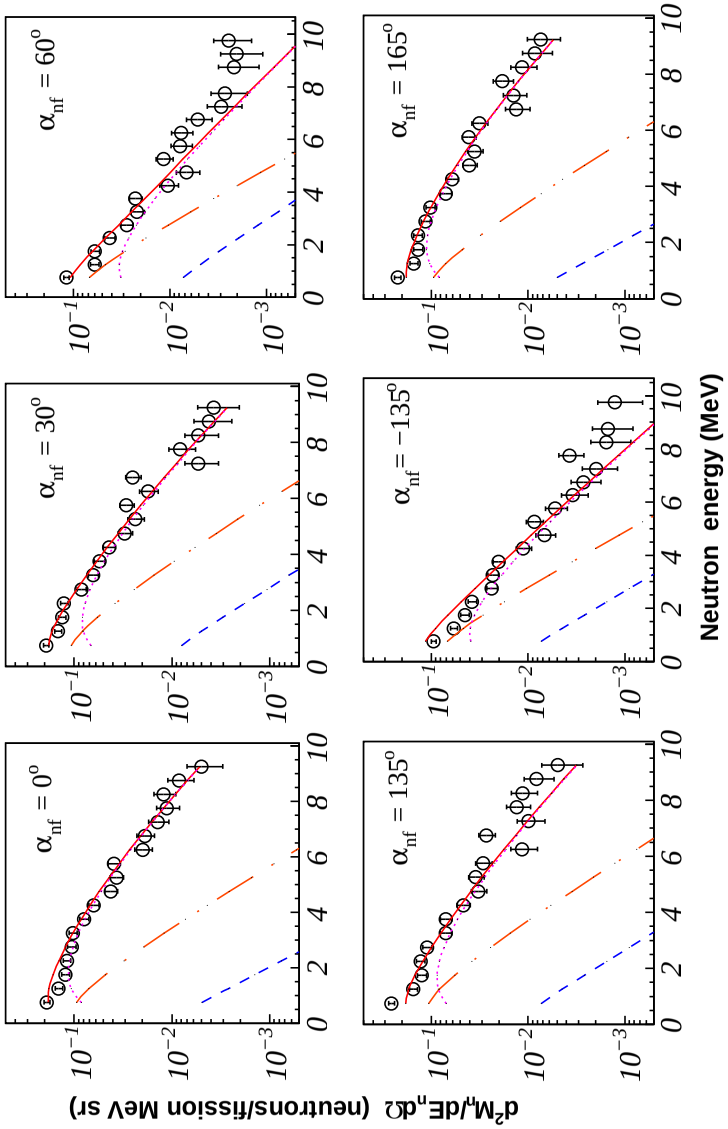

Figure 3.18: *Measured neutron multiplicity spectra (hollow circles) for the $^{16}O + ^{238}U$ reaction at E_{lab} = 100 MeV at different lab angles, along with the fits for the pre-scission (brown dot dash curve) and post-scission components from the two fission fragments (magenta dotted and blue dash curves). The solid curve (red) represents total contribution.*

inclusion of shell correction usually increases the fission barrier [Mol09] and thereby reduces the excitation energy of the fragments.

3.4 Results and Discussions

Assuming that the sudden change in the degree of mass equilibration (and vis-a-vis σ_m) is due to the onset of quasi-fission. It may be possible to extract the contribution of

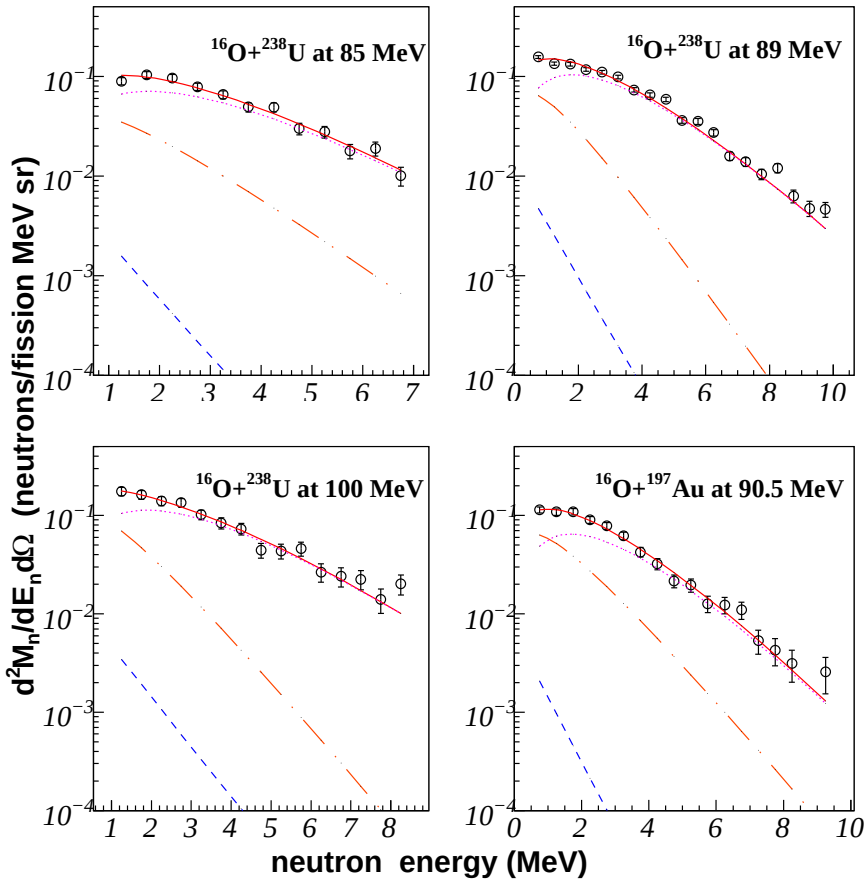

Figure 3.19: *Measured neutron multiplicity spectra (hollow circles) along with the fits for the pre-scission (brown dot dash curve) and post-scission components from the two fission fragments (magenta dotted and blue dash curves). The solid curve (red) represents total contribution.*

.

quasi-fission in the total fission process in the following way. At above barrier energies, the variances of mass distribution are only due to fusion-fission and they follow the relation $\sigma_m^2 = (\sigma_m^2)^{FF} \propto T$, where $T = \sqrt{E^*/a}$ is the nuclear temperature, E^* is the excitation energy at scission point, a = $A_{CN}/10$ is the level density parameter, A_{CN} is the compound nucleus mass number. The value of $(\sigma_m^2)^{FF}$ at below barrier energies are then extracted by extrapolating the σ_m^2 values at above barrier energies to lower energies using linear curve fitting (see Fig. 3.21). The percentage of QF was estimated

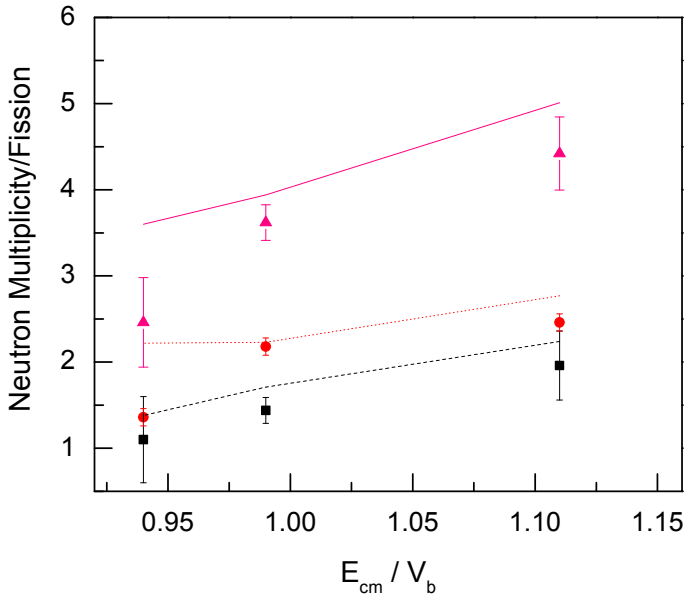

Figure 3.20: *Comparison of experimental M_n^{pre} (square, black), M_n^{post} (circle, red) and M_n^{total} (triangle, pink) with respective theoretical estimates (black dotted, red dashed, solid pink curves) at different energies.*

.

by comparing the areas under the Gaussians having variances σ_m^{FF+QF} and $(\sigma_m)^{FF}$. Gaussian fit consider total contribution FF + QF (blue dash line) and considering only FF (red line) contribution of measured mass distribution data in ^{16}O + ^{238}U system are shown in Fig. 3.22. It is found that QF contribution at two below barrier energies are ~ 6 % (at 85 MeV) and ~ 5 % (at 83 MeV).

It is interesting to note that the present mass distribution result clearly shows a sharp change in the mass distribution width, which is a signature of sudden qualitative change in the degree of mass equilibration; this may be considered to be a strong evidence for the onset of quasi-fission in ^{16}O + ^{238}U system at below-barrier energies. This is thus reaffirming the observation made earlier on the onset of quasi-fission at below-barrier energies for the same system from the study of fission fragment angular anisotropy measurement [Hin95]. On the contrary, present measurement of prescission neutron multiplicity for the same system at above and below barrier energies

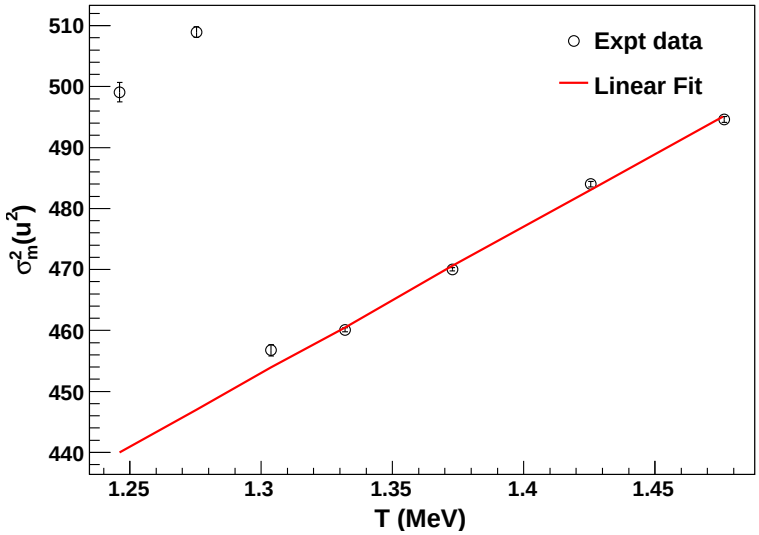

Figure 3.21: *Variation of the $\sigma_m^2(u^2)$ with T (MeV), along with linear fit to the data (red solid line).*

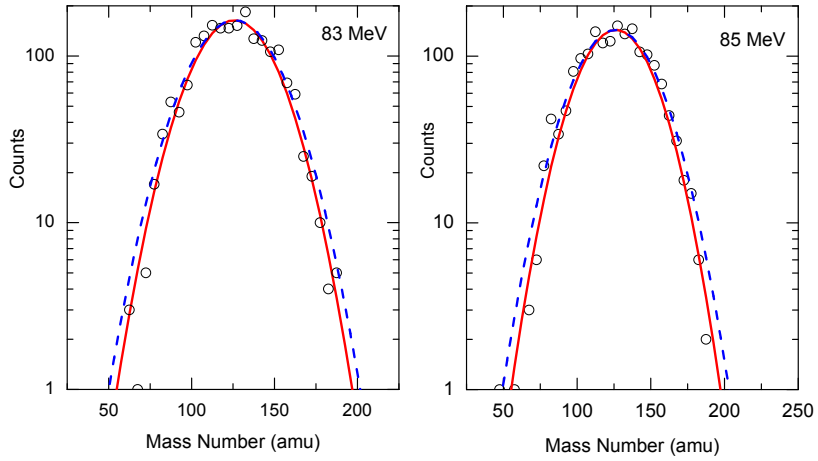

Figure 3.22: *Measured mass distribution of ^{16}O + ^{238}U (black hollow circles) along with the Gaussian fit consider total contribution FF + QF (blue dash line) and considering only FF contribution (red solid line).*

is clearly consistent with the standard statistical model [Jil08] prediction; this apparently indicates that quasi-fission does not significantly modify the complete fusion yield (and vis-a-vis M_n^{pre}) for this system even at below barrier energies. Similar inference was drawn from the study of ER measurements for the same system [Nis04],

where, too, no departure from the statistical model prediction was seen, and it was concluded that the anomalous fragment anisotropy might be linked to preequilibrium fission, not quasi-fission.

The apparent inconsistency in the inferences being drawn about the onset of QF from four different probes (fragment angular anisotropy and fragment mass distribution width on one hand, and, evaporation residue cross section and pre-scission neutron multiplicity on the other hand) warrants some discussion at this point. As two different probes (the fragment angular anisotropy and the fragment mass distribution width) have shown clear signatures of a transition to QF for this system at below barrier energies, we can conclude that quasi-fission transition is "confirmed" for ^{16}O + ^{238}U system at below barrier energies. Though the fragment angular anisotropy may be common to both pre-equilibrium fission and quasi-fission, the present observation of the change in fragment mass width, which is linked with the non-equilibration of mass asymmetry degree of freedom, is confirming the onset of quasi-fission. Moreover, as the temperature of the system, as extracted from the present neutron data, is $\sim$ 1 MeV and the shell corrected barrier is 6.24 MeV [Mol09], pre-equilibrium fission may be less dominant than expected at these energies [Ram85]. In addition, as the value of (Z_{proj}·Z_{target}) is very low (736) for this system, fusion hindrance due to Coulomb factor (extra push) may not be significant; so it may be inferred that the origin of quasi-fission in ^{16}O + ^{238}U system at below barrier energies is primarily due to orientation of the deformed target projectile system.

That the other two probes (ER and pre-scission neutron multiplicity) did not show unambiguous signatures of quasi-fission transition for this system in particular may be intuitively understood in the following way. The ER measurement is more sensitive for more symmetric systems (Z_{proj}·$Z_{target} \gtrsim 1500 - 1600$), for which quasi-fission fraction is comparable or even larger than fusion-fission. This has been established in a re-

cent study of ER measurement for ^{34}S + ^{238}U system at near barrier energies [Nis10], where significant reduction in ER formation was observed. On the contrary, in the case of highly asymmetric ^{16}O + ^{238}U (Z_{proj}·Z_{target} = 736) system, the present experimental estimate of quasi-fission ($\sim$ 5 – 6%) is much smaller than the fusion-fission cross section. The present experimental estimates are also close to the geometrical estimate ($\sim$ 13%) of the orientation dependent quasi-fission (tip collision) [Nis04] for the same system. Hence the change in ER cross-section may not be appreciable to be detected unambiguously. Same argument holds for pre-scission neutron multiplicity as well. For the present system, which is highly asymmetric, no departure of M_n^{pre} from statistical model prediction was observed, which indicate absence of quasi-fission. However for more symmetric system (^{58,64}Ni + ^{208}Pb) such change in M_n^{pre} indicating quasi-fission has already been reported in the literature [Don99].

Chapter 4

Neutron Evaporation study in ^{119}Sb

4.1 Introduction

The motivation of the present experiment is to extract nuclear level density parameter and study its dependence on angular momentum using fusion evaporation reaction. ^{119}Sb was chosen for the present study, which is near the shell closure and having ground state deformation β_2 = -0.122 [Mol95]. The neighboring nuclei which may produce after neutron evaporation are ^{118}Sb, ^{117}Sb, ^{116}Sb and their corresponding β_2 values are -0.138, -0.122, -0.122 respectively. The collective enhancement of NLD due to this deformation, if any, is expected to be damped with the increase in excitation energy at $T_c \sim 1$ MeV (see Eq. 1.21). In the present work, we measured the γ-ray multiplicity gated neutron energy spectra in the decay of ^{119}Sb* in the excitation energy range of $\sim$ 31-43 MeV, which corresponds to the average temperature in the range of $\sim$1.0 - 1.4 MeV. Light ion induced reaction (^{4}He + ^{115}In) has been chosen in the present study to populate the compound nucleus ^{119}Sb*, as it has some specific advantages over the heavy ion fusion route of production which is evident from Fig. 4.1.

It is seen from the figure that, in the case of light ion induced reaction, there is only one major residue ^{116}Sb (yield > 77%) produced via 3n channel at E^* = 42.9

MeV; on the other hand, a similar compound nucleus (^{115}Sb*) at similar excitation energy produced through heavy ion fusion route, will lead to two prominent residues ^{112}Sn (yield ~ 48.1%) and ^{112}Sb (yield ~ 28.9%), produced via *p*2*n* and 3*n* channels, respectively (lower part). So, the level density extracted through neutron spectra in the later case is not that of a particular nucleus; rather, it is averaged over more than one nuclei (residues). At lower excitaion energy (E^* = 31.3 MeV) light ion induced reaction is even more favourable as a single residue ^{117}Sb populated with yield > 90% via 2*n* channel.

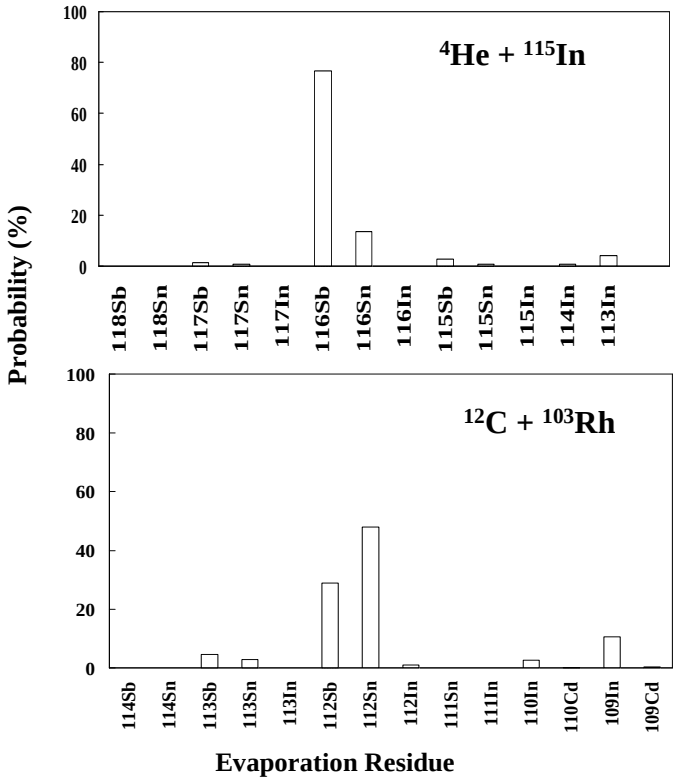

Figure 4.1: *Statistical model calculation of the relative yields of various evaporation residues produced in two different entrance channels at E* = 42.9 MeV.*

4.2 Experimental Details

The experiment was carried out using ^{4}He ion beam at bombarding energies of 30 and 42 MeV from K130 cyclotron at VECC. Self supporting ^{115}In (99%) target of thickness 1 mg/cm^2 was used. Four liquid Scintillator (BC501A) detectors (typical dimensions $\sim 5'' \times 5''$ and $7'' \times 5''$) [Ban09] were used to detect the neutrons produced in this reaction in coincidence with a 50 element BaF_2 based low energy γ multiplicity filter array [Dee10] to estimate the populated angular momentum on event-by-event basis. The filter array was split into two blocks of 25 detectors each and were placed on the top and the bottom of a thin wall reaction chamber (wall thickness ~ 3 mm) in a staggered castle type geometry. The multiplicity filter was kept at a distance of 5 cm from the target position and the solid angle coverage was ~56%. Schematic of experimental setup is shown in Fig. 4.2. Fig. 4.3 shows the actual photograph of the setup.

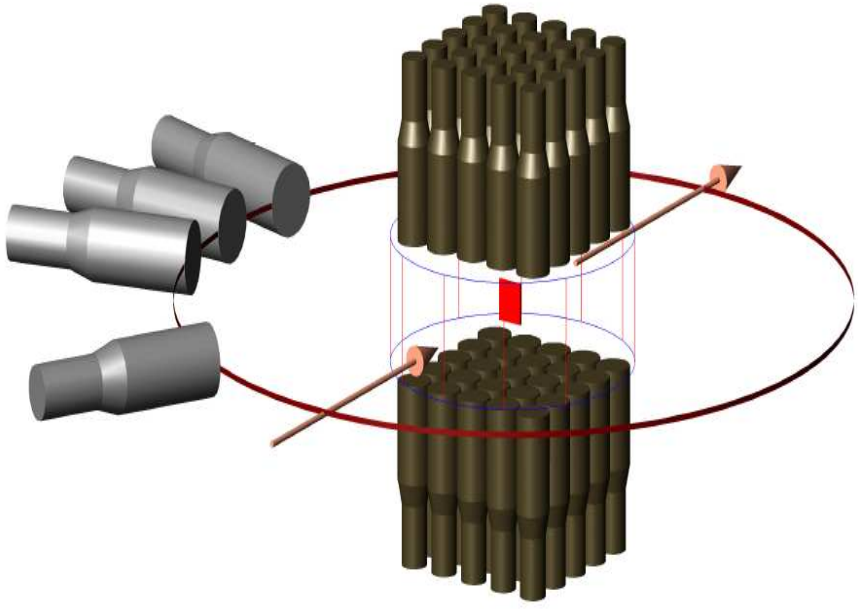

Figure 4.2: *Schematic of ^{4}He + ^{115}In experiment setup, arrow shows the beam direction.*

Figure 4.3: *Picture showing the setup of ^{4}He + ^{115}In experiment.*

The neutron detectors were placed outside the scattering chamber at angles 75°, 90°, 105° and 150° with respect to the beam direction at a distance of 150 cm from the target. Neutron energies were measured using time of flight (TOF) technique whereas the $n - \gamma$ discrimination was achieved by pulse shape discrimination (PSD) and time of flight (details given in Chapter 3). To keep the background of the neutron detector at minimum level, the beam dump was kept at 3 m away from the target and was well shielded with layers of lead, concrete and borated paraffin blocks. Empty frame run was taken to estimate the neutron background, which was subsequently used to correct the respective spectrum.

4.2.1 Electronic setup

The block diagram of the electronic setup is shown in Fig. 4.4. Each neutron detector signal was first connected to a splitter to divide the anode pulse into two equal parts without any cable reflection. The splitter circuit is shown in Fig. 4.5. This circuit

serves to distribute a pulse applied to one terminal into two other terminals while maintaining a constant impedance level (50 Ω). One of the splitter outputs was connected to the leading edge discriminator (LED, Phillips Scientific 710) and the other output was connected to the neutron gamma discriminator module (Mesytec MPD4). The LED output of the four neutron detectors were connected to a conincidence unit to extract logic OR output. Detectors of the top and bottom parts of multiplicity filter (25 BaF_2) were connected to 16 channel CAMAC constant fraction discriminators (CFD, CAEN C808). The output currents (1 mA per hit) of the CFDs were summed in a Linear-Fan-in module (CAEN N401). The summed output was fed to a VME QDC (CAEN V792) and integrated for a gate duration of 30 ns to generate, on event-by-event basis, the experimental fold F distribution with condition $F \geq 2$. Here, fold F has been defined as the number of BaF_2 detectors fired simultaneously in an event.

A trigger output was generated from the multiplicity filter array when any detector of the top block and any detector from the bottom block fired in coincidence above a threshold of 200 keV. The final master trigger was generated when, at least two of the multiplicity detectors fired (one from top and one from bottom) in coincidence with any one of the four neutron detectors. This master trigger was connected to the STROBE inputs of the ADC, QDC and common start trigger of TDC. The pulse height (PH) and zero cross over (ZCO) outputs of the MPD4 were directly connected to VME ADC (CAEN V785). Each TDC was stopped by the individual delayed outputs of the MPD4 CFDs for the generation of the individual time of flight (TOF) spectrum for each neutron detector. A dedicated VME based data acquisition (DAQ) system running under LINUX environment, developed at VECC, was used to acquire the data, which were analysed off-line as detailed below.

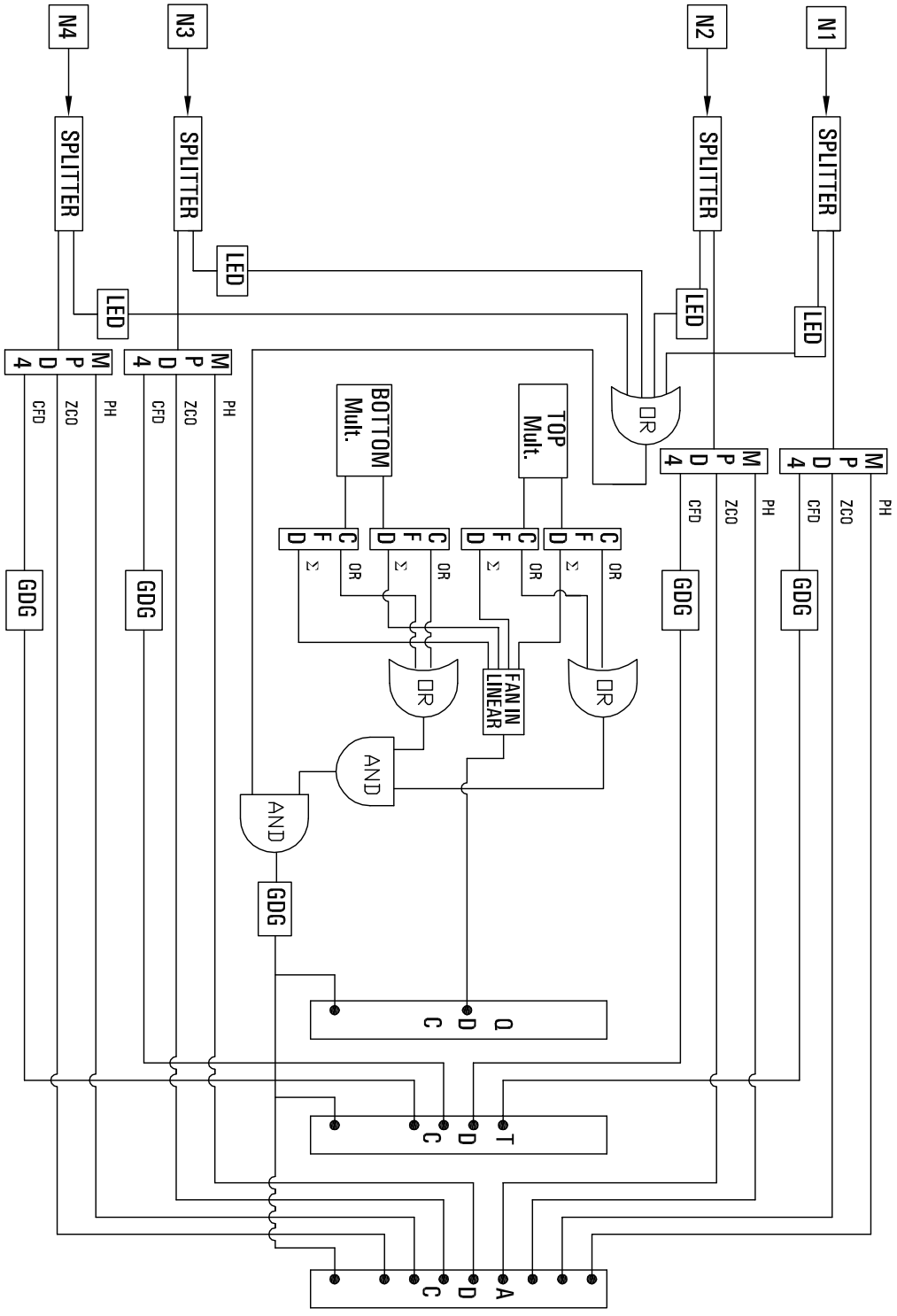

Figure 4.4: *Block diagram of electronic circuit used in the ^{4}He + ^{115}In experiment.*

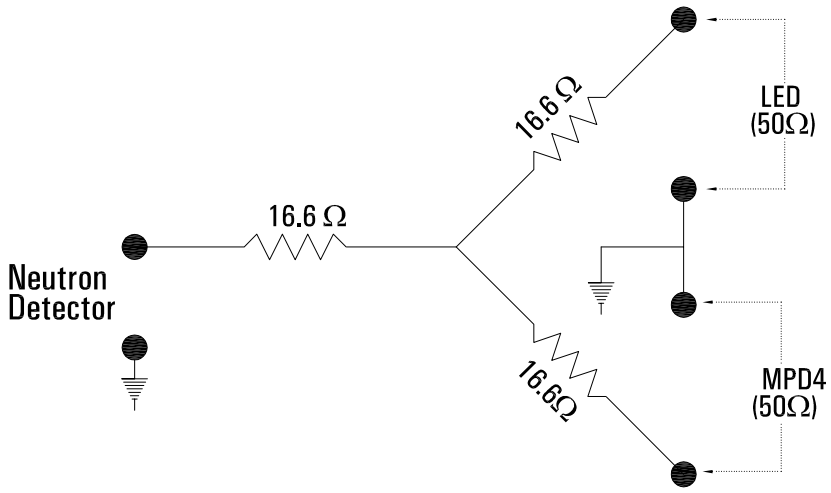

Figure 4.5: *Splitter circuit.*

4.3 Data Analysis

The data were collected on event-by-event basis, each event consisting of information on neutron time of flight (t_n), pulse height (PH), zero cross over of neutrons (ZCO) and γ -ray fold F.

4.3.1 Angular Momentum Distribution

The measured γ-ray fold distribution has been converted, first to multiplicity distribution and then to angular momentum distribution using Monte Carlo simulation technique [Dee10] based on GEANT3 toolkit [Bru86]. Here, fold is the number of BaF_2 detectors fired simultaneously in an event and multiplicity is the actual number of γ rays emitted from the compound nucleus in an event. The realistic experimental conditions (including the detector threshold and the trigger condition) have been taken into account in the simulation. To carry out the simulation, the multiplicity distribution $P(M_\gamma)$ of γ-rays is required, which is linked to the angular momentum distribution of

the compound nucleus. The angular momentum distribution for the simulation calculated using the statistical model code CASCADE [Puh76]. The calculated angular momentum distribution was converted to the multiplicity distribution $P(M_\gamma)$ using the relation

$$J = 2M_\gamma + C \tag{4.1}$$

where the multiplicative factor 2 in M_γ takes into account that each γ -rays are predominantly coming from Yrast decay, which are E2 in nature. The quantity C is a correction factor which takes into account the angular momentum carried out by statistical γ rays and particle decays. In the simulation, the value of C has been varied until the best fit to the experimental fold distribution is achieved. The extracted value of C was 0.5. The multiplicity distribution obtained from the above relation was triangular in shape, which can be expressed as

$$P(M_\gamma) = \frac{2M_\gamma + 1}{1 + exp\Big[\dfrac{M_\gamma - M_\gamma^{max}}{\delta m}\Big]} \tag{4.2}$$

Where M_γ^{max} is the maximum of this distribution and δm is the diffuseness parameter. Different input multiplicities of γ-rays were thus generated using a random number generator according to the multiplicity distribution $P(M_\gamma)$. In the simulation low energy γ -rays of each randomly generated multiplicities M_γ were thrown isotropically from the target centre and the corresponding fold F was recorded for that event. The energy distribution of the triggered γ-rays was obtained from the respective experimental run, exploiting the Gamma Multiplicity filter array itself as a low energy sum spectrometer. The simulated fold spectra were finally compared with the measured one to obtain the best fit (Fig. 4.6a).

Finally, the constraint multiplicity distributions were generated, which contributed to a particular fold window in the total fold distribution spectra. Here the fold win-

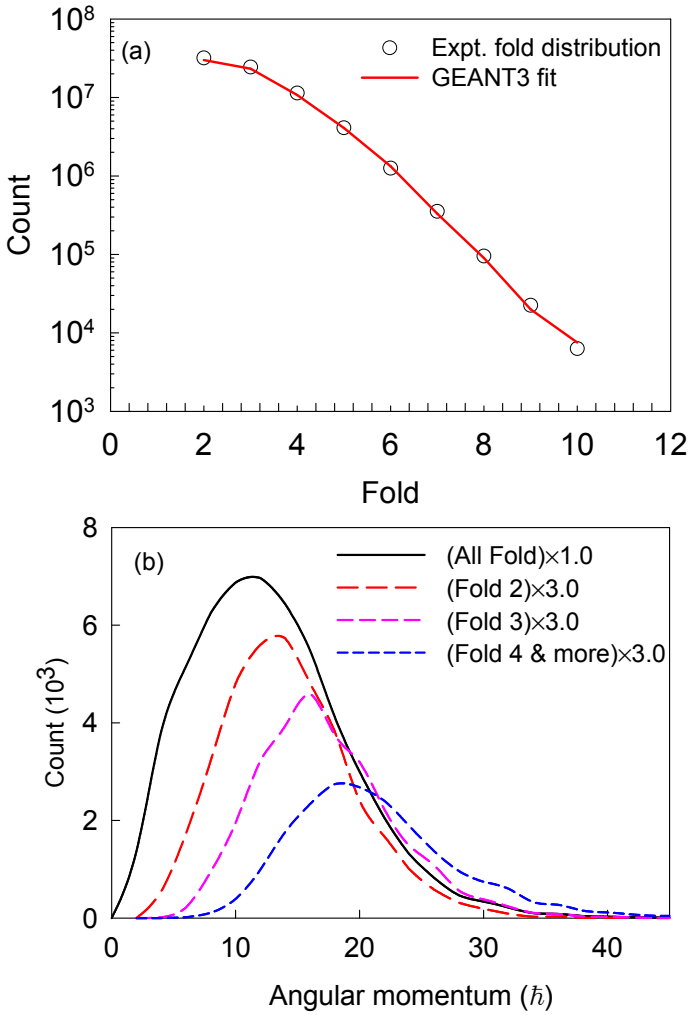

Figure 4.6: *(a) Measured γ-ray fold spectrum for beam energy of 30 MeV fitted with GEANT3 simulation and (b) angular momentum distributions for different folds.*

dows were selected as F = 2, 3 and $\geqslant$ 4. The constraint multiplicity distributions for the above fold windows were converted to the angular momentum distributions. The extracted angular momentum distributions corresponding to different folds of the multiplicity filter have been plotted in the Fig. 4.6b. The extracted values of the average angular momenta $< J >$ corresponding to different γ-ray folds of the multiplicity filter have been given in the Table. 4.1.

4.3.2 Neutron Energy Spectra

A typical two dimensional spectrum of neutron time of flight versus zero cross over has been shown in Fig. 4.7. The neutron TOF were extracted using two dimensional gate as shown in Fig. 4.7. Using the prompt gamma peaks in TOF spectra as time reference, the observed TOF spectra were transformed into energy spectra using proper incorporation of Jacobian. The details of this transformation has already been discussed in chapter 3. The efficiency correction for the neutron detector was done using Monte Carlo Computer code NEFF [Die82]. The contributions from target frame/holder due to the presence of halo beams, if any, have been eliminated using the blank frame run. The laboratory neutron energy spectra were corrected for the background before further analysis as shown in Fig. 4.8.

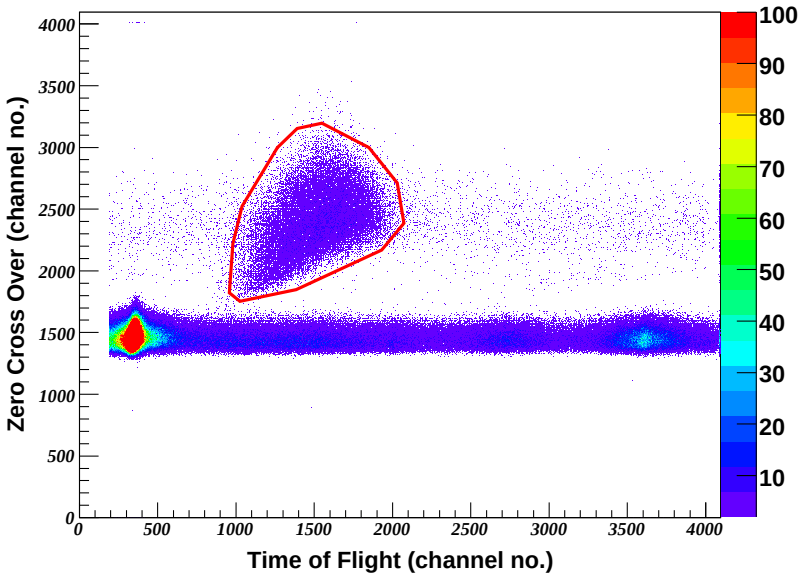

Figure 4.7: *Time of flight vs zero cross over plot. The lower band is due to γ -rays and the upper band is due to the neutrons.*

We have also estimated the scattered neutron contribution due to scattering from the multiplicity filter by comparing the data from two runs, one with full multiplicity

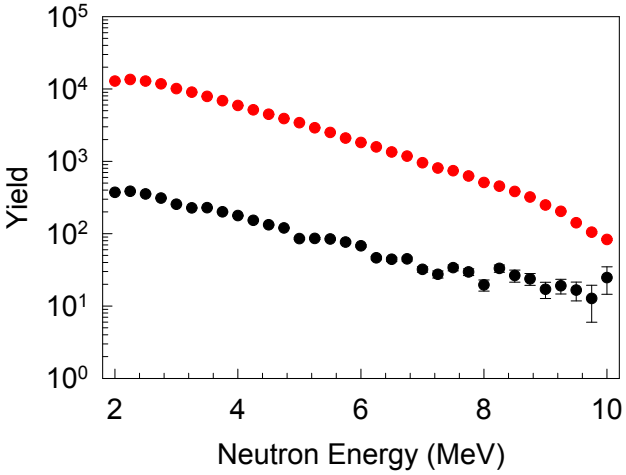

Figure 4.8: *Measured neutron energy spectrum for ^{4}He + ^{115}In at E_{beam} = 42 MeV shown by red solid circles, whereas the background estimated using blank target frame kept at the target position are shown by black solid circles.*

filter (50 detectors) and the other with only the lower part of the filter (25 detectors) in position. In both the cases trigger logic was generated with 25 BaF_2 detectors from the bottom part of multiplicity filter. Fig. 4.9 shows the measured neutron energy spectra in the two cases, the spectra in the two cases are almost same. This indicates negligible contribution of scattered neutron from the multiplicity fillter array. The experimental

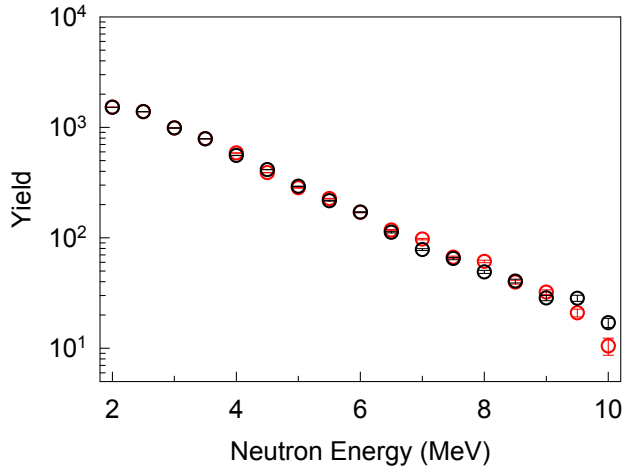

Figure 4.9: *Measured neutron energy spectrum with (red) and without (black) top multiplicity fillter array.*

neutron energy spectra thus obtained at different laboratory angles have been shown in Fig. 4.10 for E_{lab} at 30 MeV and 42 MeV respectively.

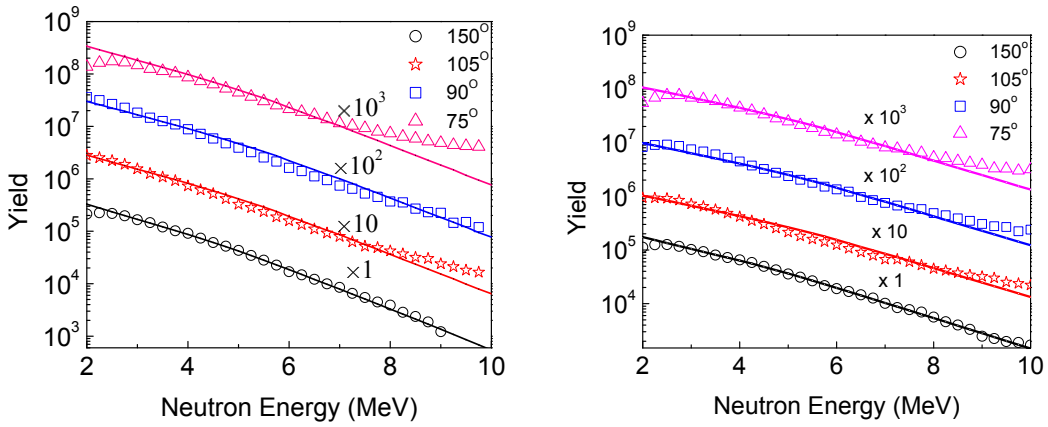

Figure 4.10: *The experimental neutron energy spectra (symbol) at different angles displayed along with the respective statistical model calculations (solid lines) for beam energy of 30 MeV (left side) and 42 MeV (right side).*

4.3.3 Statistical Model Analysis

The theoretical neutron energy spectrum was calculated using the statistical model code CASCADE, using the extracted angular momentum distributions for different folds as input (see Fig. 4.6b). The phenomenological nuclear level density formula (Eq. 1.11) was used in the calculation. The NLD parameter 'a' is related to the density of the single particle levels near the Fermi surface and is influenced by the shell structure and the shape of the nucleus, which in turn depend on excitation energy. Ignatyuk prescription [Ign75] of shell effect in nuclear level density ($a = \tilde{a}[1 - \frac{\Delta S}{U}\{1 - \exp(-\gamma U)\}]$, $U = E^* - E_{rot} - \Delta_P$) was used, where $\tilde{a}$ is the asymptotic Fermi gas value of the liquid drop NLD parameter at the excitation energy where shell effects are depleted leaving a smooth dependence on A. E^*, E_{rot} and Δ_P ($= 12/\sqrt{A}$) are excitation energy, rotational energy and pairing energy of the decaying nucleus respectively. Here ΔS is the shell correction obtained from the difference of the experimental

and the liquid drop model masses and, γ ($\gamma^{-1} = 0.4A^{4/3}/\tilde{a}$) is the rate at which the shell effect is depleted with the increase in excitation energy. The inverse level density parameter k ($k = A/\tilde{a}$) has been tuned in the calculation to reproduce the experimental data. The transmission coefficients were calculated using the optical model, where the optical model parameters for neutron, proton and alpha-particles were taken from refs. [Wil67], [Per63] and [Hui61], respectively. The calculated neutron energy spectrum in the centre-of-mass (c.m.) frame thus obtained was converted to the laboratory (lab) frame using Jacobian transformation as described below. The Kinematic diagram of neutron emission in lab and c.m. frame are shown in Fig. 4.11.

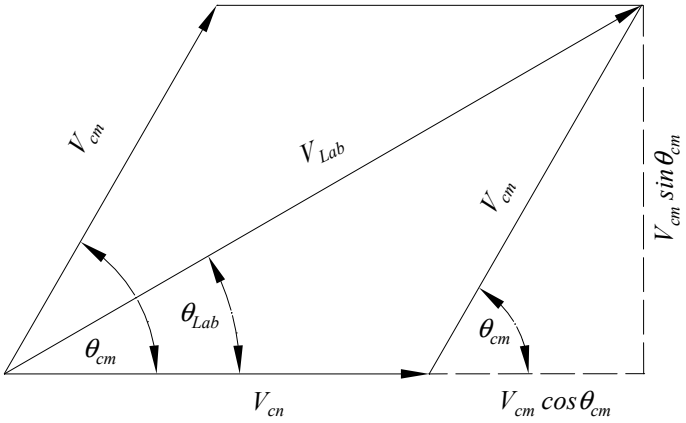

Figure 4.11: *Kinematic of neutron emission in laboratory and centre-of-mass frame.*

$$\left(\frac{d^2\sigma}{dEd\Omega}\right)^{Lab} = \left(\frac{d^2\sigma}{dEd\Omega}\right)^{cm}\left[\frac{(1+\beta^2+2\beta cos\theta_{cm})^{3/2}}{1+\beta cos\theta_{cm}}\right] \tag{4.3}$$

$$\beta = \frac{V_{cn}}{V_{cm}} \tag{4.4}$$

$$tan\theta_{Lab} = \frac{sin\theta_{cm}}{\beta + cos\theta_{cm}} \tag{4.5}$$

$$V_{cn} = \frac{m_p}{m_p + m_t}V_p \tag{4.6}$$

$$V_{cm} = \sqrt{V_{Lab}^2 + V_{cn}^2 - 2V_{Lab}V_{cn}cos\theta_{Lab}} \tag{4.7}$$

Where $\left(\frac{d^2\sigma}{dEd\Omega}\right)^{Lab}$, $\left(\frac{d^2\sigma}{dEd\Omega}\right)^{cm}$, θ_{Lab}, θ_{cm} are the double differential cross-section and angle of evaporated neutron in lab and centre of mass frame respectively. V_{cn}, V_{cm} and V_{Lab} are the velocities of compound nucleus, velocities of neutron in centre of mass frame and in lab frame respectively. m_t, m_p are the mass of the target nucleus, projectile nucleus and V_p is the velocity of the projectile nucleus. The theoretical spectra in the laboratory frame were then folded with time-of-flight energy resolution. This is done using a two dimensional response matrix $R_{i,j}$.

$$\begin{pmatrix} \left(\frac{d^2\sigma_F}{dEd\Omega}\right)_1^F \\ \left(\frac{d^2\sigma_F}{dEd\Omega}\right)_2^F \\ \cdots\cdots\cdots \\ \left(\frac{d^2\sigma_F}{dEd\Omega}\right)_i^F \end{pmatrix} = \begin{pmatrix} \left(\frac{d^2\sigma}{dEd\Omega}\right)_1^{Lab} \\ \left(\frac{d^2\sigma}{dEd\Omega}\right)_2^{Lab} \\ \cdots\cdots\cdots\cdots \\ \left(\frac{d^2\sigma}{dEd\Omega}\right)_j^{Lab} \end{pmatrix} \begin{pmatrix} R_{1,j} & R_{1,j} & \cdots & R_{1,j} & R_{1,j} \\ R_{2,j} & R_{2,j} & \cdots & R_{2,j} & R_{2,j} \\ \cdots & \cdots & \cdots & \cdots & \cdots \\ R_{i,j} & R_{i,j} & \cdots & R_{i,j} & R_{i,j} \end{pmatrix}$$

$\left(\frac{d^2\sigma}{dEd\Omega}\right)^F$ are the resultant double differential neutron cross-section after folding with response matrix, $R_{i,j}$ is a Gaussian function whose width is obtained from the time of flight enegy resolution of the corresponding neutron detector.

$$R_{i,j}(E_i) = \frac{1}{\sqrt{2\pi\sigma_i^2}} exp\left(- \frac{(E_j - E_i)^2}{2\sigma_i^2} \right) \tag{4.8}$$

The time of flight energy resolution of the neutron detector can be described as

$$\frac{\Delta E_i}{E_i} = 2\sqrt{\left(\frac{\Delta L}{L}\right)^2 + \left(\frac{\Delta t_i}{t_i}\right)^2}, \tag{4.9}$$

where, ΔL is the uncertainty in flight path (detector length), ΔE_i is the energy resolution, Δt_i is the time resolution and t_i is the flight time. Here, we have taken Δt_i as the transit time of neutron within the detector at neutron energy E_i. Organic scintillator

detectors are generally having time resolutions of the order of 1 ns, when measured using gamma source. However, in the case of neutron measurement, the time response is mainly determined by the transit time of the neutron within the detector [Kle06]. Transition time is sensitive to flux attenuation and multiple neutron scattering within the detector and therefore strongly depends on the size of the detector, neutron energy and detector threshold. The neutron transit time increases with length or volume of the scintillator and decreases with neutron energy [Kle06]. Transit time of neutron in the detector has been calculated using NRESP7 code [Die82a]. Transit time distribution of 5 MeV neutron and avearge transit time at different neutron energy for $5" \times 5"$ detector are shown in Fig. 4.12.

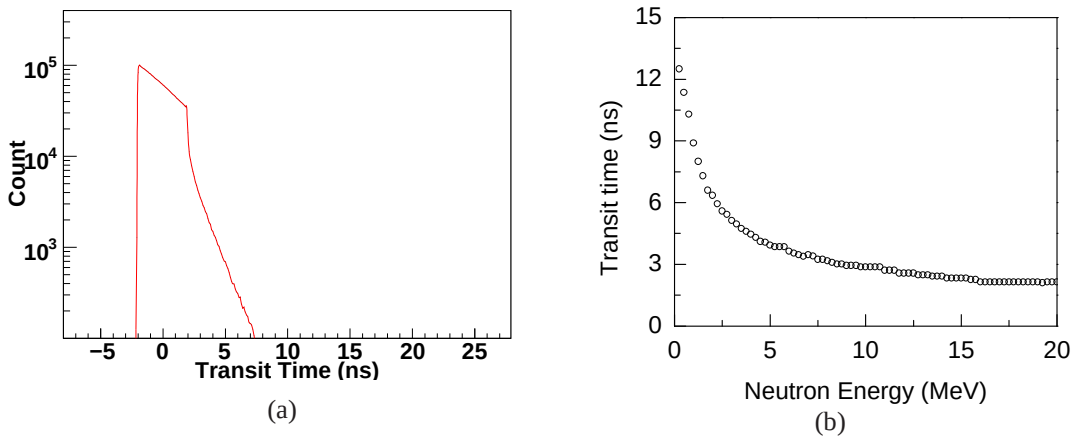

(a) (b)

Figure 4.12: *(a) Transit time distribution of 5 MeV neutron in 5 inch × 5 inch detector, (b) Avearge transit time at different neutron energy for 5 inch × 5 inch detector.*

The folded spectra thus obtained were compared with the measured neutron energy spectra for different γ -ray fold F using χ^2 minimisation technique to obtain the best fit. For the extraction of inverse NLD parameter (k), we have used the neutron data at most backward angle (150°), where the contamination of the neutron spectrum by pre-equilibrium and other direct reaction processes are negligibly small. In the CASCADE calculation it has been observed that the most sensitive parameter influencing the shape

of the neutron spectra is the NLD parameter and the sensitivity is more for the higher energy part of the spectra. The role of the deformability parameters (δ_1 and δ_2 of Eq. 1.12) was found to be insignificant. The Fig. 4.13 shows the effect of δ_1 and δ_2 on the neutron spectra for "all fold" case. The shape of the spectra remains same as we change $\delta_1 = 2 \times 10^{-6}$ and $\delta_2 = 7.9 \times 10^{-9}$ (values calculated using rotating liquid drop model (RLDM) [Coh74]) to $\delta_1 = 2.2 \times 10^{-4}$ and $\delta_2 = 7.9 \times 10^{-7}$.

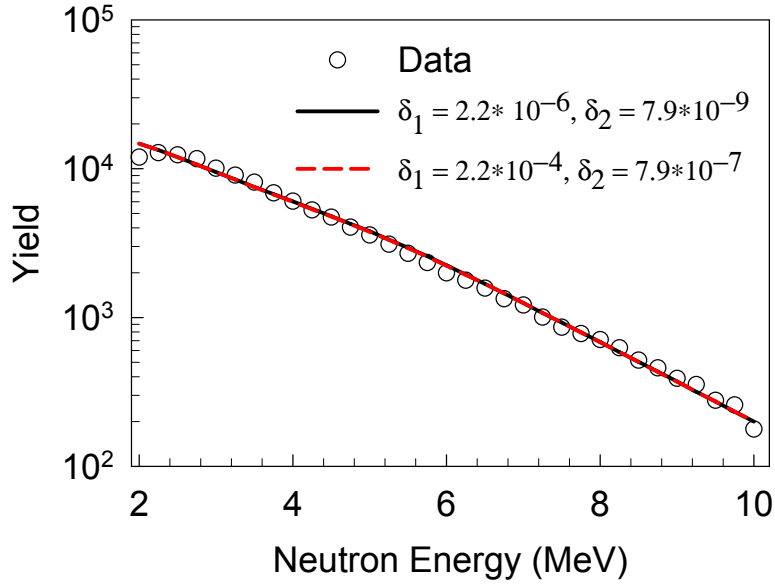

Figure 4.13: *Effect of deformability parameters (δ_1 , δ_2) in determining the shape of the neutron spectra.*

.

The experimental neutron energy spectra at $\theta_{lab} = 150°$ for different gamma-ray folds (all, 2, 3 and 4 & more) for $E_{lab} = 30$ and 42 MeV, together with the respective CASCADE predictions using the best fit values of k, have been presented in Figs. 4.14 and 4.15, respectively. The extracted values of the inverse level density parameters for different multiplicities are given in Table. 4.1. The k value thus obtained was used to calculate the neutron spectra at other angles, which has been shown in Fig. 4.10 along with the experimental spectra for comparison. The k value extracted from the neutron data at 150° angle is found to reproduce the data at 105°, 90° reasonably well. How-

ever some deviation from the CASCADE calculation has been observed for the higher energy tail part of the neutron spectrum at 75°, which may be due to the contributions from other non-equilibrium processes.

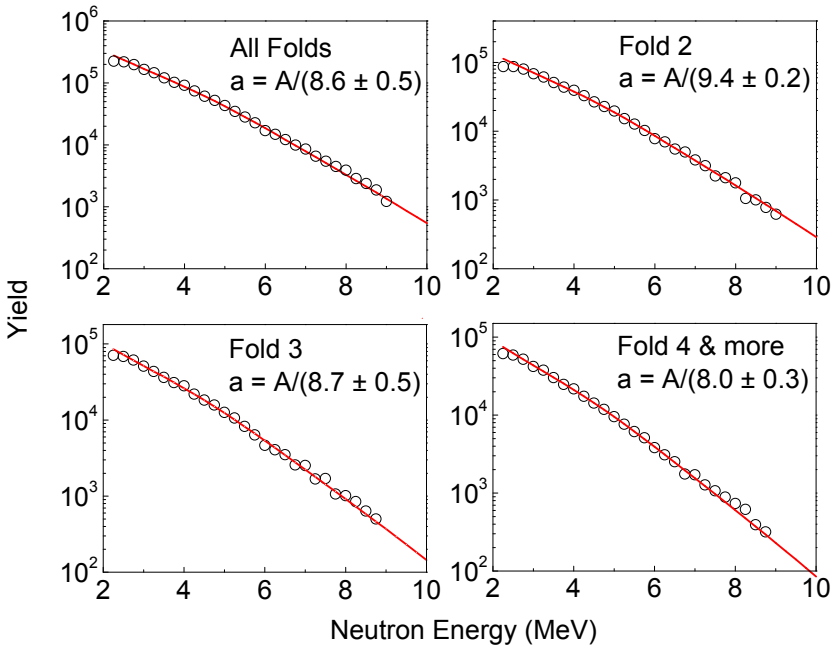

Figure 4.14: *The experimental (E_{lab} = 30 MeV) neutron energy spectra at θ_{lab} = 150° for different γ-ray folds (circles) displayed along with the respective CASCADE predictions (red solid lines), errors are within the symbol.*

Table 4.1: *Measured values of γ fold, avgerage angular momentum, inverse level density parameter and temperatures.*

Beam energy (MeV)	Fold	$< J >$ ($\hbar$)	k (MeV)	$T1$ (MeV)	$T2$ (MeV)	$T3$ (MeV)
30	All	15.0±5.9	8.6±0.5	0.98±0.03	0.53±0.02	
30	2	12.6±4.9	9.4±0.2	1.05±0.01	0.61±0.01	–
30	3	15.5±5.2	8.7±0.5	0.97±0.03	0.52±0.02	
30	4&more	19.7±6.2	8.0±0.3	0.87±0.02	0.38±0.01	
42	All	16.9±6.4	9.8±0.2	1.39±0.01	1.05±0.01	0.39±0.01
42	2	14.1±5.2	11.1±0.3	1.51±0.02	1.16±0.02	0.51±0.01
42	3	16.8±5.4	9.5±0.5	1.36±0.03	1.04±0.03	0.39±0.01
42	4&more	21.1±6.8	8.9±0.3	1.26±0.02	0.93±0.02	0.12±0.01

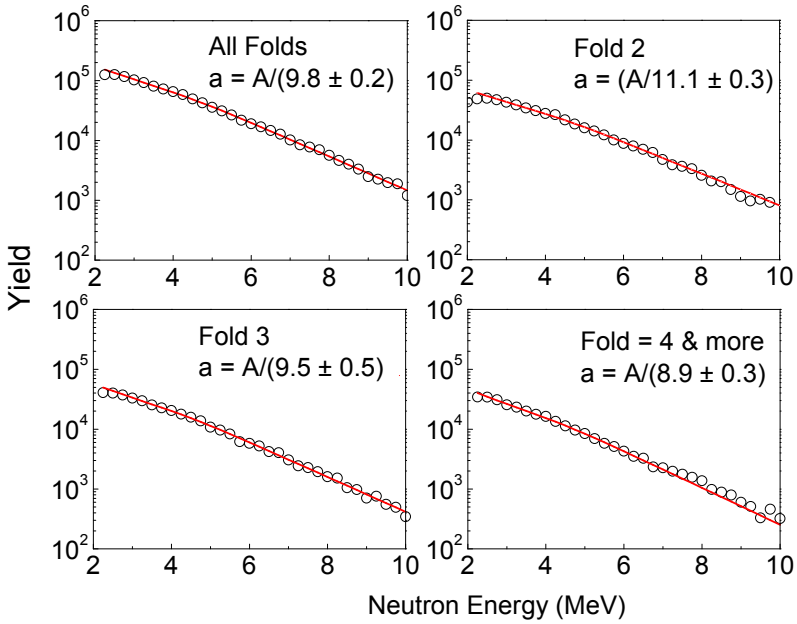

Figure 4.15: *The experimental (E_{lab} = 42 MeV) neutron energy spectra at θ_{lab} = 150° for different γ-ray folds (circles) displayed along with the respective CASCADE predictions (red solid lines).*

4.4 Results and Discussions

The theoretical fits to the neutron energy spectra for different folds as shown in fig. 4.14 and 4.15 indicate that the best-fit values of the level density parameter tend to increase at higher J values. For example, the value of a changes from A/9.4 (fold 2) to A/8 (fold 4 & more) for E_{lab} = 30 MeV and from A/11.1 (fold 2) to A/8.9 (fold 4 & more) for E_{lab} = 42 MeV. This indicates that there is enhancement of level density with the increase in angular momentum. The angular momentum dependence in NLD is generally taken care through the rotational energy E_{rot} where the effect of angular momentum dependent deformation on the decay is introduced by the effective moment of inertia ($\Im_{eff}$). The deformability parameters (δ_1 and δ_2), which are generally adjusted to take care of the angular momentum dependent deformation is insensitive in the present case and therefore failed to reproduce the fold gated particle spectra.

The average temperatures corresponding to the measured neutron spectra were found to be $\sim$ 1 MeV and 1.4 MeV for incident energies of 30 MeV and 42 MeV, respectively. In both cases, the average temperatures are above T_c (see Eq. 1.21); therefore, the collective enhancement due to ground state deformation is expected to be less significant. In order to look into the above more deeply, we have investigated the characteristics of the neutrons emitted at intermediate stages. For this study, the present system seems to be advantageous as there is predominantly only one residue and that too is populated through a single path ($2n$ and $3n$ channels at E_{lab} = 30 and 42 MeV, respectively). Fig. 4.16 shows a typical statistical model calculation of the neutron energy spectra from the nuclei produced at various intermediate stages of the decay cascade. It is seen that the slopes (and temperatures) of the neutron energy spectra are different at different stages. The nuclear temperatures at different stages (T_1, T_2 and T_3) have been extracted and tabulated in Table. 4.1 using the relation $U = aT^2$, where,

$$U = E^* - E_{rot} - S_n - < E_n >, \tag{4.10}$$

The neutron separation energies S_n for ^{119}Sb, ^{118}Sb, ^{117}Sb are 9.5, 7.4, 9.8 MeV, respectively [NND12]. The average kinetic energies $< E_n >$ have been estimated from the respective energy spectra. For the present system, the critical temperature calculated using Eq. 1.21 is 0.99 MeV. It is clear from Table. 4.1 that for each fold, the temperature is above the critical temperature in the initial decay stage; however, during the final decay stage, it is well below the critical temperature. Therefore the collective enhancement in NLD may not be ignored completely. So the enhancement in level density visible in the present case may be, at least partially, due to the ground state deformation. Further systematic study in this direction is however needed to understand the variation of nuclear level density with angular momentum and also to elucidate the mechanism of enhancement of NLD observed in the present measurement.

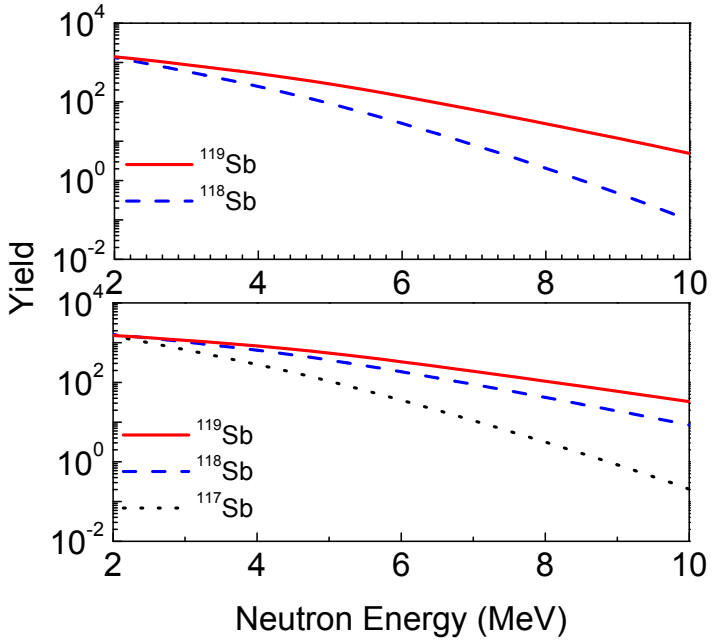

Figure 4.16: *CASCADE calculated neutron energy spectra from different stages of decay chain. Figure in the top for E_{lab} = 30 MeV, in bottom for E_{lab} = 42 MeV.*

Chapter 5

Summary and Conclusion

The aim of the present research was to study the properties of atomic nuclei using neutron as a probe. Under the present thesis work we have developed two types of neutron detectors for neutron energy and multiplicity measurements. Energy measurement was done by time of flight (TOF) technique using small volume (1.5 litres) liquid scintillator detector, whereas Gd loaded large volume (500 litres) liquid scintillator detector was fabricated for multiplicity measurement. TOF neutron detectors of various dimensions have been designed and fabricated to study the various characteristics (absolute neutron detection efficiency, pulse shape discrimination and intrinsic time resolution) of the neutron detector and their dependence on the detector dimension. Efficiency measurements have been done with associated charge particle coincidence method using a ^{252}Cf fission neutron source placed inside a multi wire proportional counter. The measured and simulated efficiencies seem to be consistent within experimental error. The detection efficiency was found to increase with the increase in detector dimension. The quality of n-γ discrimination was found to deteriorate and the time resolution were broader with the increase in size of the detector. It was also observed that the figure of merit (M) of n -γ discrimination initially increased with the increase in threshold and then got saturated. From the above study it was evident that, $5'' \times 5''$ and $7'' \times 5''$ detectors will be the optimum for higher energy neutron measurements, considering

their higher efficiencies, reasonably good figure of merit and intrinsic time resolution. On the basis of above the study, a time of flight array consisting of 50 detectors having dimensions $5'' \times 5''$ and $7'' \times 5''$ is being developed for experiments using K 500 super-conducting cyclotron at VECC, presently undergoing commissioning trials.

Apart from the neutron energy distribution, the total number of neutrons emitted in an event (neutron multiplicity) also plays a crucial role in determining the reaction mechanism, particularly in the Fermi energy domain. However, neutron measurement using time of flight technique is not generally quite efficient to estimate the neutron multiplicity very accurately on event by event basis. So the other alternative and rather economical solution is to use a single, large volume detector which should be highly efficient in neutron detection. This idea prompted us to built a 4π liquid scintillator detector for multiplicity measurement. This detector consisted of two stainless steel hemispheres of one metre diameter and filled with 500 litres of 0.5% Gd loaded liquid scintillator BC521.

The neutron capture time distribution has been experimentally measured using a novel technique with a small volume detector ($\sim$ 8 litre) in conjunction with BaF_2 detectors. Capture time distributions were also estimated using Monte Carlo simulation, the simulated results were found to be in good agreement with the measured data. 4π neutron multiplicity detector has been tested with ^{252}Cf spontaneous fission source. The measured neutron multiplicity was 4, which is consistent with literature value [Sch95].

Under this thesis work two physics experiments have been performed with the indigenously developed neutron detectors. The first experiment was performed to study the fission dynamics in ^{16}O + ^{238}U reaction at near barrier energies (E_{lab} = 83, 85, 87, 89, 92, 96 and 100 MeV). Two MWPCs were used to detect fission fragments and four liquid scintillator based detectors were used to detect neutrons produced in the reac-

tion. The measured mass distribution result clearly showed a sharp change in the mass distribution width (σ_m) as energy decreased to below barrier energies. The increase in width of the mass distribution is a clear indication of a sudden qualitative change in the degree of mass equilibration in ^{16}O + ^{238}U system at below barrier energies, which may be considered to be a strong evidence for onset of quasi-fission. This is thus reaffirming the observation made earlier on the onset of quasi-fission at below barrier energies for the same system from the study of fission fragment angular anisotropy measurement [Hin95]. On the contrary, present measurement of pre-scission neutron multiplicity for the same system at above and below barrier energies was clearly consistent with the standard statistical model prediction; this apparently indicates that quasi-fission does not significantly modify the complete fusion yield (and vis-a-vis M_n^{pre}) for this system even at below barrier energies. Similar inference was drawn from the study of evaporation residue measurements for the same system [Nis04], where, too, no departure from statistical model prediction was seen.

In the present case, which is highly asymmetric ($Z_{proj}{\cdot}Z_{target}$ = 736) the contribution of quasi-fission from the present data was found to be $\sim$ 5 – 6%, which is much smaller than the fusion-fission cross section. Hence the change in ER cross-section may not be appreciable to be detected unambiguously. However, previous ER measurement for more symmetric systems ($Z_{proj}{\cdot}Z_{target} \gtrsim 1500 - 1600$), where the quasi-fission fraction is comparable or even larger than the fusion-fission, showed considerable reduction in ER formation [Nis10]. Same argument holds for pre-scission neutron multiplicity also. Therefore, although the present observation of the sudden change in fragment mass distribution width along with the earlier observation of anomalous fragment angular anisotropy confirm the onset of quasi-fission of ^{16}O + ^{238}U system at below barrier energies, the present measurement of prescission neutron multiplicity as well as the earlier measurement of evaporation residue yield do not show any de-

parture from standard statistical model predictions, indicating the insensitivity of these two probes for highly asymmetric system with low $Z_{proj}{\cdot}Z_{target}$ ($\ll$ 1500-1600) value. For more symmetric system with higher $Z_{proj}{\cdot}Z_{target}$ value, where the QF and FF fractions are comparable, both M_n^{pre} and ER yields may also be equally sensitive for such studies.

The second experiment carried out under the present thesis work was to study nuclear level density and its dependence on angular momentum. ^{119}Sb* was populated using light ion route (^{4}He + ^{115}In), which resulted in a single residue ^{117}Sb (90%), ^{116}Sb (77%) by 2n and 3n evaporation channel at E* = 31.3 MeV, 42.9 MeV respectively. Four liquid scintillator based detectors and an array of 50 BaF_2 detectors were used to measure the energy spectra of evaporated neutrons in coincidence with the γ-ray fold. Measured γ-ray fold distribution was converted to angular momentum distribuiton using Monte Carlo simulation technique [Dee10] based on GEANT3 toolkit [Bru86]. The neutron energy distributions were then calculated using the statistical model code CASCADE [Puh76] in different angular momentum regions as estimated from the measured γ -rays fold distributions. The nuclear shape changes at higher angular momentum [Coh74] and shell effect in nuclear level density [Ign75] were incorporated in the statistical model calculations. In the analysis it was observed that, the inverse level density parameter (k) is the only sensitive parameter as far the slope of the neutron energy spectrum is concerned. The estimated neutron energy spectra were then compared with the measured neutron energy spectra for γ-ray fold F = 2, 3 and 4 & more, using χ^2 minimisation technique. The analysis of the γ-ray fold gated neutron energy spectrum reveals that the inverse level density parameter (k) decreases with the increase in J. This is indicative of the fact that ρ increases with J. This increase may be due to either the change in nuclear shapes with angular momentum or due to collective enhancement of level density due to ground state deformation.

The effect of nuclear shape changes at higher angular momentum has been ruled out as in the present case there has been almost no change in moment of inertia over the whole range of angular momentum studied here. On detailed analysis of the neutron spectra from the intermediate stages of decay, it was observed that, the temperature during the final stage of decay chain is always much less than the critical temperature (T_c) for collective enhancement. So, there is a finite possibility that the enhancement of NLD, or at least a part of it, is due to the presence of ground state deformation in the present case. Further systematic study in this direction is however needed to understand the variation nuclear level density with angular momentum and also to elucidate the mechanism of enhancement of NLD observed in the present measurement.

Bibliography

[Agg10] M. Aggarwal and S. Kailas Phys. Rev. C **81**, 047302 (2010).

[Ago03] S. Agostinelli et al., GEANT4- A simulation toolkit, et al., Nucl. Instr. and Meth. A **506**, 250 (2003).

[Ahm77] M. Ahmed Nucl. Instr. and Meth. **143**, 255 (1977).

[Bac81] B. B. Back et. al., Phys. Rev. Lett, **46**, 1068, (1981).

[Bac83] B. B. Back et. al., Phys. Rev. Lett, **50**, 818, (1983).

[Bac85] B. B. Back et. al., Phys. Rev. C, **32**, 195, (1985).

[Bac96] B. B. Back et. al. Phys. Rev. C, **53**, 1734 (1996).

[Ban09] K. Banerjee et. al. Nucl. Instr. Meth. A **608**, 440 (2009).

[Ban87] Asismoy Bandyopadhyay et. al. Nucl. Instr. and Meth. A **257**, 309 (1987).

[Bas80] Reiner Bass, Nuclear Reaction with Heavy Ions, Springer- Verlag, Berlin (1980),Chapter 7.

[Beg06] F. Begin et. al., Nucl. Inst. and Meth. A **562**, 351 (2006).

[Ber82] V. Bernand et. al., Nucl. Phys. A **385**, 319 (1982).

[Bet36] H. A. Bethe, Phys. Rev. **50**, 332 (1936).

[Bla52] J. M. Blatt and V. F. Weisskopf, Theoretical Nuclear Physics (Wiley, New York, 1952).

[Boh39] N. Bohr and J. A. Wheeler, Phys Rev **56**, 426 (1939).

[Boh53] A. Bohr, B. R. Mottelson, Kgl. Danske Videnskab. Selskab, Mat. Fys. Medd. **27**, 16 (1953).

[Boj73] S. Björnholm, A. Bhor and Mottelson, in Proceedings of the International Conference on the Physics and Chemistry of Fission, Rochester, New York, 1973 (IAEA, Vienna, 1974) Vol. 1, p. 367.

[Bre84] Breskin et. al., Nucl. Instr. and Meth. **221**, 363 (1984).

[Bri00] J. F. Briesmeister (Ed.), MCNP -A general Monte Carlo N-Particle Transport Code, Los Alamos, (LA-13709-M),2000.

[Bru86] R. Brun, et al., GEANT3, CERN-DD/EE/84-1, 1986.

[Cap09] R. Capote et. al., Nuclear Data Sheet **110**, 3109 (2009).

[Cec79] R. A. Cecil, B.D. Anderson and R. Madey, Nucl. Instr. and Meth. **161**, 439 (1979).

[Cha05] R. J. Charity and L. G. Sobotka, Phys. Rev. C **71**, 24310 (2005).

[Cha10] R. J. Charity, Phys. Rev. C **82**, 014610 (2010).

[Chi03] A. Yu. Chizhov et. al., Phys. Rev. C **67**, 011603(R) (2003).

[Cho93] H.P.Chou et. al., Nucl. Instr. Meth. A **328**, 522 (1993).

[Coh63] S. Cohen and W. J. Swiatecki, Ann. Phys. (NY) **22**, 406, (1963).

[Coh74] S. Cohen, F. Plasil and W. J. Swiatechi, Ann. Phys. (NY)**82**, 557 (1974).

[Cra70] R. L. Craum and D. L. Smith, Nucl. Instr. and Meth. A **80**, 239 (1970).

[Cub89] J. Cub et al., Nucl. Instr. and Meth. A **274**, 217 (1989).

[Dee10] Deepak Pandit et. al., Nucl. Instr. Meth. A **624**, 148 (2010).

[Dek87] E. Dekempeneer, H. Liskien, et al., Nuclear Instruments and Methods in Physics Research A **256**, 489 (1987).

[Dem01] P. Demetriou and S. Goriely, Nuclear Physics A **695**, 95 (2001).

[Dic88] J. K. Dickens, ORNL-6436, Oak Ridge National Laboratory, 1988.

[Die82] Dietze and Klein, Nucl. Instr. and Meth. A **193**, 549 (1982).

[Die82a] G. Dietz and H. Klein, PTB-ND-22 Report (1982).

[Don99] L. Donadille et. al., Nucl. Phys A **656**, 259 (1999).

[Fas03] Fasso et. al., The Physics model of FLUKA: status and recent developments, in: Computing in High Energy and Nuclear Physics 2003 Conference (CHEP2003), La Jolla, CA, USA, 24-28 March 2003, (paper MOMT005), eConf C0303241 (2003), arXiv:hep-ph/0306267.

[Fas05] Fasso, A. Ferrari, J. Ranfit, P.R. Sala, Fluka: a multi-particle transport code, CERN-2005-10, INFN/TC_05/11, SLAC-R-773, 2005.

[Fre86] R.Freifelder, M. Prakash and John M. Alexander, Phys. Rep **133**, 315 (1986).

[Gho04] T. K. Ghosh et. al., Phys. Rev. C **69**, 031603(R) (2004).

[Gho05] T. K. Ghosh et. al., Phys. Lett. B **627**, 26 (2005).

[Gho05a] T. K. Ghosh, PhD Thesis, Jadavpur University, 2005.

[Gho09] T. K. Ghosh et. al., Phys Rev C **79**, 054607 (2009).

[Gil65] A. Gilbert, F. S. Chen, and A. G. W. Cameron, Can. J. Phys. **43**, 1248 (1965).

[Gil65a] A. Gilbert and A. G. W. Cameron, Can. J. Phys. **43**, 1446 (1965).

[Gho05b] T. K. Ghosh et. al., Nucl. Instr . Meth. A **540**, 285 (2005).

[Gul89] K. Gul et al., Nucl. Instr. and Meth. A **278**, 470 (1989).

[Gup08] Y. K. Gupta et. al., Phys. Rev. C **78**, 054609 (2008).

[Gup09] Y. K. Gupta et. al., Phys. Rev. C **80**, 054611 (2009).

[Hag88] K. Hagel et. al., Nucl. Phys. A **486**, 429 (1988).

[Hau52] W. Hauser and H. Feshbach, Phys. Rev. C, **87**, 366 (1952).

[Hen88] S. Henss et. al., Phys. Rev. Lett **60**, 11 (1988).

[Her05] M. Herman et. al., Empire Nuclear Reaction Model Code Instruction Manual (March 22, 2005).

[Hil53] D. L. Hill and J. A. Wheeler, Phys. Rev. **89**, 1102 (1953).

[Hil79] D. Hilscher et. al., Phys. Rev. C **20**, 576 (1979).

[Hin89] D. J. Hinde et. al., Nucl. Phys. A **502**, 497c (1989).

[Hin95] D. J. Hinde et. al., Phys. Rev. Lett, **74**, 1295 (1995).

[Hin02] D. J. Hinde et. al., Phys. Rev. Lett, **89**, 282701 (2002).

[Hin08] D. J. Hinde et. al., Phys. Rev. Lett. **100**, 202701 (2008).

[Hod78] P. E. Hodgson, Nuclear Heavy-ion Reactions, Clarendon Press Oxford (1978), Chapter 4.

[Hor00] Horvath et al., Nucl. Instr. and Meth. A **440**, 241 (2000).

[Hua00] Po-lin Huang, S. M. Grimes, and T. N. Massey, Phys. Rev. C **62**, 024002 (2000).

[Hui61] J. R. Huizenga and G. Igo, Nucl. Phys. **29**, 462 (1961).

[Ign75] A.V. Ignatyuk, G.N. Smirenkin and A.S. Tishin, Sov. J. Nucl. Phys. **21** 255 (1975).

[Ign79] A. V. Ignatyuk, K. K. Istekov and G. N. Smirenkin, Sov. J. Nucl. Phys. **29**, 450 (1979).

[Itk04] M. G. Itkis *et al.*, Nucl. Phys. A **734**, 136 (2004).

[Jah03] U. Jahnke et al., Nucl.Instr. and Meth. A **508**, 295 (2003).

[Jah83] U. Jahnke et. al., Lecture Notes in Physics (Springer Verl. Berlin) 178 (1983).

[Jas04] S. D. Jastaniah, P.J. Sellin, Nucl. Instr. A **517**, 202 (2004).

[Jil08] Jhilam Sadhukhan and Santanu Pal, Phys. Rev. C **78**, 011603 (2008), Phys Rev C **79**, 019901 (2008).

[Jun98] A. R. Junghans et. al., Nucl. Phys. A **629**, 635 (1998).

[Kal70] J. Kalyna and I.J. Taylor, Nucl. Instr. and Meth. **88**, 277 (1970).

[Kat78] S. K. Kataria, V. S. Ramamurthy and S. S. Kapoor, Phys. Rev. C **18**, 549 (1978).

[Kle02] H. Klein, S. Neumann, Nucl. Instr. and Meth. A **476**, 132 (2002).

[Kle06] H. Klein, F.Brooks, PoS (FNDA2006) 097.

[Kno00] G. F. Knoll, Radiation Detection and Measurement, 3rd Edition, John Wiley and Sons (2000), Inc, Chapter 1.

[Kom07] S. Komarov et. al., Phys. Rev. C **75**, 064611 (2007).

[Kra40] H. A. Kramers, Physica **7**, 284 (1940).

[Lang93] G. H. Lang et. al., Phys. Rev. C **48**, 1518 (1993).

[Lie98] E. Lienard et al., Nucl.Instr. and Meth. A **413**, 321 (1998).

[Lig04] P. K. Lightfoot et. al., Nucl. Instr. A **522**, 439 (2004).

[Maj95] N. Majumdar et. al., Phys. Rev. C **51**, 3109 (1995).

[May49] M. G. Mayer, Phys. Rev. **75** , 1969 (1949).

[Mit02] A. Mitra et al., Nucl. Phys. A **707**, 343 (2002).

[Mit06] A. Mitra et al., Nucl. Phys. A **765**, 277 (2006).

[Mol09] Peter Moller et. al., Phys Rev C **79**, 064304 (2009).

[Mol95] P. Möller et. al., Atomic Data and Nuclear data Table **59**, 185 (1995).

[Mos94] M. Moszynski et. al., Nucl. Instr. and Meth. A **350**, 226 (1994).

[Nak97] H. Nakada and Y. Alhassid, Phys. Rev. Lett **79**, 2939 (1997).

[Neb86] G. Nebbia et. al., Phys. Lett. B **176**, 20 (1986).

[New90] J.O. Newton, Sov. J. Nucl. Phys. **21**, 349 (1990).

[Nis04] K. Nishio et. al., Phys. Rev. Lett. **93**, 162701 (2004).

[Nis08] K. Nishio et. al., Phys. Rev. C **77**, 064607 (2008).

[Nis10] K. Nishio *et al.,* Phys. Rev. C **82**, 024611 (2010).

[NND12] www.nndc.bnl.gov.

[Nov97] T. Novotny, Photon Spectrometry in Mixed Neutron Photon Fields Using NE213 Liquid Scintillator Detectors, PTB-Report PTB-N-28, Breunschweig, 1997.

[Per63] F. G. Perey, Phys. Rev. **131**, 745 (1963).

[Poi74] J. Poitou et al., Nucl. Instr. Meth. **114**, 113 (1974).

[Puh76] F. Puhlhofer, Nucl. Phys. A **280**, 267 (1976).

[Raf08] R. Rafiei et. al., Phys Rev C **77**, 024606 (2008).

[Ram85] V. S. Ramamurty and S. S. Kapoor, Phys. Rev. Lett. **54**, 178 (1985).

[Ram90] V. S. Ramamurty et. al., Phys. Rev. Lett. **65**, 25 (1990).

[Rid74] R. A. J. Riddle et al., Nucl. Instr. and Meth. **121**, 445 (1974).

[Rob81] Robert E. Howe Nucl. Instr. and Meth. **190**, 309 (1981).

[Ros89] H. Rossner, D. Hilscher, D. J. Hinde, B. Gebauer, M. Lehmann, M. Wilpert, E. Mordhorst, Phys Rev. C **40**, 2629 (1989).

[Rei04] A. J. Reiter, PhD Thesis, University of Glasgow, 2004.

[Sag03] R. N. Sagaidak et. al., Phys. Rev .C **68**, 014603 (2003).

[Sch95] W. U. Schröder, DOE/ER/79048-1.

[She87] W. Q. Shen et al., Phys. Rev. C **36**, 115 (1987).

[Shl90] S. Shlomo and J. B. Natowitz, Phys. Lett. B **252**, 187 (1990) and reference therein.

[Shl91] S. Shlomo and J. B. Natowitz, Phys. Rev. C **44**, 2878 (1991).

[Sie86] Arnold J. Sierk, Phys. Rev. C **33**, 2039 (1986).

[Sod08] P.A. Söderström. Proceedings of the International School of Physics 'Enrico Fermi', volume 169 page 551. SIF, Bologna and IOS Press, Amsterdam, 2008.

[Spe74] P. Sperr et. al., Nucl. Instr. and Meth. **116**, 55 (1974).

[Tak93] A. Takahiko et. al., Nucl. Instr. Meth. A **333**, 492 (1993).

[Tho64] T. D. Thomas, Nucl. Phys. **53**, 577 (1964).

[Tok85] J. Toke et al., Nucl. Phys. A **440**, 327 (1985).

[Ven08] S. Venkataramanan et.al., Nucl. Instr. Meth. A **596**, 248 (2008).

[Vio85] V. E. Viola, K. Kwiatkowski, M. Walker, Phys. Rev. C **31**, 1550 (1985).

[Wei37] V. Weisskopf, Phys. Rev. **52**, 295 (1937).

[Wei40] V. Weisskopf and D. H. Ewing, Phys. Rev. **57**, 472 (1940).

[Wil67] D. Wilmore and P. E. Hodgson, Nucl. Phys. **55**, 673 (1964).

[Win71] R. A. Winyar et al., Nucl. Instr. and Meth. **95**, 141 (1971).

[Zhe84] Z. Zheng et. al., Nucl. Phys. A **422**, 447 (1984).

List of Publications

(A) Relevant to the present Thesis

In refereed journals

1. *"Variation of nuclear level density with angular momentum"*, **K. Banerjee**, S. Bhattacharya, C. Bhattacharya, M. Gohil, S. Kundu, T. K. Rana, G. Mukherjee, R. Pandey, P. Roy, H. Pai, A. Dey, T. K. Ghosh, J. K. Meena, S. Mukhopadhyay, D. Pandit, S. Pal, and S. R. Banerjee **Phys. Rev. C 85, 064310 (2012)**.

2. *"Evidence of quasi fission in ^{16}O + ^{238}U reaction at sub barrier energies"*, **K. Banerjee**, T.K. Ghosh, S. Bhattacharya, C. Bhattacharya, S. Kundu, T. K. Rana, G. Mukherjee, J. K. Meena, J. Sadhukhan, S. Pal, P. Bhattacharya, K. S. Golda, P. Sugathan, R. P. Singh **Phys. Rev. C 83, 024605 (2011)**.

3. *"Variation of neutron detection characteristics with dimension of BC501A neutron detector"*, **K. Banerjee**, T. K. Ghosh, S. Kundu, T. K. Rana, C. Bhattacharya, J. K. Meena, G. Mukherjee, P.Mali, D. Gupta, S. Mukhopadhyay, D. Pandit, S. R. Banerjee , S.Bhattacharya, T. Bandyopadhyay, S.Chatterjee, **Nucl. Instr. and Meth. A, 608, 440 (2009)**.

4. *"Characteristics of Gd-loaded liquid scintillators BC521 and BC525"*, **K. Banerjee**, S. Kundu, S. Mukhopadhyay, T.K. Rana, S. Bhattacharya, C. Bhattacharya, S. R. Banerjee, T.K. Ghosh, G. Mukherjee, T. Bandyopadhyay, A. Dey, J. K. Meena, P. Mukhopadhyay, D. Gupta, S. Pal, D. Pandit, S. Bhattacharya, **Nucl. Instr. and Meth. A, 580, 1383 (2007)**.

In Conferences

1. "*Extraction of angular momentum gated nuclear level density parameter*", **K Banerjee** et. al. Proc. of DAE -BRNS Symp. on Nucl. Phys. 56, 594 (2011).

2. "*Angular momentum gated neutron evaporation studies"* **K. Banerjee** et. al., Proc. of DAE -BRNS Symp. on Nucl. Phys., 55, 324 (2010).

3. "*Development of liquid scintillator based Neutron Detector"*, **K. Banerjee** et.al, Proc. of DAE -BRNS Symp. on Nucl. Phys., 51, 624 (2006).

4. "*Capture time distribution study in Gd loaded liquid scintillator"*, **K. Banerjee** et.al, Proc. of DAE -BRNS Symp. on Nucl. Phys., Vol. 51, 588 (2006).

5. "*Simulation result of 4π neutron multiplicity detector"*, **K.Banerjee**, et.al, Proc. of DAE -BRNS Symp. on Nucl. Phys., 50, 440 (2005).

6. "*Simulation study of liquid scintillator based 4π neutron detector"*, **K.Banerjee**, et.al, Proc. of DAE -BRNS Symp. on Nucl. Phys., 49, 524(2004).

(B) Other Publications (in refereed journals)

1. "*Measurement and simulation of neutron response function of organic liquid scintillator detector"*, M. Gohil, **K.Banerjee**, S. Bhattacharya, C. Bhattacharya, S. Kundu, T. K. Rana, G. Mukherjee, J. K. Meena, R. Pandey, H. Pai, T. K. Ghosh, A. Dey, S. Mukhopadhyay, D. Pandit, S. Pal, S. R. Banerjee, T. Bandopadhyay, **Nucl. Instr. and Meth. A 664, 304 (2012)**.

2. "*Complex-fragment emission in low-energy light-ion reactions"*, S. Kundu, C. Bhattacharya, **K. Banerjee**, T. K. Rana, S. Bhattacharya, A. Dey, T. K. Ghosh, G. Mukherjee, J. K. Meena, P. Mali, S. Mukhopadhyay, D. Pandit, H. Pai, S. R. Banerjee, and D. Gupta **Phys. Rev. C 85, 064607 (2012)**.

3. *"Measurement of Giant Dipole Resonance width at low temperature: A new experimental perspective"*, S. Mukhopadhyay, Deepak Pandit , Surajit Pal, Srijit Bhattacharya, A. De, S. Bhattacharya, C. Bhattacharya, **K. Banerjee**, S. Kundu, T. K. Rana, G. Mukherjee, R. Pandey, M. Gohil, H. Pai, J. K. Meena and S. R. Banerjee, **Phys. Lett. B 709, 9 (2012)**.

4. *"Onset of deformation at N = 112 in Bi nuclei"*, H. Pai, G. Mukherjee, R. Raut, S. K. Basu, A. Goswami, S. Chanda, T. Bhattacharjee, S. Bhattacharyya, C. Bhattacharya, S. Bhattacharya, S. R. Banerjee, S. Kundu, **K. Banerjee**, A. Dey, T. K. Rana, J. K. Meena, D. Gupta, S. Mukhopadhyay, Srijit Bhattacharya, Sudeb Bhattacharya, S. Ganguly, R. Kshetri, and M. K. Pradhan, **Phys. Rev. C 85, 064317 (2012)**.

5. *"MONSTER: a time of flight spectrometer for Îš-delayed neutron emission measurements"*, A R Garciaa, T MartÃŋneza, D Cano-Otta, J Castillaa, C Guerreroa,b, J MarÃŋna, G MartÃŋneza, E Mendozaa, M C Ovejeroa, E M Reilloa, C Santosa, F J Teraa, D VillamarÃŋna, R Noltec, J Agramuntd, A Algorad, J L Taind, **K Banerjeee**, C Bhattacharyae, H PentillÃd'f, S Rinta-Antilaf and D Gorelov, **IOP Jour. of Instr. 7C, 05012 (2012)**.

6. *"Cluster emission in ^{13}C + ^{12}C and ^{12}C + ^{12}C reaction at 6MeV/nucleon"*, T. K. Rana, C. Bhattacharya, S. Kundu, **K. Banerjee**, S. Bhattacharya, G. Mukherjee, T. K. Ghosh, J. K. Meena, P. Dhara and M. Biswas, H. Pai, K. Mahata, S. Kumar, K. Ramachandran, P. C. rout and S. K. Pandit, V. Nalal and R.G. Pillay, **Intr. Jour. of Mod Phys E 20, 789 (2011)**.

7. *"Change over from compound nuclear fission to quasi-fission"*, T. K. Ghosh, **K. Banerjee**, C. Bhattacharya, S. Bhattacharya, S. Kundu, P. Mali, J. K. Meena,

G. Mukherjee, S. Mukhopadhyay, and T. K. Rana. **EPJ Web of Conference 2, 10003 (2010)**.

8. *"Extreme nuclear shapes examined via giant dipole resonance lineshapes in hot light-mass systems"*, Deepak Pandit, S.Mukhopadhyay, Srijit Bhattacharya, Surajit Pal, A. De, S. Bhattacharya, C. Bhattacharya, **K. Banerjee**, S. Kundu, T. K. Rana, A. Dey, G. Mukherjee, T. Ghosh, D. Gupta, and S. R. Banerjee, **Phys. Rev. C 81, 061302(R) (2010)**.

9. *"Light charged particle emission from hot $^{32}S^{*}$ formed in $^{20}Ne + {}^{12}C$ reaction"*, Aparajita Dey, S. Bhattacharya, C. Bhattacharya, **K. Banerjee**, T. K. Rana, S. Kundu, S. R. Banerjee, S. Mukhopadhyay, D. Gupta, and R. Saha, **Eur. Phys. J. A 41, 39 (2009)**.

10. *"Sharp change-over from compound nuclear fission to quasifissio"*, T. K. Ghosh, **K. Banerjee**, C. Bhattacharya, S. Bhattacharya, S. Kundu, P. Mali,J. K. Meena, G. Mukherjee, S. Mukhopadhyay, and T. K. Rana, **Phys. Rev. C 79, 054607 (2009)**.

11. *"Giant dipole resonance width in nuclei near Sn at low temperature and high angular momentu"*, Srijit Bhattacharya, S. Mukhopadhyay, Deepak Pandit, Surajit Pal, A. De, S. Bhattacharya, C. Bhattacharya, **K. Banerjee**, S. Kundu, T. K. Rana, A. Dey, G. Mukherjee, T. Ghosh, D. Gupta, and S. R. Banerjee, **Phys. Rev. C 77, 024318 (2008)**.

12. *"Consistency of nuclear thermometric measurements at moderate excitation"*, T. K. Rana, C. Bhattacharya, S. Kundu, **K. Banerjee**, S. Bhattacharya, A. Dey, T. K. Ghosh, G. Mukherjee, J. K. Meena,D. Gupta, S. Mukhopadhyay, D. Pandit, S. R. Banerjee, A. Roy, and P. Dhara, **Phys. Rev. C 78, 027602 (2008)**.

13. *"Fragment emission studies of the ^{16}O + ^{12}C reaction"*, S. Kundu, A. Dey, **K. Banerjee**, T. K. Rana, S. Mukhopadhyay, D. Gupta, R. Saha, S. Bhattacharya, and C. Bhattacharya, **Phys. Rev. C 78, 044601 (2008)**.

14. *"LAMBDA: Large Area Modular BaF_2 Detector Array for the measurement of high energy gamma rays"*, S. Mukhopadhyay, Srijit Bhattacharya, Deepak Pandit, A. Ray, Surajit Pal, **K. Banerjee**, S. Kundu, T. K. Rana, S. Bhattacharya, C. Bhattacharya, A. De, S. R. Banerjee, **Nucl. Instr. and Meth. A, 582, 603 (2007)**.

15. *"Study of dissipative collisions of ^{20}Ne (≈ 7-11 MeV/nucleon)+ ^{27}Al"*, Aparajita Dey, C. Bhattacharya, S. Bhattacharya, T. K. Rana, S. Kundu, **K. Banerjee**, S. Mukhopadhyay, S. R. Banerjee, D. Gupta, and R. Saha, **Phys. Rev. C 75, 064606 (2007)**.

16. *"Characterization of fragment emission in ^{20}Ne(≈ 7-11 MeV/nucleon)+^{12}C reactions"*, Aparajita Dey, C. Bhattacharya, S. Bhattacharya, S. Kundu, **K. Banerjee**, S. Mukhopadhyay, D. Gupta, T. Bhattacharjee, S. R. Banerjee, S. Bhattacharyya, T. K. Rana, S. K. Basu, R. Saha, K. Krishan, A. Mukherjee, D. Bandopadhyay, and C. Beck, **Phys. Rev. C 76, 034608 (2007)**.

17. *"Evidence of large nuclear deformation of $^{32}S^*$ formed in the ^{20}Ne + ^{12}C reaction"*, Aparajita Dey, S. Bhattacharya, C.Bhattacharya, **K. Banerjee**, T. K. Rana, S. Kundu, S. Mukhopadhyay, D. Gupta, and R. Saha, **Phys. Rev. C 74, 044605 (2006)**.

18. *"Survival of orbiting in ^{20}Ne (7- 10 MeV/nucleon) + ^{12}C reactions"*, C. Bhattacharya, A. Dey, S. Kundu, **K. Banerjee**, S. Bhattacharya, S. Mukhopadhyay, D. Gupta, T.Bhattacharjee, S. R. Banerjee, S. Bhattacharya, T. Rana, S. K. Basu,

R. Saha, S. Bhattacharjee, K. Krishan, A. Mukherjee, and D. Bandopadhyay **Phys. Rev. C 72, 021601(R) (2005)**.